

**MODELLING AND SIMULATION OF METAL  
CUTTING BY FINITE ELEMENT METHOD**

A THESIS SUBMITTED IN PARTIAL FULFILLMENT OF THE  
REQUIREMENT FOR THE AWARD OF THE DEGREE OF

**MASTER OF TECHNOLOGY**

(COMPUTATIONAL DESIGN)

TO

**DELHI TECHNOLOGICAL UNIVERSITY**



SUBMITTED BY

**NEERAJ YADAV**

**ROLL NO.:2K15/CDN/08**

UNDER THE GUIDANCE OF

**DR. ATUL KUMAR AGRAWAL**

**PROFESSOR**

DELHI TECHNOLOGICAL UNIVERSITY

**DEPARTMENT OF MECHANICAL, PRODUCTION & INDUSTRIAL  
AND AUTOMOBILE ENGINEERING**

**DELHI TECHNOLOGICAL UNIVERSITY**



**BAWANA ROAD, DELHI-110042**

**DELHI TECHNOLOGICAL UNIVERSITY**

(Formerly Delhi college of Engineering)

Shahbad Daulatpur, Baawana Road,

Delhi-110042

---

## **STUDENT'S DECLARATION**

I, **Neeraj Yadav**, hereby certify that the work which is being presented in this thesis entitled “**Modelling And Simulation Of Metal Cutting By Finite Element Method**” is submitted in the partial fulfilment of the requirement for degree of **Master of Technology (Computational Design)** in Department of Mechanical Engineering at **Delhi Technological University** is an authentic record of my own work carried out under the supervision of **Dr.Atul Kumar Agrawal**. The matter presented in this thesis has not been submitted in any other University/Institute for the award of Master of Technology Degree. Also, it has not been directly copied from any source without giving its proper reference.

### **Signature of Student**

This is to certify that the above statement made by the candidate is correct to the best of my knowledge.

### **Signature of Supervisor**



**DELHI TECHNOLOGICAL UNIVERSITY**

(Formerly Delhi college of Engineering)

Shahbad Daultapur, Baawana Road,

Delhi-110042

---

## **CERTIFICATE**

This is to certify that this thesis report entitled, “**Modelling And Simulation Of Metal Cutting By Finite Element Method**” being submitted by **Neeraj Yadav (Roll No. 2K15/CDN/08)** at Delhi Technological University, Delhi for the award of the Degree of Master of Technology as per academic curriculum. It is a record of bonafide research work carried out by the student under my supervision and guidance, towards partial fulfilment of the requirement for the award of Master of Technology degree in Computational Design. The work is original as it has not been submitted earlier in part or full for any purpose before.

**Dr. Atul Kumar Agrawal**

**Professor**

**Mechanical Engineering Department**

**Delhi Technological University**

**Delhi-110042**

## **ACKNOWLEDGEMENT**

Research is a higher concept. It brings to test our patience, vigour and dedication. Every result arrived is a beginning for a higher achievement. My project is a small drop in an ocean. It needs the help of friends and guidance of experts in the field, to achieve something new.

I found my pen incompetent to express my thanks to my supervisor **Dr. Atul Kumar Agrawal, Professor, DTU** under whose kind and worthy guidance and supervision I had the opportunity to carry out this work. It was only due to him advice, thoughtful comments, constructive criticism, and continuous vigil over the progress of my work with personal interest that it has taken this shape. He has been a great source of encouragement.

I would like to extend my gratitude to **Prof. R.S. Mishra, Head**, Department of Mechanical Engineering, Delhi Technological University, for providing this opportunity to carry out the present thesis work.

I would especially like to acknowledge my gratitude to all my dear friends for their consistent support, valuable suggestions from time to time to make this project worthy.

With a silent prayer to the almighty Finally, and most importantly, I would like to thank my family for their truthful care and support. My warmest thanks to my parents for their patience and everything they have done for me to become what I am today.

**NEERAJ YADAV**

**M.Tech (COMPUTATIONAL DESIGN)**

**2K15/CDN/08**

# TABLE OF CONTENTS

<b>STUDENT’S DECLARATION</b> .....	<b>ii</b>
<b>CERTIFICATE</b> .....	<b>iii</b>
<b>ACKNOWLEDGEMENT</b> .....	<b>iv</b>
<b>ABSTRACT</b> .....	<b>xiii</b>
<b>1 INTRODUCTION</b> .....	<b>1</b>
1.1 Historical Developments .....	5
1.2 Advantages of finite element method .....	11
1.3 Aim .....	11
1.4 Methodology .....	12
1.5 Thesis outline:.....	12
<b>2 LITERATURE REVIEW: THEORY AND BASICS OF ORTHOGONAL METAL CUTTING</b> .....	<b>13</b>
2.1 Introduction.....	13
2.2 Orthogonal Metal Cutting.....	14
2.3 Chip Morphology.....	16
2.3.1 Discontinuous chip: .....	16
2.3.2 Continuous chip: .....	16
2.3.3 Continuous chip with built-up edge: .....	17
2.3.4 Cyclic or serrated chips: .....	17
2.4 Deformation zones.....	18
2.5 Mechanics of Metal Cutting.....	19
2.6 Friction in Metal Cutting .....	25
2.7 Shear Stress in Metal Cutting .....	26
2.8 Chip Formation Process .....	27
2.9 Temperature in Metal Cutting.....	28
<b>3 LITERATURE REVIEW: THEORY AND BASICS OF LINEAR ELASTIC FRACTURE MECHANICS</b> .....	<b>30</b>
3.1 Stress Distribution Around a Crack.....	30
3.2 Plane stress versus plane strain.....	32
3.3 Loading Modes .....	33

3.4	Stress Intensity Factors .....	34
3.5	Toughness of material .....	37
3.6	The Griffith Energy Balance .....	38
3.7	The Energy Release Rate.....	40
3.8	The J-Integral.....	42
3.9	The Finite Element Method .....	47
3.9.1	System of Equations .....	47
3.9.2	Constitutive Relations .....	48
3.9.3	Element Types .....	49
3.10	The Classical Approach to the Stress Intensity Factor Calculation .....	50
3.11	Finite element analysis techniques .....	53
3.11.1	Available tools and softwares.....	54
3.12	Conclusion .....	55
<b>4</b>	<b>SIF AND J-INTEGRAL DETERMINATION USING ABAQUS®.....</b>	<b>56</b>
4.1	Using Abaqus/CAE (v6.14).....	56
4.2	Finite Elements in Fracture Mechanics .....	60
4.3	SIF Extraction for a 2D centre cracked plate of Finite Dimensions .....	61
4.3.1	Procedure used in Abaqus .....	61
4.3.2	Analytical solution.....	69
4.3.3	Comparison results of Abaqus with Analytical Solution .....	69
4.4	SIF Extraction for Crack in a Three Point Bend Specimen (Moment applied).....	70
4.4.1	Problem Description and Abaqus Procedure.....	70
4.4.2	Analytical solution.....	73
4.4.3	Comparison results of Abaqus with Analytical Solution .....	73
4.5	SIF Extraction for a 3D centre through cracked plate of Finite Dimensions.....	74
4.5.1	Procedure used in Abaqus .....	75
4.5.2	Analytical Solutions .....	82
<b>5</b>	<b>HERTZ CONTACT ANALYSIS USING FINITE ELEMENT METHOD .....</b>	<b>83</b>
5.1	Introduction.....	83
5.2	Hertz Contact Theory .....	84
5.2.1	Assumptions and Idealizations:.....	85
5.2.2	Sphere – Sphere Contact.....	86
5.2.3	Cylinder–Cylinder Contact.....	90
5.2.4	Applications.....	93

5.3	Hertz contact modelling in ABAQUS® (2D Cylinder Roller Contact).....	94
5.3.1	Problem Description .....	94
5.3.2	FEM Solution .....	95
5.3.3	Analytical solution.....	97
5.3.4	Conclusion.....	98
<b>6</b>	<b>FINITE ELEMENT FORMULATION IN METAL CUTTING .....</b>	<b>100</b>
6.1	Introduction.....	100
6.2	Model Formulation .....	100
6.2.1	Lagrangian .....	101
6.2.2	Eulerian.....	101
6.2.3	Arbitrary Lagrangian-Eulerian (ALE) .....	102
6.2.3.1	Boundaries in ALE methods.....	103
6.2.3.2	Mesh-update procedures.....	103
6.3	Meshing .....	104
6.4	Geometry Modelling.....	105
6.5	Governing Equations .....	106
6.5.1	Conservation laws: .....	106
6.5.2	Workpiece material constitutive equations: .....	107
6.6	Damage and Failure Model .....	108
6.7	Chip Separation Criteria .....	110
6.8	Friction Models.....	112
6.8.1	Constant Coulomb .....	112
6.8.2	Constant Shear .....	113
6.8.3	Constant Shear in Sticking Zone and Coulomb in Sliding Zone.....	113
6.9	Chip-Tool Interface Model and Heat Generation .....	113
6.10	ABAQUS Platform.....	114
<b>7</b>	<b>PRESENT MODEL AND SIMULATION OF METAL CUTTING.....</b>	<b>117</b>
7.1	Introduction.....	117
7.2	Tool Modelling .....	118
7.3	Work piece Modelling .....	119
7.4	System Modelling.....	122
7.4.1	Interfacial contact and friction .....	122
7.4.2	Boundary Conditions.....	123
7.4.2.1	Displacement Boundary Conditions .....	123
7.4.2.2	Thermal Boundary Condition.....	123
<b>8</b>	<b>RESULTS AND DISCUSSION.....</b>	<b>125</b>

8.1	Finite element modelling based on adiabatic analysis .....	126
8.1.1	Chip morphology and its mechanism .....	126
8.1.2	Variation of feed and cutting speed .....	128
8.2	Finite element modeling based on fully coupled temperature- displacement analysis .....	129
8.2.1	Chip morphology .....	129
8.2.2	Cutting forces .....	133
8.2.3	Variation of cutting speed & Feed .....	134
8.2.4	Effects of Coefficient of friction.....	133
8.3	Comparison of Cutting Force with Experimental Data:.....	134
8.4	Verification of simulated results.....	134
8.5	Discussion.....	135
<b>9</b>	<b>CONCLUSIONS AND FUTURE WORK .....</b>	<b>138</b>
9.1	Conclusions.....	138
9.2	Future Works .....	139
	<b>REFERENCES .....</b>	<b>141</b>
	<b>APPENDIX.....</b>	<b>145</b>



## LIST OF FIGURES

Figure 2.1: Geometric description of a basic machining process in 2D. Figure by Emese [18].....	14
Figure 2.2: Types of cutting: (a) Orthogonal cutting, (b) Oblique cutting .....	15
Figure 2.3: Different types of chips in metal cutting .....	17
Figure 2.4: Deformation zones in metal cutting .....	18
Figure 2.5: Variables in orthogonal cutting .....	19
Figure 2.6: 2D orthogonal cutting forces diagram.....	20
Figure 2.7: Merchant's circle diagram for 2D orthogonal cutting.....	21
Figure 2.8: Shear plane angle in orthogonal cutting .....	23
Figure 2.9: Velocity Vector Diagram .....	24
Figure 2.10: Distribution of shear and normal stress on the rake face.....	26
Figure 2.11: Pre-flow region.....	27
Figure 2.12: Locations of heat sources in metal cutting .....	28
Figure 3.1: Real and ideal crack tension behaviour [28] .....	30
Figure 3.2: Stresses near the crack tip and polar coordinates [1] .....	31
Figure 3.3: Stress tensor at a point in space.....	32
Figure 3.4: Loading modes I, II and III [1].....	34
Figure 3.5: A through-thickness crack in an infinitely wide plate subjected to a remote tensile stress [28] .....	39
Figure 3.6: a) 2D contour integral, b) 2D closed contour integral [35].....	42
Figure 3.7: a) Local coordinates system, b) 3D J-Integral [8].....	45
Figure 3.8: FEM domain and boundary conditions [32].....	47
Figure 3.9: Three dimensional elements, (a) 8 nodes, (b) 20 nodes, (c) 10 nodes, from [35] .....	49
Figure 3.10: Degeneration of a quadrilateral element into a triangle at the crack tip [28] .....	50
Figure 3.11: Degeneration of a brick element into a wedge [28].....	50
Figure 3.12: Crack-tip elements for elastic and elastic-plastic analyses.....	51
Figure 3.13: Spider-web mesh from [35].....	52
Figure 3.14: Example of discretization.....	53

Figure 3.15: Numerical simulation process. ....	53
Figure 4.1: Graphical user interface of Abaqus/CAE v6.14 upon start up. ....	57
Figure 4.2: 2D Centre Crack Geometry .....	61
Figure 4.3: 2D centre crack plate mesh .....	66
Figure 4.4: 2D centre crack plate von-mises stress contour .....	67
Figure 4.5: Three Point Bend Specimen (Moment applied) .....	70
Figure 4.6: Three Point Bend Specimen mesh.....	70
Figure 4.7: Three Point Bend Specimen von-mises stress contour .....	72
Figure 4.8: 3D centre through cracked plate(half part).....	74
Figure 4.9: crack extension direction shown by q-vector .....	77
Figure 4.10: 3D centre through crack mesh.....	79
Figure 4.11: J-Contour layers along the thickness of plate.....	80
Figure 4.12: 3D centre crack von-mises stress contour .....	80
Figure 4.13: SIF variation over the plate .....	81
Figure 5.1: Two Sphere in Contact .....	86
Figure 5.2: Magnitude of the stress components below the surface as a function of maximum pressure of contacting spheres. ....	89
Figure 5.3: Two Cylinders in Contact.....	90
Figure 5.4: Magnitude of stress components below the surface as a function of maximum pressure for contacting cylinders. ....	93
Figure 5.5: 2d cylinder roller contact master-slave surface.....	95
Figure 5.6: 2d cylinder roller contact mesh .....	95
Figure 5.7: 2d cylinder roller contact deformed shape at magnification factor=1.....	96
Figure 5.8: 2d cylinder roller contact von-mises stress contour at magnification factor=1 .....	96
Figure 5.9: Comparison of Analytical and FEM ABAQUS Solution .....	97
Figure 6.1: An explanatory demonstration of the Eulerian, Lagrangian and ALE formulations. Figure from Proudian [44] .....	102
Figure 6.2: Eulerian and Lagrangian boundary conditions in ALE simulation(Source: Ozel, et al. 2007)[45] .....	103
Figure 6.3: Smoothing: (a) Initial local mesh, (b) Reallocating of the nodes.....	105
Figure 6.4: Refinement: (a) Initial local mesh, (b) Reducing element size .....	105
Figure 6.5: Illustration of the 3D-2D projection.....	106

Figure 6.6: Stress-strain curve with damage degradation .....	108
Figure 6.7: Geometrical Separation (Source: Mamalis, et al. 2001).....	111
Figure 6.8: Orthogonal metal cutting simulation by using Abaqus .....	116
Figure 7.1: Cutting Tool Mesh.....	118
Figure 7.2: Geometric Details and Mesh of Workpiece .....	120
Figure 7.3: Adiabatic Stress-Strain relationship for AISI 4340.....	121
Figure 7.4: Tool-Chip Surface-Node Interaction.....	122
Figure 8.1: Von-mises stress and strain contours for segmented chip.....	126
Figure 8.2: Temperature Distribution .....	126
Figure 8.3: Variation of Cutting Force and Thrust Force .....	127
Figure 8.4: Effect of Feed on $F_c$ and $F_t$ .....	128
Figure 8.5: Effect of cutting velocity on $F_c$ and $F_t$ .....	129
Figure 8.6: Deformed continuous chip mesh.....	130
Figure 8.7: Deformed Segmented chip mesh.....	130
Figure 8.8: Temperature Distribution .....	131
Figure 8.9: Von-mises stress and strain contours for continuous chip .....	131
Figure 8.10: Evolution of $F_c$ and $F_t$ for continuous and Segmented chip .....	133
Figure 8.11: Distribution of $\sigma$ and $\tau$ on rake surface .....	134
Figure 8.12: Variation of $F_c$ and $F_t$ for continuous chip at different cutting velocity	134
Figure 8.13: Variation of $F_c$ and $F_t$ for segmented chip at different cutting velocity	135
Figure 8.14: Variation of (a) chip reduction ratio (b) deformed chip thickness and (c) tool-chip contact length with cutting velocity for continuous and segmented chip formation.....	136
Figure 8.15: Variation of cutting force over feed and speed .....	136
Figure 8.16: Effect of coefficient of friction on Average cutting force.....	133
Figure 8.17: Effect of coefficient of friction on shear zone temperature.....	133
Figure 8.18: Comparison of predicted forces during simulation of continuous and segmented chip formation with experimental forces .....	135

## LIST OF TABLES

Table 3.1: Critical stress intensity factors for common materials .....	35
Table 4.1: Outline of Abaqus/CAE v6.14 modules. ....	57
Table 4.2: Comparison of results of 2D Centre Crack.....	69
Table 4.3: Comparison of results for Three point Bend Specimen.....	73
Table 4.4: SIF results for various layers .....	81
Table 4.5: SIF determined from analytical solutions.....	82
Table 5.1: Comparison result of 2D cylinder roller contact of ABAQUS with Analytical .....	98
Table 7.1: Geometric variables of the cutting tool .....	118
Table 7.2: cutting tool properties (Ozel & Zeren, 2006) .....	118
Table 7.3: Details of the geometric model and cutting parameters .....	119
Table 7.4: Workpiece properties (Ozel & Zeren, 2006) .....	120
Table 7.5: Johnson-Cook parameters for AISI 4340 (Johnson & Cook, 1983; Johnson & Cook, 1985) .....	121
Table 8.1: Cutting force comparison with experimental data at different velocity ...	134

## **ABSTRACT**

Metal cutting, or simply machining, is one of the oldest processes for shaping components in the manufacturing industry. It is widely quoted that 15% of the value of all mechanical components manufactured worldwide is derived from machining operations. There are lots of studies to investigate this complex process in both academic and industrial world. Predictions of important process variables such as temperature, cutting forces and stress distributions play significant role on designing tool geometries and optimising cutting conditions. Researchers find these variables by using experimental techniques which makes the investigation very time consuming and expensive. At this point, finite element modelling and simulation becomes main tool. These important cutting variables can be predicted without doing any experiment with finite element method

The developed model was implemented in the FEM package ABAQUS as a user material model and used in the investigation of orthogonal metal cutting. The method chosen for the chip formation has a large impact on the result of the simulations.

This main objective is to deal with the plane strain 2D Finite Element (FE) modelling of segmented, as well as continuous chip formation while machining AISI 4340 with a negative rake carbide tool and to simulate both the continuous and segmented chips from the same FE model based on FE code ABAQUS/Explicit. Both the adiabatic and coupled temperature displacement analysis has been performed to simulate the right kind of chip formation. It is observed that adiabatic hypothesis plays a critical role in the simulation of segmented chip formation based on adiabatic shearing. The numerical results dealing with distribution of stress, strain and temperature for segmented and continuous chip formations were compared and found to vary considerably from each other. The simulation results were also compared with published experimental results; thus validating the developed model.

# **CHAPTER 1**

## **INTRODUCTION**

Machining is a term that covers a large collection of manufacturing processes designed to remove material from a workpiece. This is one of the most important mechanical processes in industry because almost all the products get their final shape and size by material removal either directly or indirectly. Although metal cutting process is commonplace, the underlying physical phenomena are highly complex. Therefore, this area has always been of great interest to the researchers. During the cutting process, the unwanted material is removed from the workpiece with the aid of a machine tool and a cutting tool by straining a local region of the workpiece by the relative motion of the tool and the workpiece. As the tool advances, the material ahead of it is sheared continuously along a narrow zone called the shear plane; thus, removing the excess material in the form of chip that flows along the rake surface of the tool. Metal cutting or machining is considered as one of the most important and versatile processes for imparting final shape to the preformed blocks and various manufactured products obtained from either casting or forging. Major portion of the components manufactured worldwide necessarily require machining to convert them into finished product. Basic chip formation processes include turning, shaping, milling, drilling, etc., the phenomenon of chip formation in all the cases being similar at the point where the cutting edge meets the work material. During cutting, the chip is formed by deforming the work material on the surface of the job using a cutting tool. The technique by which the metal is cut or removed is complex not simply because it involves high straining and heating but it is found that conditions of operation are most varied in the machining process as compared to other manufacturing processes. Although numerous researches are being carried out in the area of metal cutting both for its obvious technical and economical importance, machining still is sometimes referred to as one of the least understood manufacturing processes because of the complexities associated with the process. Efforts are being made continuously to understand the complex mechanism of cutting in a simple and effective way. Improvements in manufacturing technologies

require better modelling and simulation of metal cutting processes. Theoretical and experimental investigations of metal cutting have been extensively carried out using various techniques. On the other hand, complicated mechanisms usually associated in metal cutting, such as interfacial friction, heat generated due to friction, large strains in the cutting region and high strain rates, have somewhat limited the theoretical modelling of chip formation. Numerous works are being constantly published by the researchers to improve the technique, out of which some are based purely on experimental studies while others include various analytical and numerical models. Since experimental studies prove to be very time consuming and costly, considerable amount of research is being devoted to develop analytical and numerical models of chip formation process, thus replacing the costly experiments (Astakhov, 2006). Pioneering works in analytical modelling has been carried by Merchant (1945), Piispanen (1948), Drucker (1949), Hahn (1951), Chao and Trigger (1951), Leone (1954), Loewan and Shaw (1954), Rapier (1954) and Weiner (1955) while in numerical modelling include works by Klamecki (1973) and Tay, Stevenson and Davis (1974), Stevenson, Wright and Chow,(1983), Muraka, Barrow and Hinduja (1979).

Chip formation and its morphology are the key areas in the study of machining process that provide significant information on the cutting process itself. The chip morphology depends upon the workpiece material properties and the cutting conditions. The main chip morphologies observed in cutting process are the continuous and the cyclic or serrated chips. Many parameters, namely, cutting force, temperature, tool wear, machining power, friction between tool-chip interface and surface finish are affected by the chip formation process and chip morphology. Thus, for determining the optimum cutting conditions, it is very essential to simulate the real machining operation by using various analytical and numerical models. Availability of an accurate model aids in the selection of optimal process parameters so that the metal removal process can be carried out more efficiently and economically. One of the state-of-art efforts in manufacturing engineering is the finite element simulation of the metal cutting process. These simulations would greatly enhance our understanding of the metal cutting process and in reducing the number of trial and error experiments, which is used traditionally for tool

design, process selection, machinability evaluation, chip formation and chip breakage investigations. According to a comprehensive survey conducted by the CIRP Working Group on Modeling of Machining Operations during 1996-1997 [1], among the 55 major research groups active in modeling, 43% were active in empirical modeling, 32% in analytical modeling, and 18% in numerical modeling in which finite element modeling techniques are used as the dominant tool. More attention to the finite element method has been paid in the past decade in respect to its capability of numerical modeling of different types of metal cutting problems. So, many researches are focusing on computer modeling and simulation of metal cutting process to solve many complicated problems arising in the development of new technologies.

Thus, FEM-based analysis provides detailed qualitative and quantitative insight in to the chip formation process that is very much required for profound understanding of the influence of machining parameters. While experimental tests and analytical models serve as the foundation of metal cutting, FEM leads to the advancement and further refinement of knowledge in the area of metal cutting.

Finite element method is basically defined as dividing a continuum system to small elements, describes element properties as matrices and assembles them to reach a system of equations whose solutions give the behaviour of the total system.

Basic ideas of the finite element method are studied at the beginning of 1940s. Courant (1943) developed finite element method and he used piecewise polynomial interpolation over triangular subregions to model torsion problems. Clough (1960) used the term “finite element” firstly. Zienkiewicz and Cheung (1967) wrote the first book on finite element theory. Also other theory books are written by Cook, et al. (1989), Mohr (1992) and Chandrupatla and Belegundu (2002). In the present decade FEM is gaining much popularity in the study of machining processes. This not only gives the information of some difficult to measure variables like plastic strain, stresses and machining temperatures, but also overcomes most of the restrictive assumptions associated with analytical models.

With the development of faster processors and larger memory, model limitations and computational difficulty have been overcome to a large extent. In



addition, more commercial FE codes are being developed for cutting simulations, including ABAQUS , AdvantEdge , DEFORM 2D , LS DYNA , FORGE 2D , MARC , FLUENT and ALGOR . Significant progress has been made in this field such as:

- (1) Lagrangian approach is used to simulate the cutting process including incipient chip formation.
- (2) Segmented chip formation is modeled to simulate high-speed machining.
- (3) 3D simulation is performed to analyze oblique cutting.
- (4) A diversity of cutting tools and workmaterials is used in the simulation of cutting process.

According to the review made by [Ng and Aspinwall \(2002\)](#), majority of the works concerned with the numeric modeling deals with the 2D FEM of continuous chip formation. Although study of segmental or serrated chip is quite important in the cutting process when considering wide range of work-piece materials including hardened steels and some aerospace materials, not much work is found in the literature till the year 1999. Recently, there are many significant papers that explain the segmented chip formation by considering the negative rake angles ([Ohbuchi and Obikawa, 2005](#)). Different material models such as the Johnson Cook material model, Rhim and Oh model ([Rhim and Oh, 2006](#)), Obikawa and Usui model (Obikawa and Usui, 1996) are available in the literature. In simulations of machine cutting, the simulation model must adequately handle: huge elasto-plastic deformations, thermal processes and complex interactions, all of which acts very rapidly. Due to this, the simulations are not trivial either from a numerical or from a physical point of view. There are quite a large number of parameters that effects the simulation result, and the parameters themself depend on each other in complex relations.

One of the main problems in Finite Element (FE) simulations of cutting is to get the **material separation** around the tool tip to be physically correct. Several techniques for performing FE simulations of chip-workpiece separation has been proposed during the last 20 years. One of the earlier models for

chip-workpiece separation is path dependent parting and newer ones include frequent adaptive remeshing and more radical ones such as leaving the FE domain and using meshfree methods like Smooth Particle Hydrodynamics (SPH).

The importance of predicting the right kind of chip accurately under various cutting conditions motivates the authors to develop finite element models that should have the capability to satisfactorily analyze both the continuous and the segmented chip formation. Several efforts are being constantly made by the researchers worldwide to come up with significant results in this area. The main objective of this work is to simulate the chip formation process by incorporating ALE along with appropriate material and damage model by following both the adiabatic and coupled temperature displacement analysis.

## **1.1 Historical Developments**

Metal cutting studies are as old as over 100 years. Early research in metal cutting started with Cocquilhat (1851), who was focused on the work required to remove a given volume of material in drilling. Tresca (1873) firstly attempted to explain how chips are formed. Ernest and Merchant (1941) first developed the simplest and most widely used model for cutting. Lee and Shaffer (1951), Kobayashi and Thomsen (1962) contributed to study of Ernest and Merchant. Oxley and Welsh (1963) introduced the first parallel-sided shear zone model of chip formation for a predictive machining theory. Most widely used text books are written by Armerago (1969), Boothroyd (1981), Shaw (1984) and Trent (2000). More general introductory knowledge can be found at text books written by Kalpakjian, et al. (2006), and DeGarmo, et al. (1997).

With the advent of powerful computers and efficient commercial software packages, Finite Element Method (FEM) has become one of the most powerful tools for the simulation and analysis of cutting process. This not only allows studying the cutting process in greater detail than possible in experiments, but also takes into account the material properties and non-linearity better than analytical models. The earliest finite element chip formation studies simulated the loading of tool against a pre-formed chip avoiding the problems of modelling large flows [2]. Small strain

elastic-plastic analysis demonstrated the development of plastic yielding along the primary shear plane as the tool was displaced against the chip. This work had a number of limitations, making it only of historical interest. The limitations of this initial work were removed by Shirakashi and Usui [3], who developed an iterative way of changing the shape of the pre-formed chip until the generated plastic flow was consistent with the assumed shape. They also included realistic chip/tool friction conditions and material flow stress variations with strain, strain rate and temperature measured from high strain rate Hopkinson bar tests. The procedure of loading a tool against an already formed chip greatly reduced computing capacity requirements. The justification of the method was that it gave good agreement with experiments but it did not follow the actual path by which a chip should be formed. Rigid-plastic modelling however, does not require the actual loading path to be followed. Iwata *et al.* [4] developed steady state rigid-plastic modelling (within a eulerian framework) adjusting an initially assumed flow field to bring it into agreement with the computed field. They included friction, work hardening, and a chip fracture criterion. Experiments at low cutting speeds supported their predictions. The mid-1980s saw the first non-steady chip formation analyses, following the development of a chip from first contact of a cutting edge with the workpiece as in machining. Updated Lagrangian elastic-plastic analysis was used, and different chip/ work separation criteria at the cutting edge were developed. Strenkowski and Carol [5] used a strain-based separation criterion. At that time, neither a realistic friction model nor coupling of elastic-plastic to thermal analysis was included.

The 1990s have seen the development of non-steady state analysis, from transient to discontinuous chip formation, the first three-dimensional analyses, and the introduction of adaptive meshing techniques particularly to cope with the flow around the cutting edge of a tool. A simple form of remeshing at the cutting edge, instead of the geometrical crack, was introduced to accommodate the separation of chip from the work. Both rigid- plastic and elastic-plastic adaptive remeshing softwares have been developed and are being applied for chip formation simulations [6, 7]. Marusich and Ortiz [6] developed a two-dimensional finite element code for the simulation of orthogonal cutting that includes

sophisticated adaptive remeshing, thermal effects, a criterion for brittle fracture and tool stiffness. They seem to be more effective than Arbitrary Lagrangian-Eulerian (ALE) methods in which the mesh is neither fixed in space nor in the workpiece. Thus, the 1970s to the 1990s has seen the development and testing of finite element techniques for chip formation processes and during this period, many researchers have concentrated more on the development of the new methods in the finite element simulations of metal cutting [3].

Pioneering work in the analysis of metal cutting by using FEM has been carried out by Klamecki (1973) and Tay et al. (1974). Generally, application of finite element modeling to cutting process involves Eulerian, Lagrangian or Arbitrary Lagrangian Eulerian (ALE) formulations. Tay et al. (1974) used the Eulerian formulation technique that is often being used till date. In Eulerian approach, the reference frame is fixed in space that allows for the material to flow through the grid (Raczy et al., 2004). As the mesh is fixed in space, the numerical difficulties associated with the distortion of elements are eliminated. In one of the recent works, an Eulerian finite element model has been applied to the simulation of machining which showed good overall correlation with the experimental results (Akarca et al., 2008). This approach permits simulation of machining process without the use of any mesh separation criterion. The main drawback of Eulerian formulation is that it is unable to model the unconstrained flow of material or free boundaries and may only be used when boundaries of the deformed material are known a priori. Hence, in this case, dimension of the chip must be specified in advance to produce a predictive model for chip formation (Mackerle, 1962). While in Lagrangian approach, no a priori assumption is needed about the shape of the chip. In Lagrangian approach, the reference frame is set by fixing the grid to the material of interest such that as the material deforms the grid also deforms. Lagrangian formulation is easy to implement and is computationally efficient. Difficulties arise when elements get highly distorted during the deformation of the material in front of the tool tip. Both the approaches, Eulerian and Lagrangian, have their own advantages and disadvantages. The strong point of one is the weakness of the other. Keeping this in view, a more general approach, Arbitrary Lagrangian Eulerian (ALE) approach was introduced by the end of the last decade which takes the best part of both the

formulations and combines them in one (Obikawa et al., 1997). ALE reduces to a Lagrangian form on free boundaries while maintains an Eulerian form at locations where significant deformations occur, as found during the deformation of material in front of the tool tip; thus avoiding the need of remeshing (Rakotomalala et al., 1993). Olovsson et al. (1999) stated that implementation of ALE into the special purpose computer code Exhale2D allowed flow boundary conditions whereby a small part of the workpiece in the vicinity of the tool tip needs to be modeled. Movaheddy et al. (Movahhedy et al., 2008) presented the ALE model for continuous chip to study the effect of tool edge preparation. Attanasio et al. (2008) predicted flank wear and crater wear evolution by utilizing a diffusion wear model implemented in an ALE numerical simulation of turning operation on AISI 1045 by uncoated WC tool.

Therefore, many **chip separation criteria** have been used in the literature to simulate the cutting action at the cutting zone (Strenkowski & Moon, 1990). These criteria are grouped as geometrical and physical types. A geometrical criterion is based on a specified small distance from the tool tip, beyond which the separation of nodes is allowed along the predefined parting line. Komvopoulos and Erpenbeck (1991) used a distance tolerance of half of the length of the side length of the element in front of the tool tip. According to the physical criteria, the nodes get separated when the value of a predefined physical parameter, such as stress, strain or strain energy density, at nodes reaches a critical value that has been selected depending upon the work material properties and the cutting condition (Iwata et al., 1984). Strenkowski and Carrol (1985) introduced the chip separation criterion based on the effective plastic strain at the node nearest to the cutting edge, the typical limit ranging from 0.25 to 1.00. Many researchers have used this criterion to model the cutting process by considering various limit values. Even if the criterion is chosen properly, there is no physical indication as to what limit value should be used; thus making the chip separation model more of arbitrary nature. Consequently, this limits the application of Lagrangian formulation in modeling the metal cutting process.

Ng and Aspinwall (1999) pointed out in a review that majority of the works concerned with the numerical modeling deals with the 2D FEM of continuous chip

formation. The continuous chip is an ideal type of chip for analysis because the shear deformation imposed by the cutting tool on the workpiece is uniformly distributed throughout the chip which makes it stable. Shi and Liu (2004) performed a fully coupled thermal stress analysis using ABAQUS/Explicit v6.2 to compare the results obtained from four different material models for simulating the formation of continuous chips. Li et al. (2002) employed Johnson–Cook’s model as constitutive equation of the workpiece material for qualitative understanding of crater-wear from the calculated temperature distribution by using Abaqus and other commercially available FE codes. Ozel (2006) has simulated continuous chip formation process by using DEFORM-2D software to study the effect of tool-chip interfacial friction models on the FE simulations.

Baker et al. (2002) studied the chip segmentation in detail based on adiabatic shearing while machining Ti6Al4V by using ABAQUS/Standard by considering simple isotropic plastic flow law as the material model. Similarly, Mabrouki et al. (2006) focused on adiabatic shearing using Johnson cook material model for AISI 4340 steel and compared the results obtained from ABAQUS/Explicit and Thirdwave Systems’ AdvantEdge with those obtained experimentally. Calamaz et al. (2008) proposed a new material model that takes into account not only the strain hardening and the thermal softening phenomenon, as in case of Johnson- Cook model, but also strain softening phenomenon by using the finite element solver FORGE 2005. Vyas and Shaw (1999) have argued that the root cause of saw tooth chip formation is cyclic cracking. Baker et al. (2002) focused on the effects that a growing crack has on the plastic deformation of the material. In one of the recent papers (Lorentzon & Jarvstrat, 2009), the effect of different fracture criteria on the segmented chip formation has been investigated for the alloy 718. A conclusion from that study is that both thermal softening and material damage cause the transition from continuous chip to segmented chip formation.

Pioneering works to determine cutting temperature using analytical approach began in 1951 by Hahn [8] followed by Chao and Trigger [9], Leone [10], Loewan and Shaw [11], Weiner [12] and Rapier [13]. In analytical modeling, especially in earlier works, uniform plane heat source and velocity discontinuity were often assumed by considering that the chip is formed instantaneously at the shear plane. The

secondary deformation zone was usually neglected and the tool chip frictional force was taken as uniform. Such simplified assumptions modify the original problem to some extent.

Bai and Dodd (1992) have concluded that the adiabatic shear bands are commonly the precursors to fracture. Calamaz, Coupard and [Girod \(2008\)](#) proposed a new material model that takes into account not only the strain rate hardening and the thermal softening phenomenon, as in case of Johnson-Cook model, but also strain softening phenomenon by using the finite element solver FORGE 2005. Nakayama al. (1988), Aurich and Bil (2006) presented a 3D FE model for the simulation of segmented chip formation and investigated the relative effect of the two mentioned alternative mechanisms on the predicted chip formation. In addition to the mechanisms leading to segmented chip formation, few researchers have focused on the factors influencing the shear frequency. It has been found that the cutting speed and the feed are the main parameters controlling the frequency of segmentation ([Bayoumi and Xie, 1995](#); [Hou and Komanduri,1995](#)).

## **1.2 Advantages of finite element method**

**Advantage** of finite element method is the entire process can be simulated using a computer. Compared to empirical and analytical methods, finite element methods used in the analysis of chip formation have advantages in several respects, namely,

- (1) Material properties can be handled as a function of strain, strain rate, and temperature.
- (2) Interaction between the chip and the tool can be modeled as sticking and sliding.
- (3) Non-linear geometric boundaries, such as the free surface of the chip can be represented and used.
- (4) In addition to the global variables such as, the cutting force, thrust force and chip geometry, local variables, such as stresses, temperature distributions, etc., can also be obtained.

## **1.3 Aim**

The aim of this thesis is to be a pre-study for coming simulations of orthogonal cutting in ABAQUS. This pre-study covers a wide range of questions related to cutting simulations, of which the main questions for the study are:

Which are the important parameters for performing simulations of orthogonal cutting?

What are the limitations when performing cutting simulations in ABAQUS/Explicit?

Which are the possible ways to perform chip-workpiece separation in cutting simulations?

Which of these possible ways are suitable for simulations in ABAQUS/Explicit?



## **1.4 Methodology**

The questions are explored first in a literature study, presented in the theory Chapter and thereafter the investigation is continued by some simulations in the commercial simulation software ABAQUS. Finite Element (FE) model with Arbitrary Lagrangian-Eulerian (ALE) formulation is implemented and examined.

## **1.5 Thesis outline:**

A brief description of each chapter in this study is given in the following: Chapter 1 gives a introduction, and historical developments in metal cutting simulation. In chapter two, theories of metal cutting is discussed which can be used in analytical solutions. In chapter three, because metal cutting has fracture and crack propagation ahead of tool tip hence Theory of Linear Elastic Fracture mechanics is given. In chapter four, some classic fracture problems are discussed and stress intensity factor, J-Integral is determined using ABAQUS and results are analytically validated. In chapter five, since in metal cutting there is tool chip contact and hence master-slave surface choosen in ABAQUS, hence classic hertz contact simulation is done on ABAQUS and results are analytically validated. In chapter six, there is theory about how to perform finite element simulation of metal cutting in ABAQUS, which is helpful when a real simulation is performed. In chapter seven, there is a model of metal cutting presented taken from experimental results and the model is simulated in ABAQUS and results are compared with experimental data. In chapter eight, results and discussion about presented model is given. In chapter nine, conclusion and future work is given.

## **CHAPTER 2**

### **LITERATURE REVIEW: THEORY AND BASICS OF ORTHOGONAL METAL CUTTING**

#### **2.1 Introduction**

The process of machining consists of removing material from a workpiece, by means of shear deformation, with a sharp cutting tool. A motion of the workpiece relative to the tool is needed in order to achieve the removal. This motion is in most machining processes defined as a primary motion, called the cutting speed, which for the specific case of turning is the velocity with which the workpiece rotates. A secondary motion called feed rate, which for turning is the axial distance the tool advances in one revolution of the workpiece, is usually also defined.

Metal cutting process involves various independent and dependent variables. Independent variables are the input variables over which the machinist has direct control [14]. These include type of workpiece material and tool material, shape and size of workpiece material, cutting tool geometry, type of machining process, cutting parameters (speed, feed and depth of cut) and cutting fluids. The type of input parameters selected during machining process decides much about the dependent variables. The important dependent or output variables are cutting force and power, surface finish, tool wear and tool failure, size and properties of the finished product. A small change in input variables, say, cutting parameters, tool geometry and workpiece or tool material may alter the forces to great extent. Surface finish is again a function of tool geometry, tool material, workpiece material and cutting parameters. Tool wear is also a crucial aspect of machining pertaining to the economics of machining since longer tool life leads to higher productivity. Moreover, as the tool wear takes place, it changes in both geometry and size. Such a change can result in increased cutting forces which in turn increase deflection in the workpiece and may create a chatter condition. Again due to increased power consumption, there can be increased heat generation, thus accelerating the wear rate.

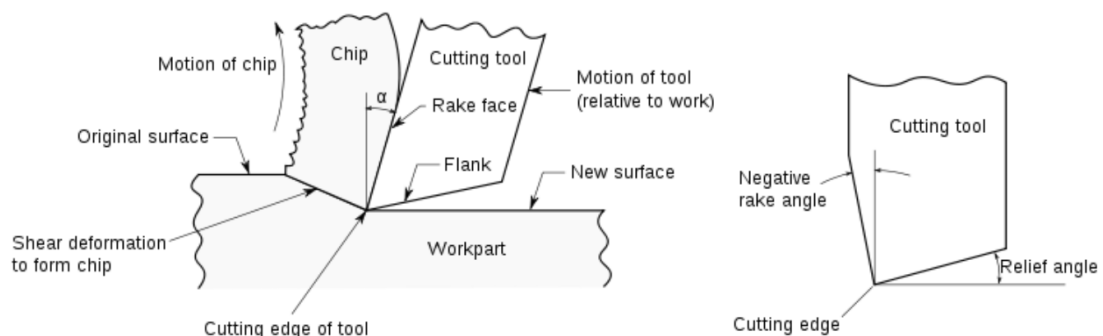
The enormous variety in input variables leads to infinite combinations and understanding the interrelationship between these input variables and output variables again becomes an arduous task.

The metal cutting processes used can be divided into two types: orthogonal cutting, where the tool's cutting edge is perpendicular to the direction of motion, and oblique cutting where the cutting edge forms an inclination angle relative to the cutting direction [15]. Orthogonal cutting is rarely not existing in industry but it is common in research as a sort of simplification of the cutting process.

A full 3D-simulation of cutting is costly since the relatively sharp edge of the tool require a very fine mesh. Orthogonal cutting can be modelled as a two dimensional plain strain problem and is therefore more frequently investigated in research [16, 17].

## 2.2 Orthogonal Metal Cutting

Figure 2.1 visualizes the geometry of the process of orthogonal cutting in two dimensions. It can be seen that the cutting tool has two sides, the rake face and the flank face. The rake face where the chip is formed is situated at an angle, called rake angle, relative the normal of the new surface. The flank forms a relief angle (or clearance angle) to the new surface. The difference in height between the original surface and the new surface is called the cutting depth.



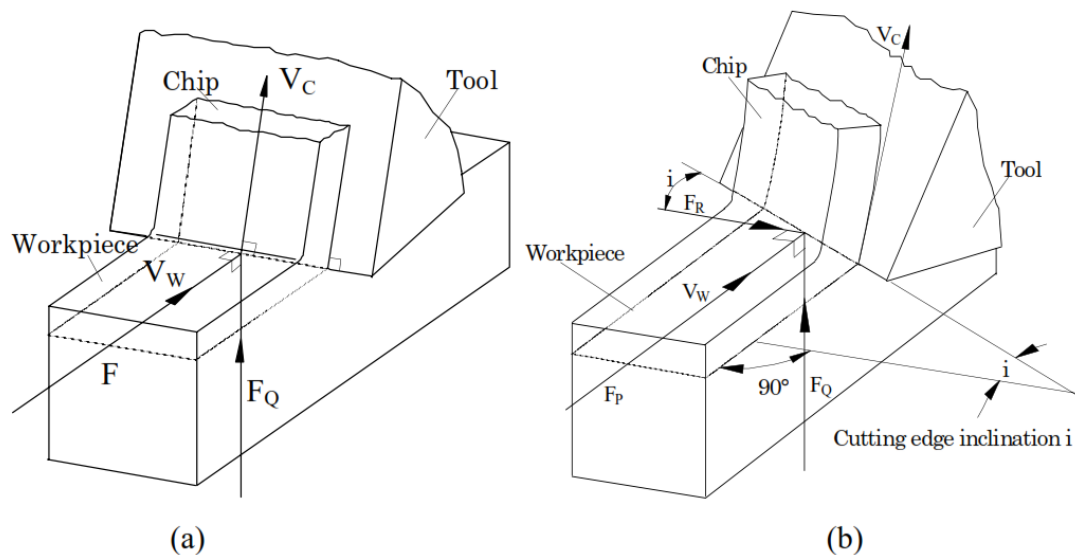
**Figure 2.1: Geometric description of a basic machining process in 2D.  
Figure by Emese [18].**

During cutting as the tool touches the work material, severe plastic deformation occurs within the workpiece material and the excess of material starts flowing

over the rake face of the cutting tool in the form of chip. The zone of plastic deformation known as shear plane lies between the chip and the undeformed work material.

Based on the position of cutting edge, the cutting process can be classified as orthogonal cutting and oblique cutting.

In orthogonal cutting, also known as two-dimensional cutting, the cutting edge is perpendicular to the cutting velocity vector. On the other hand, in oblique cutting, the edge is inclined with the cutting velocity by a certain angle called the inclination angle. Oblique cutting is a common type of three-dimensional cutting used in machining process. Orthogonal cutting is only a particular case of oblique cutting such that any analysis of orthogonal cutting can be applied to oblique cutting [19].



**Figure 2.2: Types of cutting: (a) Orthogonal cutting, (b) Oblique cutting**

As far as practical requirements of rake and other angles are concerned, the ideal conditions of orthogonal cutting are rarely achieved. But analysis of oblique cutting is much more difficult, so focus has been mainly given on the orthogonal cutting with very few exceptions dealing with the mechanics of oblique cutting. The important theories based on orthogonal cutting model which have paved the way for the analysis of chip formation process include Merchant's model [20], Lee and Shaffer's model [21], Oxley's model [22], just to name a few.

## **2.3 Chip Morphology**

Chip formation and its morphology are the key areas in the study of machining process that provide significant information on the cutting process itself. The process variables such as cutting force, temperature, tool wear, machining power, friction between tool-chip interface and surface finish are greatly affected by the chip formation process and chip morphology. Chip is formed due to deformation of the metal lying ahead of the cutting tool tip by shearing process. The extent of deformation that the work piece material undergoes determines the nature or type of chip produced. The extent of deformation of chips again depends upon cutting tool geometry (positive or negative rake angle), workpiece material (brittle or ductile), cutting conditions (speed, feed and depth cut), machining environment (dry or wet machining) [14].

The main chip morphologies (See Figure 2.3) observed in cutting process are described briefly as follows:

### **2.3.1 Discontinuous chip:**

These chips are small segments that adhere loosely to each other. The phenomenon can be attributed to the repeated fracturing that limits the amount of deformation the chip undergoes. Hard and brittle materials like gray cast iron, bronze, brass when machined with larger feed and negative rake cutting tool in the absence of cutting fluid produce discontinuous chips. Machine vibration or tool chatter may cause this type of chips form.

### **2.3.2 Continuous chip:**

Continuous chips are in the form of long coil. These are formed by the continuous plastic deformation of material without fracture ahead of the cutting edge of the tool resulting in a smooth flow of chip up the tool face. Ductile material when machined under low feed and high cutting speed, generally, in the presence of cutting fluid produces such kind of chips. This type of chip is considered ideal for cutting operation because it results in better surface finish

### 2.3.3 Continuous chip with built-up edge:

This kind of chip is not as smooth as that of continuous chip and affects the surface finish adversely. Built-up edge is mostly found when ductile materials are machined under larger feed and lower cutting speed with inadequate or no cutting fluid. BUE results poor surface finish and it shortens tool life. High cutting speeds can be used to eliminate BUE.

### 2.3.4 Cyclic or serrated chips:

These chips are continuous, but, possess a saw-tooth appearance that is produced by a cyclical chip formation of alternating high shear strain followed by low shear strain. Machining of certain difficult to machine metals such as titanium alloys, nickel-base super alloys and austenitic stainless steels are generally characterized by formation of segmented chip formation [23].

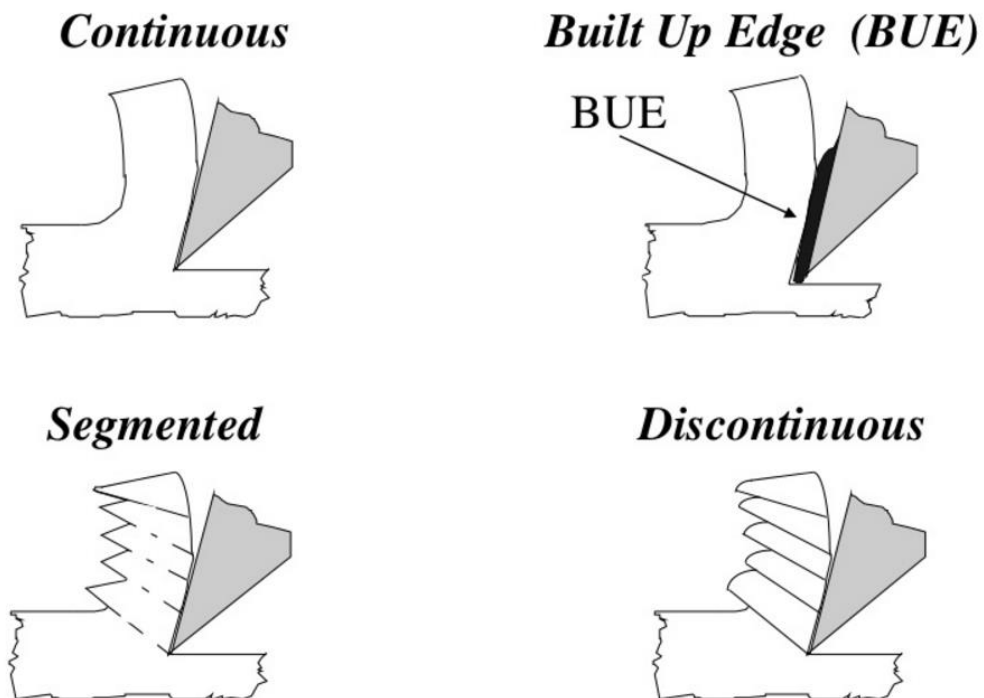
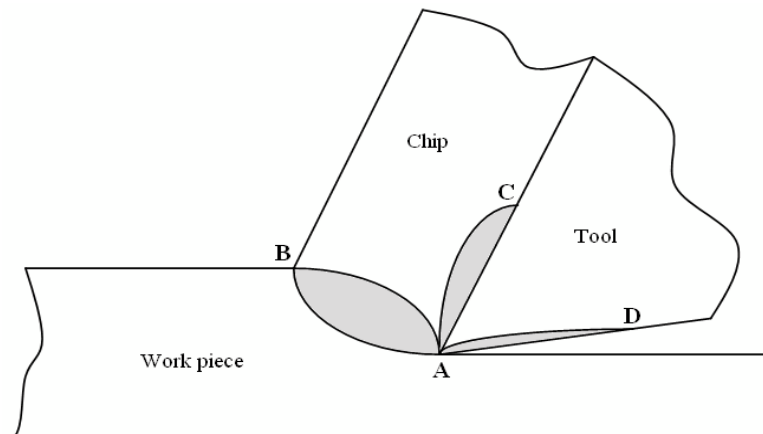


Figure 2.3: Different types of chips in metal cutting

## 2.4 Deformation zones

There are three deformation zones in the cutting process as shown in Figure 2.4;

- Primary shear zone (A-B): The chip formation takes place firstly and mainly in this zone as the edge of the tool penetrates into the workpiece. Material on this zone has been deformed by a concentrated shearing process. In this zone the workpiece material is forced to a quick change in direction under severe shear plastic straining.
- Secondary shear zone (A-C): The chip and the rake face of the tool are in contact from A to C. When the frictional stress on the rake face reaches a value equal to the shear yield stress of the work-piece material, material flow also occur on this zone.
- Tertiary shear zone (A-D): When the clearance face of the tool rubs the newly machined surface deformation can occur on this zone. In the tertiary deformation-zone there exists shearing due to surface friction.

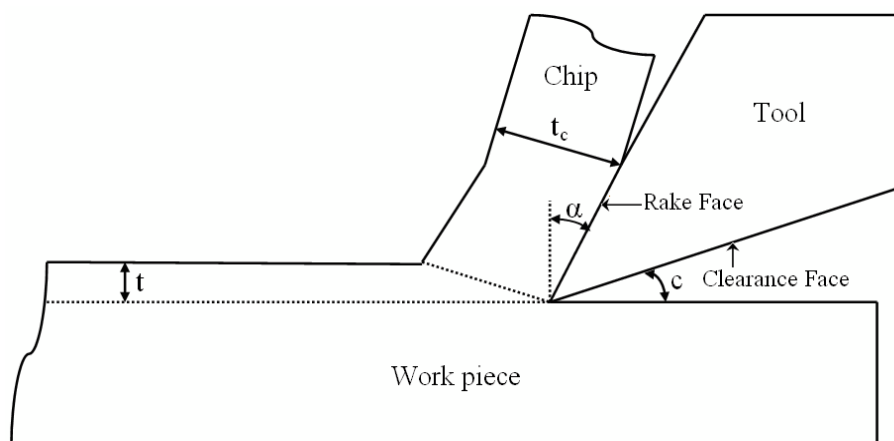


**Figure 2.4: Deformation zones in metal cutting**

## 2.5 Mechanics of Metal Cutting

The first scientific studies of metal cutting were conducted in about 1850, which were aimed at establishing the power requirements for various operations. In the last sixty years researchers have been focused on predicting physical behaviour of metal cutting or developing previous models. Much of the early works are analytical models that represent the basic mechanics of metal cutting.

Orthogonal cutting and tool geometry variables are shown in Figure 2.5.  $t$  is the undeformed chip thickness and it is sometimes called depth of cut.  $t_c$  is the chip thickness. Rake face is the face where chip and tool in contact. Rake angle ( $\alpha$ ) is an angle between the rake face and newly machined surface normal. Clearance face is a surface which the machined surface passes over. Clearance angle ( $c$ ) is an angle between newly machined surface and clearance face. These variables are important because they determine the characteristics of the process.

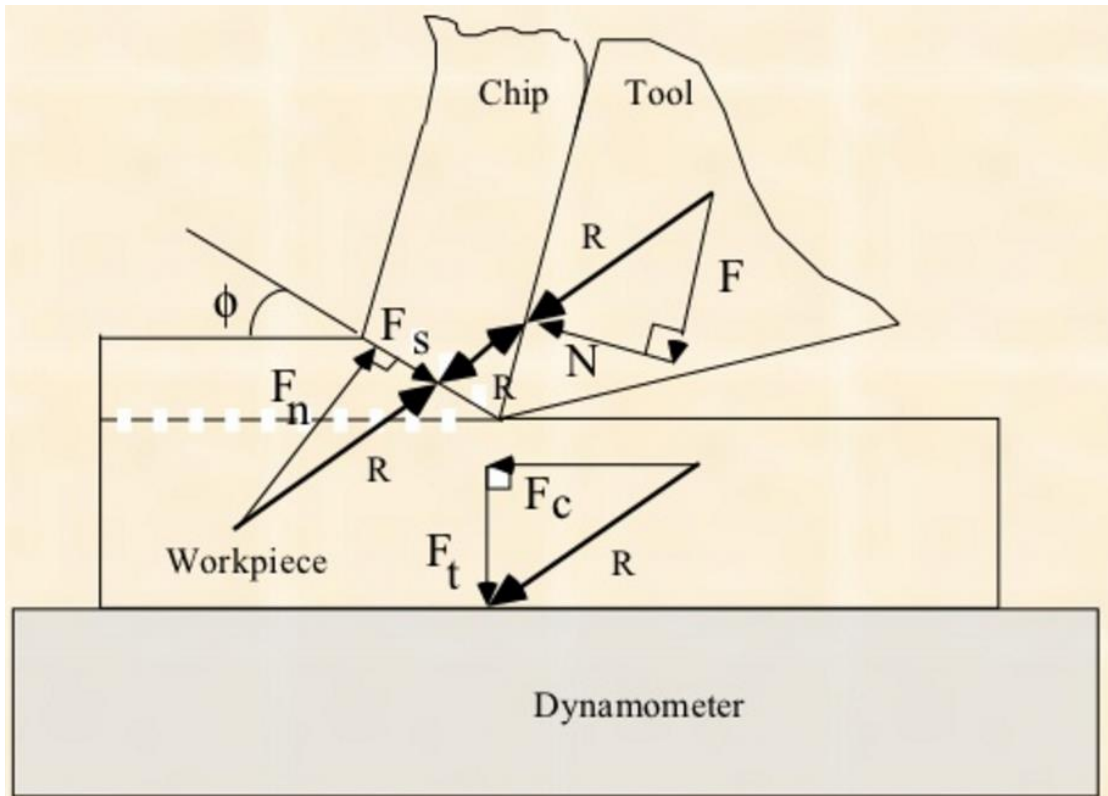


**Figure 2.5: Variables in orthogonal cutting**

A considerable amount of investigations has been directed toward the prediction and measurement of cutting forces. This is because cutting force is a result of the extreme conditions at the tool-workpiece interface and this interaction can be directly related to many other output variables such as generation of heat and consequently tool wear and quality of machined surface as well as chip formation process and the chip morphology [24, 25]. Measurement of forces becomes mandatory at certain cases say, adequate equations are not available, evaluation of effect of machining parameters cannot be done analytically and theoretical models have to be verified.



Several works are available in the literature that makes use of different types of dynamometers to measure the forces. The dynamometers being commonly used nowadays for measuring forces are either strain gauge or piezoelectric type. Though piezoelectric dynamometer is highly expensive, this has almost become standard for recent experimental investigations in metal cutting due to high accuracy, reliability and consistency.



**Figure 2.6: 2D orthogonal cutting forces diagram**

Estimation of forces acting between tool and work material is one of the vital aspects of mechanics of cutting process since it is essential for:

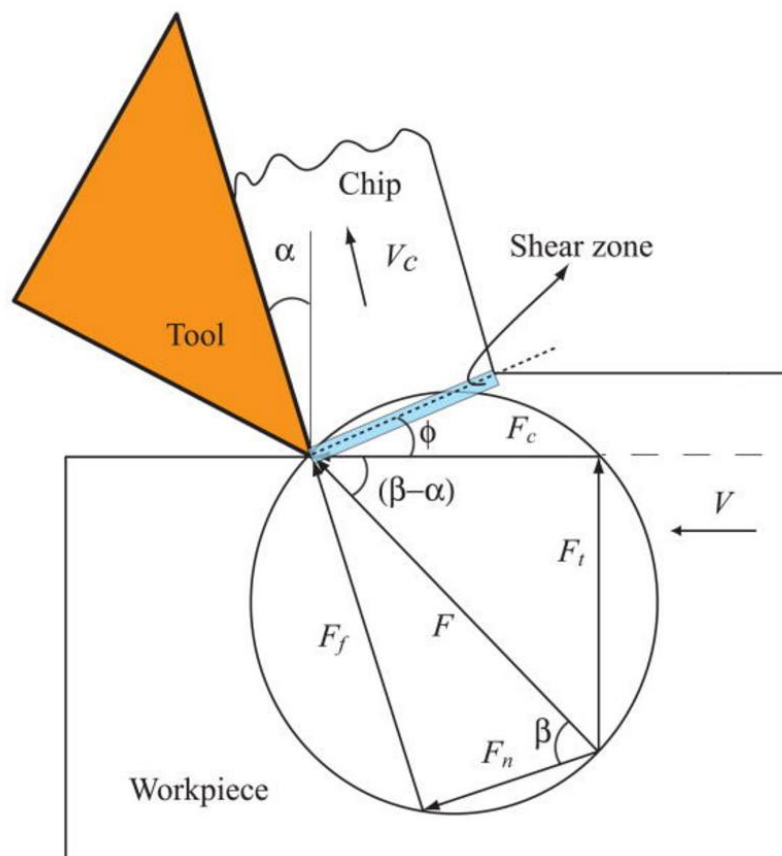
- Determination of the cutting power consumption
- Structural design of machine-fixtured-tool system
- Study of the effect of various cutting parameters on cutting forces
- Condition monitoring of both the cutting tools and machine tools

Analysis of force during machining includes magnitude of cutting forces and their components and location of action of those forces as well as the pattern of the forces, say, static or dynamic.

Merchant (1945) developed an analysis for thin-zone model with the following assumptions:

- i. Tool tip is sharp, and no rubbing occurs between the tool and the work piece.
- ii. The deformation is two dimensional.
- iii. The stresses on the shear plane are uniformly distributed.
- iv. The resultant force  $R$  applied at the shear plane is equal, opposite and collinear to the force  $R$  applied to the chip at the tool-chip interface.

With the help of these assumptions, force diagram of orthogonal cutting can be drawn as shown in Figure 2.5.



**Figure 2.7: Merchant's circle diagram for 2D orthogonal cutting**

The resultant force can be related to the other forces such as friction force  $F$  along the rake face or the cutting force  $F_c$  in the direction of motion. Since the resultant force can change in magnitude and direction, it is better to consider the two force components  $F_c$  (along the work velocity) and  $F_t$  (perpendicular to work velocity). These forces are given as-

$$F_c = \frac{tb\tau \cos(\beta - \alpha)}{\sin \phi \cos(\phi + \beta - \alpha)} \quad (2.1)$$

$$F_t = \frac{tb\tau \sin(\beta - \alpha)}{\sin \phi \cos(\phi + \beta - \alpha)} \quad (2.2)$$

where  $\tau$  is the shear stress on the shear plane assumed uniform over this plane and equal to shear yield stress of the work-piece material,  $\phi$  is the shear angle shown in Figure 2.7.,  $\alpha$  is the tool rake angle,  $t$  is the undeformed chip thickness,  $b$  is the width of cut, and  $\beta$  is the angle between the resultant force and the normal to the rake face. This angle represents the friction angle between the tool and chip. From the Equations (2.1) and (2.2) the cutting forces can be determined if shear stress, friction angle and shear angle are known.

Shear angle is an important variable in metal cutting analysis because it defines the characteristic of deformation. Merchant used the minimum energy principle in his analysis and he assumed that the deformation process adjusted itself to a minimum energy condition. He applied this assumption by equating  $dF_c/d\phi$  to zero for a constant cutting speed

$$\frac{dF_c}{d\phi} = \frac{tb\tau \cos(\beta - \alpha) \cos(2\phi + \beta - \alpha)}{\sin^2 \phi \cos^2(\phi + \beta - \alpha)} = 0 \quad (2.3)$$

Then

$$\phi = \frac{\pi}{4} - \frac{1}{2}(\beta - \alpha) \quad (2.4)$$

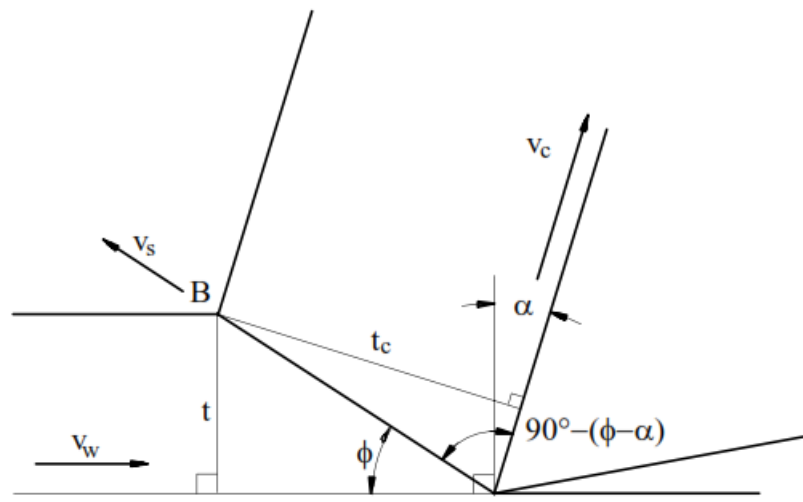
This approach has two doubts. Firstly, he used minimum energy principle, which is not supported by evidence. Secondly, the differentiation assumes  $\beta$  and  $\tau$  are constants but  $\beta$  is not a constant and it is dependent of shear angle.

Shear angle can be determined by using length of cut or chip thickness.

$$\frac{l_{chip}}{l} = \frac{t_c}{t} = r \quad (2.5)$$

Where  $l$  is the length of the cut,  $l_{chip}$  is the length of the chip,  $t$  is the undeformed chip thickness,  $t_c$  is the chip thickness and  $r$  is the chip ratio. By using the geometry of the cut which is shown in Figure 2.8., shear angle can be obtained by

$$\tan \phi = \frac{r \cos \alpha}{1 - r \sin \alpha} \quad (2.6)$$



**Figure 2.8: Shear plane angle in orthogonal cutting**

From the force diagram in Figure 2.6., shear force  $F_s$  and normal force  $F_N$  are given-

$$F_s = F_c \cos \phi - F_t \sin \phi \quad (2.7)$$

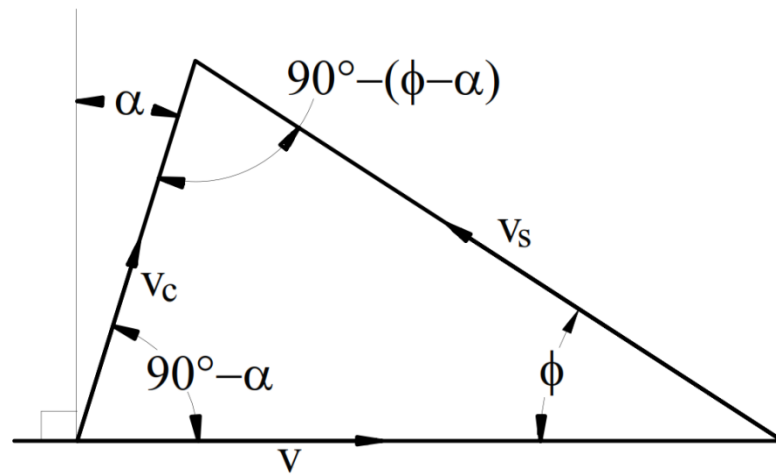
$$F_n = F_c \sin \phi + F_t \cos \phi \quad (2.8)$$

The shear stress  $\tau = \frac{F_s}{A_s}$  and normal stress  $\sigma = \frac{F_n}{A_s}$ , where  $A_s = \frac{bt}{\sin\phi}$

From the velocity diagram in Figure 2.9., chip velocity and shear velocity can be obtained by using:

$$V_c = \frac{\sin\phi}{\cos(\phi - \alpha)} \cdot V = r \cdot V \quad (2.9)$$

$$V_s = \frac{\cos\alpha}{\cos(\phi - \alpha)} \cdot V \quad (2.10)$$



**Figure 2.9: Velocity Vector Diagram**

Shear strain and strain rate in cutting is given by-

$$\gamma = \tan(\phi - \alpha) + \cot\phi \quad (2.11)$$

$$\dot{\gamma} = \frac{V_s}{\Delta y} = \frac{\cos\alpha}{\cos(\phi - \alpha)} \frac{V}{\Delta y} \quad (2.12)$$

where  $\Delta y$  is the thickness of the shear zone.

In Merchant's analysis, the contact between the tool and the chip is Coulomb friction and the following formula for coefficient of friction can be obtained from force diagram shown in Figure 2.7-

$$\mu = \frac{F}{N} = \frac{F_t + F_c \cdot \tan\alpha}{F_c - F_t \cdot \tan\alpha} = \tan\beta \quad (2.13)$$

Where F is the friction force on the rake face, N is the normal force on the rake face.

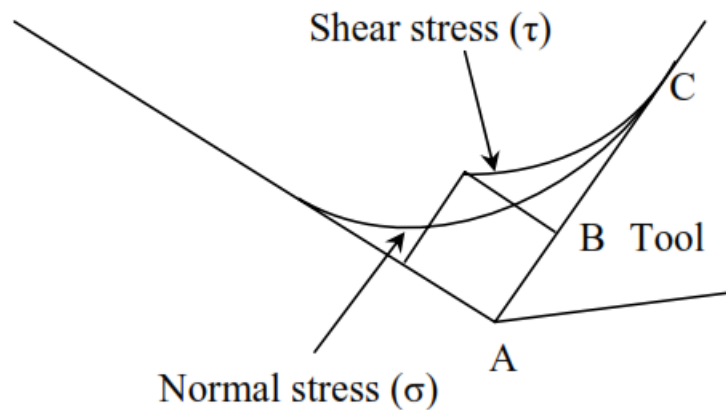
## 2.6 Friction in Metal Cutting

In metal cutting friction between chip and tool interface plays significant role on important process variables such as temperatures and tool wear. Therefore, it has to be studied in detail. Laws of friction was firstly determined by Leonardo da Vinci and later restated by Amonton and Coulomb. These laws are-

- The friction force is proportional to the normal force which means that the coefficient of friction is constant.
- The friction force and the coefficient of friction are independent of the apparent area of the sliding interface.

These laws are valid when normal force N is below a critical certain value. In metal cutting, friction conditions are very different from a simple dry friction and normal force is very high. As the normal force increases, Coulombs' and Amontons' law no longer holds true as the real area of contact between chip and tool rake face increases. Therefore Coulomb's and Amontons' law can not represent the friction phenomenon in metal cutting.

Friction in metal cutting was studied in detail by many researchers. To achieve this goal, researchers study the contact and friction stress on the rake face by using direct measurement. Usui and Takeyama (1960) measured the distribution of the shear ( $\tau$ ) and the normal ( $\sigma$ ) stress on the rake face of the tool. As shown in Figure 2.10., they found the shear stress remains constant over about the half of tool-chip contact nearest the cutting edge but it decreases to zero over the rest, reaching zero of course at point C where the chip leaves contact with the tool. The normal stress was found to decrease and reach zero from the cutting edge to point C. Zorev (1963) found also similar results from his experiments.



**Figure 2.10: Distribution of shear and normal stress on the rake face**

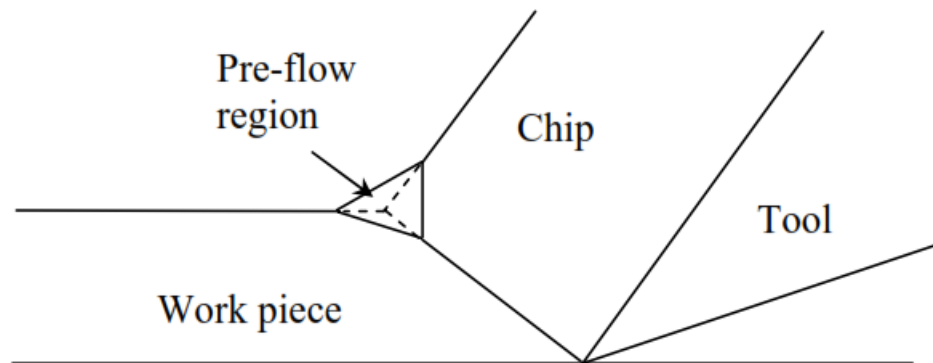
Over the length AB, normal stress is sufficiently high and contact area to total area ratio approaches unity and metal adheres to the rake face. This region is called the sticking region and plastic deformation occurs in the chip. The coefficient of friction in the sticking region is not constant, but it depends on the magnitude of the normal load. The value of the coefficient of friction in this region is lower than the value under sliding friction conditions. In the length from B to C, which extends from the end of the sticking region to the point where chip loses contact with the tool rake face, the contact area to total area ratio is less than unity, so coefficient of friction is constant, and sliding friction occurs.

The measured coefficient of friction in metal cutting is an average value based on both regions. Any changes in cutting conditions that may change lengths AB and BC will change the value of coefficient of friction.

## 2.7 Shear Stress in Metal Cutting

The shear stress in metal cutting is higher than the yield stress of determined from tensile test on work materials. Rubbing effect and the pre-flow region existence are two reasons of this situation. Rubbing effect on the clearance of the tool introduces a force which is measured but does not contribute to the shearing process. Secondly, a pre-flow region is present in most of the cutting processes that

extends the length of the shear plane that assumed in analysis as shown in Figure 2.11



**Figure 2.11: Pre-flow region**

In addition to these two reasons, high normal stress can increase the yield shear stress on the shear plane during cutting. At low cutting speeds, work hardening of the material is also must be taken into account while determining the shear stress. Strain rate and temperature are normally causing opposing effects on yield stress of the material. Since both strain rate and temperature are relatively high in metal cutting operations, sometimes it can be thought as they cancel each other but recent considerations of the mechanism of yield at very high strain rates indicate that the high strain rate may have the effect of increasing yield stress above the static yield value.

## **2.8 Chip Formation Process**

The chip formation process, which starts in the primary deformation zone, is by some authors described as a material flow around the tool tip while by others it is described as a crack that moves ahead of the tool tip splitting the material like in splitting of wood [15].

The physics of chip separation is a key issue that has not yet been fully understood [27]. A large number of different (but internally related) physical phenomena, e.g. large plastic strain, damage, friction, heat generation, exists in the deformation zone where the chip separation occur.



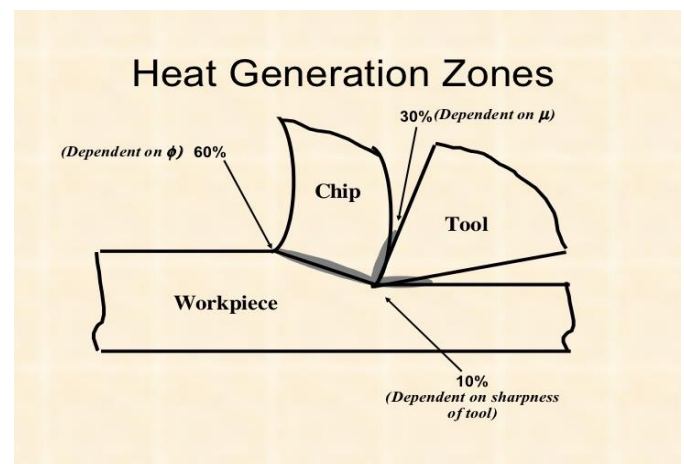
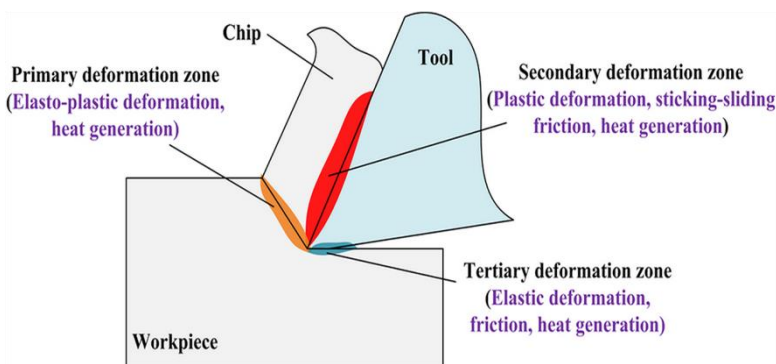
The process of chip - workpiece separation can be described as follows. In the beginning of the process a stress concentration in front of the tool tip is built up when the tool moves towards the workpiece. When these stresses reaches a certain limit an elasto-plastic zone forms in the workpiece (considering ductile material). The sizes of the elastic and the plastic parts of the zone is related to the ductility of the workpiece material [9]. For more brittle materials it is assumed that a crack opens up in front of the cutting edge [27].

Often the cutting process can be characterized by the type of chip produced. General categories of chips are continuous, discontinuous, continuous with built-up edges and shear-localized as can be seen in Figure 2.3. The different types of chips indicates different types of physical processes and which type is formed is dependent on cutting and material conditions.

## 2.9 Temperature in Metal Cutting

During a metal cutting operation, high temperatures are generated because of plastic deformation of work piece material and friction along the tool/chip interface. Determination of temperatures in tool, chip and work piece is important for process efficiency because these temperatures have a great influence on the rate of tool wear, strength of work piece material, mechanics of chip formation, surface integrity, cutting forces, etc.

Heat sources in metal cutting are shown in Figure 2.12. There are three Heat source namely as Primary, Secondary and Tertiary Heat source. Primary zone occurs on shear plane due to intensive plastic deformation. The shear plane temperature is very important because it influences flow stress of work piece material and temperatures on the tool face.



**Figure 2.12: Locations of heat sources in metal cutting**

Secondary or Frictional heat source localises at the tool-chip interface. Temperature of rake face is the maximum temperature in real machining operations and it causes tool wear. Another frictional heat source is Tertiary heat source that is generated at the contact between the flank face of the tool and the work piece due to tip radius of the cutting tool.

Thermal studies in metal cutting have focused on determining the heat generation, its distribution in the cutting area and the maximum temperature. There are three types of methods used to achieve results about temperatures-

- Analytical: In the analytical studies, empirical correlations have been used to determine heat generation and temperature distribution. Analytical calculations have been done under simplified assumptions.
- Experimental: The experimental techniques such as thermo couple with tool/chip pair, thermal camera, etc. have been providing thermal distribution of cutting zone. Results of the experimental works mainly depend on calibration of the instruments used.
- Numerical: Distribution of temperature on the cutting zone has been obtained by using finite element, finite difference and boundary elements methods.

## CHAPTER 3

### LITERATURE REVIEW: THEORY AND BASICS OF LINEAR ELASTIC FRACTURE MECHANICS

#### 3.1 Stress Distribution Around a Crack

The cracks in mechanical components subject to applied loads behave very close to what is observed when there are notches, which are responsible for stress concentration due to reduction of area against the nominal area. The geometry of the crack creates high stress concentrations in its tip. This behaviour is illustrated in Figure 3.1. Due to the high tension observable on the edge of the crack, a plastic zone appears. However, following the LEFM theory, the plastic behaviour is not taken into account, and tension is given by an ideal crack following the linear elastic model. Consequently, the LEFM reveals a large gap, by not taking into account areas that could be in the plastic domain [28].

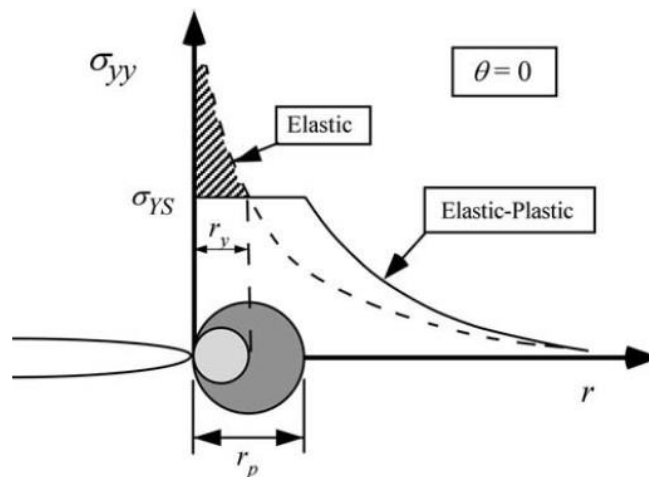
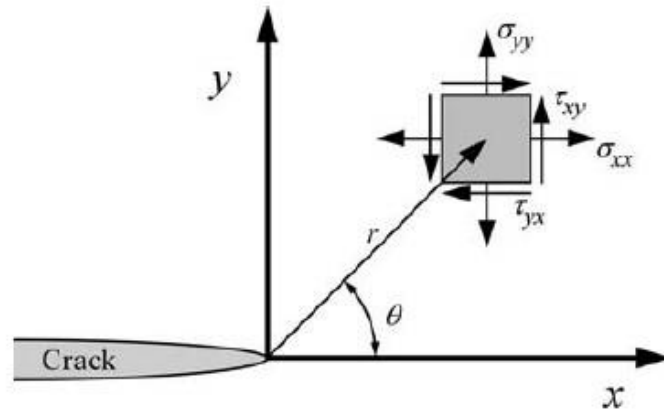


Figure 3.1: Real and ideal crack tension behaviour [28]

Consulting Anderson [28], for cracked geometries subjected to external forces, it is possible to derive closed-forms or analytical expressions for the stresses in the body, assuming the LEFM. Irwin [29], Sneddon [30], Westergaard, and Williams were among the first to publish such solutions.



**Figure 3.2: Stresses near the crack tip and polar coordinates [1]**

Considering a polar coordinate system,  $(r, \theta)$ , with the origin at the crack tip represented on Figure 3.2, it can be shown that the stress field in any linear elastic cracked body is given by,

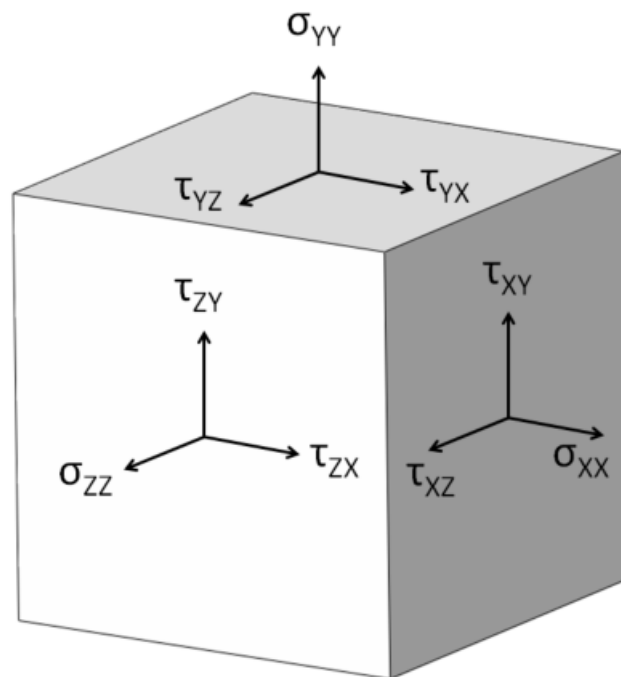
$$\sigma_{ij} = \left(\frac{k}{\sqrt{r}}\right)f_{ij}(\theta) + \sum_{m=0}^{\infty} A_m r^{m/2} g_{ij}^{(m)}(\theta) \quad (3.1)$$

Where  $\sigma_{ij}$  is the stress tensor,  $k$  a constant and  $f_{ij}$  a dimensionless function of  $\theta$  in the leading term. For the higher order terms,  $A_m$  is the amplitude and a dimensionless function of  $\theta$  for the  $m$ th term. It should be noticed, that the solution for any given configuration contains a leading term that is proportional to  $1/\sqrt{r}$ . As  $r \rightarrow 0$ , the leading term goes to infinity, but the other terms remain finite or approach zero. Thus, stress near the crack tip varies with  $1/\sqrt{r}$ , independently of the geometries. It can also be shown that displacement near

the crack tip varies with  $\sqrt{r}$ . Equation (3.1) describes also a stress singularity, since stress is asymptotic to  $r = 0$ .

### 3.2 Plane stress versus plane strain

A common practice in stress analysis is to assume a specimen is in a two-dimensional, planar state of stress. This two-dimensional state can be described as either plane stress or plane strain. Plane stress is defined as a state of stress in which the normal stress,  $\sigma_z$ , and the shear stresses  $\sigma_{xz}$  and  $\sigma_{yz}$  directed perpendicular to the x-y plane are assumed to be zero [28]. More simply put, two faces of a cubic element are stress free [31] (see Figure 1).



**Figure 3.3: Stress tensor at a point in space**

Plane stress occurs most often for very thin isotropic plates subjected to only in-plane loads [28]. Considering a cracked plate, the region near the crack typically experiences plane stress conditions if the crack length is large compared to the plate thickness [32]. Conversely, plane strain is described by the condition in which the strain normal to the x-y plane,  $\epsilon_z$ , and the shear strains  $\gamma_{xz}$  and  $\gamma_{yz}$  are assumed to be zero. Plane strain often occurs when a specimen is much thicker in one direction (for

example the z direction) than in the other two (x and y) directions [28]. For a cracked plate plane strain conditions typically prevail near the crack when the crack length is small compared to the plate thickness [32]. However, real structures seldom behave in purely plane strain or plane stress ways. This is especially true in cracked structures, where local constraints near the crack tip cause increases in stress intensity. This increase in stress intensity is often ignored in analysis, which usually assumes constant stress through the thickness [33]. Stresses are not uniform through the thickness, and can only be accurately analyzed using three-dimensional analysis. Bakker showed that a cracked plate under plane stress undergoes a change to plane strain behavior near the crack tip [33]. He states that this change occurs at  $r/t < 0.5$ , and is confirmed by Nakamura for a sufficiently thin plate [34]. Nakamura goes further to say that this transitional region extends to a radial distance from the crack front of about one and one-half times the plate thickness. Bakker [33] adds that the radial position where the plane stress to plane strain transition takes place strongly depends on the position in the thickness direction.

For the plane stress and plane strain:-

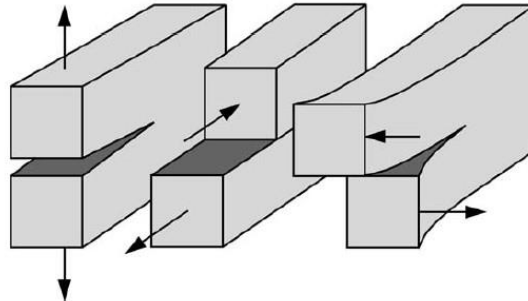
$$\begin{aligned} \sigma_{xx}, \sigma_{yy}, \tau_{xy} &\neq 0 \\ \sigma_{zz} = \tau_{zx} = \tau_{zy} &= 0 && \text{(plane stress)} \\ \epsilon_{xx}, \epsilon_{yy}, \tau_{xy} &\neq 0 \\ \epsilon_{zz} = \tau_{yx} = \gamma_{zy} &= 0 && \text{(plane strain)} \end{aligned}$$

### 3.3 Loading Modes

In fracture mechanics, there are three types of loading that a crack can experience, presented on Figure 3.4.

Mode I loading, where the principal load is applied in the normal direction to the crack plane, opening the crack (a traction mode). Mode II corresponds to an in-plane shear loading and tends to slide one crack face over the other (a shear mode). Mode III refers to the out-of-plane shear (a torsion mode).

A cracked body can be loaded in any one of these modes, or a combination of two or three modes. For each of these modes, it can be deduced a stress intensity factor, which are presented next.



**Figure 3.4: Loading modes I, II and III [1]**

### 3.4 Stress Intensity Factors

The stress intensity factor ( $K$ , or  $SIF$ ) was first proposed by Irwin in 1957 and can be thought of as a measure of the effective local stress at the crack tip. An increasing  $K$  indicates the stress near the crack tip is increasing. With this linear elastic fracture mechanics approach of characterizing the crack tip stresses, small amounts of plasticity may be viewed as taking place within the crack tip stress field and neglected for the characterization. The stress intensity factors are used as a measure that quantifies the severity of a crack relative to others cracks. They are so, of extreme importance for the cracks study. They are also related to the mechanisms of crack initialization but also their propagation, and in some cases, the stress intensity factor may reach an extreme value: the fracture toughness  $K_C$ , leading to the fracture of the components.

$K$  is usually expressed in the following units:

$Mpa\sqrt{m}$  for metric units

$ksi\sqrt{in}$  for imperial units

$K$  can be determined using closed-form solutions, finite element analysis, and a number of other techniques. The solutions relate the remote loading, geometry of the specimen, and the crack size to the stress intensity factor,  $K$ . Using the stress

intensity factor in design requires knowledge of the critical stress intensity factor or fracture toughness ( $K_C$ ).

The critical stress intensity factor or fracture toughness ( $K_C$ ) is a mechanical property that measures a material's resistance to fracture. Fracture toughness is used in structural integrity assessment, damage tolerance design, fitness-for-service evaluation, and residual strength analysis.  $K_C$  is further expressed according to the loading mode, such as  $K_{IC}$ ,  $K_{IIC}$ ,  $K_{IIIC}$  for modes one, two, and three, respectively. When the stress intensity factor reaches the material's fracture toughness an existing crack will undergo unstable crack extension. Since  $K_C$  is material specific its value must be determined for each material of concern. Further,  $K_C$  can vary with temperature, component thickness, and strain rate. Table 3.1 lists critical stress intensity factors for some common materials.

**Table 3.1: Critical stress intensity factors for common materials**

	$K_C$	
	$Mpa\sqrt{m}$	$ksi\sqrt{in}$
Steel AISI 4340	59	53.7
Stainless Steel AISI 403	77	70.1
Aluminum 2024-T851	23	20.9
Titanium Ti-6Al-6V	66	60.1

Each mode of loading produces the  $1/\sqrt{r}$  singularity at the crack's tip, but the proportionality constants  $k$  and  $\bar{f}_{ij}$  depend on the mode. For further considerations it is important to substitute  $k$  of Equation (3.1) by the stress intensity factor  $K$ , where  $K=k\sqrt{2\pi}$ . The stress intensity factor is usually given with a subscript to denote the mode of loading, i.e.,  $K_I$ ,  $K_{II}$ , or  $K_{III}$ .

Considering the LEFM, the stress fields ahead of a crack tip in an isotropic linear elastic material can be written as,



$$\lim_{r \rightarrow 0} \sigma_{ij}^{(I)} = \frac{K_I}{\sqrt{2\pi r}} f_{ij}^{(I)}(\theta) \quad (3.2)$$

$$\lim_{r \rightarrow 0} \sigma_{ij}^{(II)} = \frac{K_{II}}{\sqrt{2\pi r}} f_{ij}^{(II)}(\theta) \quad (3.3)$$

$$\lim_{r \rightarrow 0} \sigma_{ij}^{(III)} = \frac{K_{III}}{\sqrt{2\pi r}} f_{ij}^{(III)}(\theta) \quad (3.4)$$

For modes I, II, and III, respectively.

In a mixed-mode problem (i.e., when more than one loading mode is present), the individual contributions to a given stress can be summed:

$$\sigma_{ij}^{(Total)} = \sigma_{ij}^{(I)} + \sigma_{ij}^{(II)} + \sigma_{ij}^{(III)} \quad (3.5)$$

Equation (3.5) results from the principle of linear superposition.

Considering this thesis will focus on loading Mode I, it is shown below both the stress and displacement field ahead a crack tip,

$$\sigma_{xx} = \frac{K_I}{\sqrt{2\pi r}} \cos(\theta) \left[ 1 - \sin\left(\frac{\theta}{2}\right) \sin\left(\frac{3\theta}{2}\right) \right] \quad (3.6)$$

$$\sigma_{yy} = \frac{K_I}{\sqrt{2\pi r}} \cos\left(\frac{\theta}{2}\right) \left[ 1 + \sin\left(\frac{\theta}{2}\right) \sin\left(\frac{3\theta}{2}\right) \right] \quad (3.7)$$

$$\tau_{xy} = \frac{K_I}{\sqrt{2\pi r}} \cos\left(\frac{\theta}{2}\right) \sin\left(\frac{\theta}{2}\right) \cos\left(\frac{3\theta}{2}\right) \quad (3.8)$$

For Plain Stress,

$$\sigma_{zz} = 0$$

For Plain Strain,

$$\sigma_{zz} = \nu(\sigma_{xx} + \sigma_{yy})$$

Where  $(r, \theta)$  are the polar coordinates,  $\nu$  the Poisson ratio. The remaining components of the stress tensor are zero.

### 3.5 Toughness of material

Toughness describes the amount of total energy required for the material break. In general, if the material requires a lot of energy before breaking, then it looks like “tough”. If only a little energy is needed to break the material it is weak or brittle, depending on whether the material exhibits a yielding phenomenon followed by a plastic behaviour as load is increased or not. Toughness is the resistance opposed by material to be broken. When crack propagates through the structure, fracture occurs. The amount of energy absorbed during the fracture depends on the size of the component, which is broken. The amount of energy absorbed *per unit area* of crack is constant for a given material corresponds to its toughness. High toughness is particularly important for components, which may suffer impact (cars, toys, bikes, impact tools and hammer), or for components where a fracture would be catastrophic (pressure vessels, aircraft). Toughness varies with temperature, some materials change from being tough to brittle as temperature decreases (e.g. some steels, rubber). A famous example of this problem in steels was the battleships that broke in two in cold seas during the Second World War; some dangerous embitterment occurs in hydrogen storage [36].

Detailed toughness tests use specimens with initial cracks, and measure the energy per unit area as the crack grows. This can be applied to all materials, and the selection charts show toughness data measured this way. Simple toughness tests use specimens of fixed size with a machined notch, and just measure the energy needed to break the specimen. Crack grows as soon as the crack tip stress exceeds a critical value. The SIF determines the amplitude of the crack tip stress for a given geometry and loading case, thus allowing to assume that a crack grows when  $K$  reaches a critical value. This implies that a crack growth criterion can be formulated, where the SIF is compared to this critical value. Therefore value of the SIF has to be calculated. The critical value has to be found in some experimental measurements. It is referred

to as “Fracture Toughness “,  $K$ , where an additional subscript is used to describe the fracture mode analysed,  $K_{Ic}$ ,  $K_{IIc}$ ,  $K_{IIIc}$

### 3.6 The Griffith Energy Balance

According to the first law of thermodynamics, when a system goes from a non-equilibrium state to equilibrium, there is a net decrease in energy [28].

In 1920, Griffith applied this idea to the formation of a crack [37]:

“It may be supposed, for the present purpose, that the crack is formed by the sudden annihilation of the tractions acting on its surface. At the instant following this operation, the strains, and therefore the potential energy under consideration, have their original values; but in general, the new state is not one of equilibrium. If it is not a state of equilibrium, then, by the theorem of minimum potential energy, the potential energy is reduced by the attainment of equilibrium; if it is a state of equilibrium, the energy does not change.”

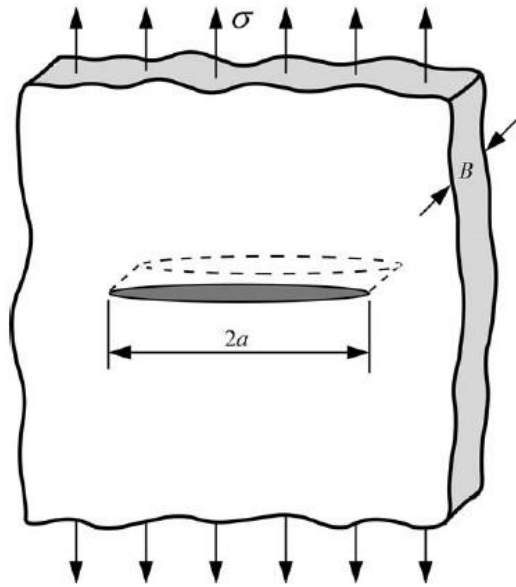
The total energy must decrease or remain constant to form a crack or to allow its propagation. Thus the critical conditions for fracture can be defined as the point where the crack growth occurs under equilibrium conditions, with no net change in the total energy.

Consider a wide plate subjected to a constant stress load with a crack ‘ $2a$ ’ long (Figure 3.5). In order for this crack to increase in size, sufficient potential energy must be available in the plate to overcome the surface energy  $\gamma_s$  of the material. The Griffith energy balance for an incremental increase in the crack area  $dA$ , under equilibrium conditions, can be expressed as follow:

$$\frac{d\Phi}{dA} = \frac{d\Pi}{dA} + \frac{dW_s}{dA} = 0 \quad (3.9)$$

or

$$\frac{d\Pi}{dA} = -\frac{dW_s}{dA} \quad (3.10)$$



**Figure 3.5: A through-thickness crack in an infinitely wide plate subjected to a remote tensile stress [28]**

Where  $\Phi$  is the total energy,  $\Pi$  the potential energy supplied by the internal strain energy and external forces and  $W_s$  the work required to create new surfaces.

From Anderson [28], for the cracked plate illustrated

in Figure 3.5, Griffith [37] used the stress analysis of Inglis to show that,

$$\Pi = \Pi_0 - \frac{\pi\sigma^2 a^2 B}{E} \quad (3.11)$$

Where  $\Pi_0$  is the potential energy of an uncracked plate and  $B$  is the plate thickness. Since the formation of a crack requires the creation of two surfaces,  $W_s$  is given by-

$$W_s = 4aB\gamma_s \quad (3.12)$$

With  $\gamma_s$  the surface energy of the material. Thus,

$$-\frac{d\Pi}{dA} = \frac{\pi\sigma^2 a}{E} \quad (3.13)$$

And,

$$\frac{dW_s}{dA} = 2\gamma_s \quad (3.14)$$

Solving for the fracture stress,

$$\sigma_f = \left(\frac{2E\gamma_s}{\pi a}\right)^{1/2} \quad (3.15)$$

It is important to have in mind the distinction between crack area and surface area. The crack area is defined as the projected area of the crack ( $2aB$  in the present example), but since a crack includes two matching surfaces, the surface area is  $2A$ .

### 3.7 The Energy Release Rate

Irwin [35], in 1956, proposed an energy approach for fracture that is essentially equivalent to the Griffith model, except that Irwin approach is in a form more convenient for solving engineering problems.

Irwin defined an energy release rate  $G$ , which is a measure of the energy available for an increment of crack extension:

$$G = -\frac{d\Pi}{dA} \quad (3.16)$$

The term rate, as it is used in this context, does not refer to a derivative with respect to time;  $G$  is the rate of change in potential energy with the crack area. Since  $G$  is obtained from the derivative of a potential, it is also called the crack extension force or the crack driving force. According to Equation (3.13), the energy release rate for a wide plate in plane stress with a crack of length  $2a$  (Figure 3.5) is given by,

$$G = \frac{\pi\sigma^2 a}{E} \quad (3.17)$$

Referring to the previous section, the crack extension occurs when  $G$  reaches a critical value,

$$G_c = \frac{dW_s}{dA} = 2\gamma_s \quad (3.18)$$

Where  $G_c$  is also a measure of the fracture toughness of the material.

At this moment, it must be said the energy release rate is extremely important for this thesis. This is justified by its direct relationship with the stress intensity factor.

Irwin's showed that for linear elastic materials, under loading Mode I, it may be written,

$$G = \frac{K_I^2}{E'} \quad (3.19)$$

Where for Plane Stress,

$$E' = E$$

And for Plain Strain,

$$E' = \frac{E}{1-\nu^2}$$

Nevertheless, the energy release rate is still not enough and practical to get the value of the stress intensity factor.

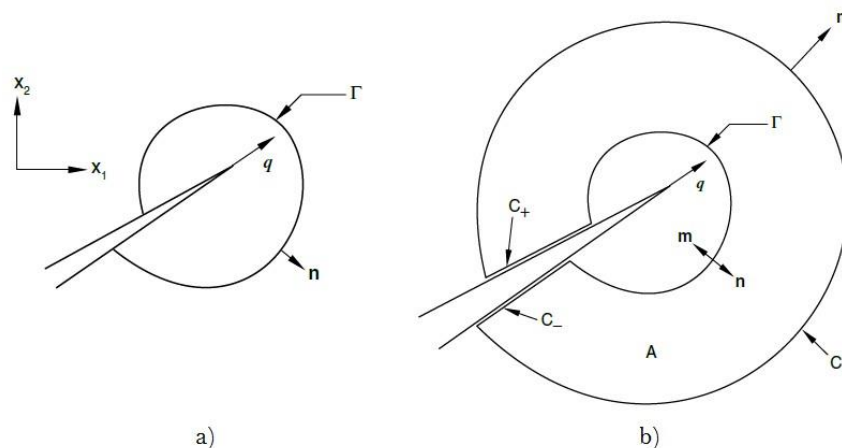
### 3.8 The J-Integral

In the previous section, it was showed the basis behind the energy release rate, with a direct relation with the stress intensity factor. Even the energy release rate is a simple concept, it is not obvious how to deduce it with the finite element method. Fortunately, there is another concept in the LEFM theory, called the J-Integral, which may be calculated numerically and reveals itself very useful because in the context of LEFM, the J-Integral is equal to the energy release rate  $G$ .

#### J-Integral Calculation

As said before, the stress intensity factor can be calculated by the energy release rate  $G$ , which in this thesis context is equal to the J-Integral.

The J-Integral is a contour integral for bi-dimensional geometries (see Figure 3.6). Its definition is easily extended to three-dimensional geometries, and it is used to extract the stress intensity factors.



**Figure 3.6: a) 2D contour integral, b) 2D closed contour integral [35]**

For the two-dimensional case, the J-Integral is given by,

$$J = \lim_{\Gamma \rightarrow 0} \int_{\Gamma} n \cdot H \cdot q d\Gamma \quad (3.20)$$

Where  $\Gamma$  is the contour containing the crack tip,  $n$  is the exterior normal to the contour, and  $q$  is the unitary vector within the virtual displacement direction of the crack.

The function  $H$  is defined by,

$$H = WI - \sigma \cdot \frac{\partial u}{\partial x} \quad (3.21)$$

Where  $W$  is the elastic strain energy,  $I$  the identity tensor,  $\sigma$  the stress tensor and  $u$  the vector of displacements.

The contour connects the two crack faces and encloses the crack tip. This is shown in Figure 3.6a). The contour tends to zero, until it only contains the crack tip (Equation (3.20)). The exterior normal  $n$  moves along the integration while  $q$  stands fixed in the crack tip.

It is very important to note the J-Integral is independent of the chosen path for elastic materials in the absence of imposed forces in the body or tension applied on the crack, so the contour does not need to contract itself on the crack, but it has only to enclose the crack tip.

The two dimensional integral may be rewritten as a closed bi-dimensional contour integral as the following [38],

$$J = - \oint_{C_+C_-+C_++\Gamma} m \cdot H \cdot \bar{q} d\Gamma - \int_{C_++C_-} t \cdot \frac{\partial u}{\partial x} \cdot \bar{q} d\Gamma \quad (3.22)$$

Where the line integrals are performed in a closed contour, which is an extension of  $\Gamma$ .  $C_+$  and  $C_-$  are contours along the crack faces, enclosed by  $C$ . The normal  $m$  had to be introduced as the unitary exterior normal to the contour  $C$ , respecting  $m = -n$ . The function  $\bar{q}$  had also to be introduced, being a unitary vector applied in the direction of the virtual extension of the crack tip, which respects  $\bar{q} = q$  in  $\Gamma$  and vanishes in  $C$ .



The J-Integral may be now transformed in a surface integral by the divergence theorem properties, yielding to,

$$J = \int_S \left( \frac{\partial}{\partial x} \right) \cdot (H \cdot \bar{q}) dS \quad (3.23)$$

Where  $S$  is the area in the closed domain. The equilibrium forces equation is,

$$\left( \frac{\partial}{\partial x} \right) \cdot \sigma + f = 0 \quad (3.24)$$

Where  $\sigma$  is the tension tensor, and  $f$  the volume forces. And the energy strain gradient, for an homogeneous material with constant properties is,

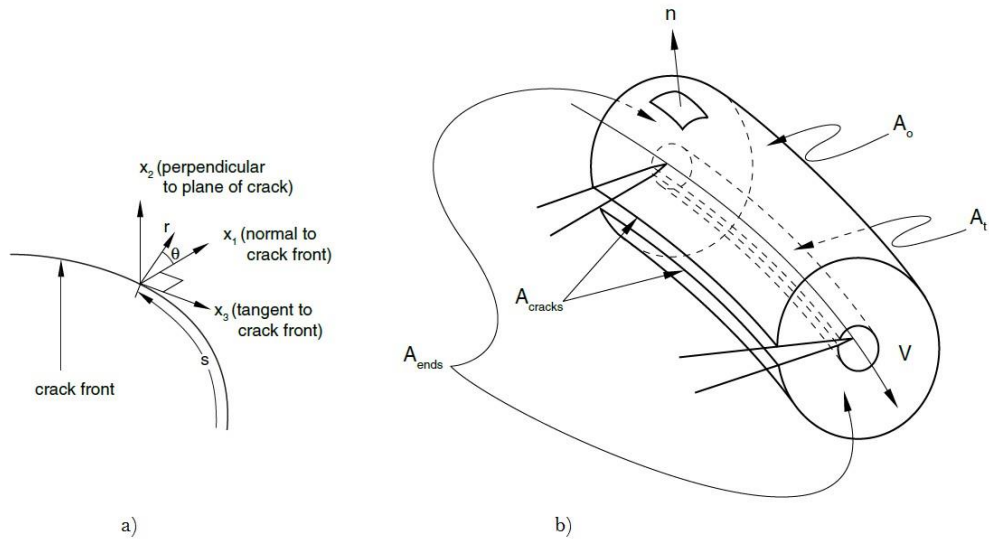
$$\left( \frac{\partial W(\epsilon)}{\partial x} \right) = \frac{\partial W}{\partial \epsilon} \frac{\partial \epsilon}{\partial x} = \sigma \frac{\partial \epsilon}{\partial x} \quad (3.25)$$

Where  $\epsilon$  is the mechanical strain.

Considering these two previous equations, the J-Integral may now be written as,

$$J = - \int_S \left( \left[ H \frac{\partial \bar{q}}{\partial x} + \left( f \cdot \frac{\partial u}{\partial x} \right) \cdot \bar{q} \right] \right) dS \quad (3.26)$$

The bi-dimensional equation for the J-Integral is easily extended to a three dimensional formulation. The J-Integral has to be defined in order to a parametric variables, in the crack front, in such manner  $\mathbf{J}(s)$  is defined by a function which characterizes the bi-dimensional J-Integral for each point placed in the path defining the crack front, which is also described parametrically in order to  $s$  (Figure 3.7).



**Figure 3.7: a) Local coordinates system, b) 3D J-Integral [8]**

The local system of Cartesian coordinates is placed in the crack front. See Figure 3.7a). The axis  $x_3$ , runs tangentially the crack,  $x_2$  is defined perpendicular to the crack front. In this formulation,  $x_1$  will always be directed forward at the crack front.  $x_1$  and  $x_2$  define a perpendicular plane to the crack front.  $J(s)$  is so described in the  $x_1 x_2$  plane.

From Figure 3.7, it is obvious that for the three-dimensional case, each infinitesimal 2D contour must be integrated, for each position of  $s$ , along the path described by the crack front in order to obtain a volume J-Integral.

### **Stress Intensity Factors Extraction**

Having defined the procedure to obtain the J-Integral, for both, bi-dimensional and three-dimensional crack geometries, it becomes necessary to extract the stress intensity factors. Consulting Abaqus® Documentation [35], for a linear elastic material, the J-Integral is related to the stress intensity factors by the following relation,

$$J = \frac{1}{8\pi} K^T P^{-1} K \quad (3.27)$$

With  $K = [K_I, K_{II}, K_{III}]^T$  and  $P$  the pre-logarithmic energy factor tensor [39, 40]. For homogeneous and isotropic materials this equation may be simplified in the form,

$$J = \frac{1}{E'}(K_I^2 + K_{II}^2) + \frac{1}{2G}K_{III}^3 \quad (3.28)$$

Where for Plane Stress,

$$E' = E$$

And for Plain Strain,

$$E' = \frac{E}{1-\nu^2}$$

At last, for pure Mode I loading, the relation between the J-Integral and the stress intensity factor is given by,

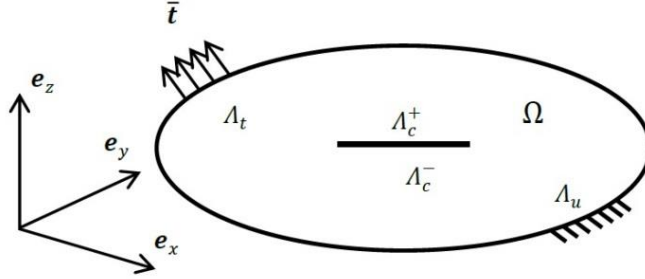
$$J = \left(\frac{K_I^2}{E'}\right) \quad (3.29)$$

Which is exactly the equation presented in section 3.7

### 3.9 The Finite Element Method

#### 3.9.1 System of Equations

In this section, are presented the governing equations of the finite elements, used for the analyses.



**Figure 3.8: FEM domain and boundary conditions [32]**

Considering the domain  $\Omega$  of Figure 3.8, the border  $\Lambda$  may be divided in four independent borders:  $\Lambda_t$  with tension applied,  $\Lambda_u$  with imposed displacement, and the last two domains,  $\Lambda_c^+$  and  $\Lambda_c^-$ , representin the crack faces.

The equilibrium equations and boundary conditions are,

$$\begin{aligned}
 \nabla \sigma + f &= 0 \text{ in } \Omega \\
 \sigma \cdot n &= \bar{t} \text{ in } \Lambda_t \\
 \sigma \cdot n &= 0 \text{ in } \Lambda_c^+ \\
 \sigma \cdot n &= 0 \text{ in } \Lambda_c^- \\
 u &= u_{imp} \text{ in } \Lambda_u
 \end{aligned}
 \tag{3.30}$$

Where  $f$  represents the volume forces,  $n$  the outer normal,  $\bar{t}$  the superficial forces,  $u_{imp}$  the imposed displacements. Finally, considering an infinitesimal deformation  $\delta v$ , the weak formulation is,

$$\int_{\Omega} \sigma \nabla \delta v = \int_{\Lambda_t} t \delta v d\Gamma + \int_{\Lambda} f \delta v d\Omega
 \tag{3.31}$$

### 3.9.2 Constitutive Relations

Although the fact the weak formulation has always the same form, the element quality depends on the constitutive relations, as well of the selected shape forms.

This thesis is limited to the linear elastic fracture mechanics, implying that only small strains will be considered. The material model could not be different than the presented next, which is a limitation imposed by the commercial software of analysis Abaqus®.

Respecting the elasticity theory, the tension obeys to the following,

$$\begin{bmatrix} \sigma_{xx} \\ \sigma_{yy} \\ \sigma_{zz} \\ \sigma_{xy} \\ \sigma_{xz} \\ \sigma_{yz} \end{bmatrix} = D \begin{bmatrix} \epsilon_{xx} \\ \epsilon_{yy} \\ \epsilon_{zz} \\ 2\epsilon_{xy} \\ 2\epsilon_{xz} \\ 2\epsilon_{yz} \end{bmatrix} \quad (3.32)$$

Being D given by,

$$D = \frac{E(1-\nu)}{(1+\nu)(1-\nu)} \begin{bmatrix} 1 & \frac{\nu}{1-\nu} & \frac{\nu}{1-\nu} & 0 & 0 & 0 \\ \frac{\nu}{1-\nu} & 1 & \frac{\nu}{1-\nu} & 0 & 0 & 0 \\ \frac{\nu}{1-\nu} & \frac{\nu}{1-\nu} & 1 & 0 & 0 & 0 \\ 0 & 0 & 0 & \frac{1-2\nu}{2(1-\nu)} & 0 & 0 \\ 0 & 0 & 0 & 0 & \frac{1-2\nu}{2(1-\nu)} & 0 \\ 0 & 0 & 0 & 0 & 0 & \frac{1-2\nu}{2(1-\nu)} \end{bmatrix} \quad (3.33)$$

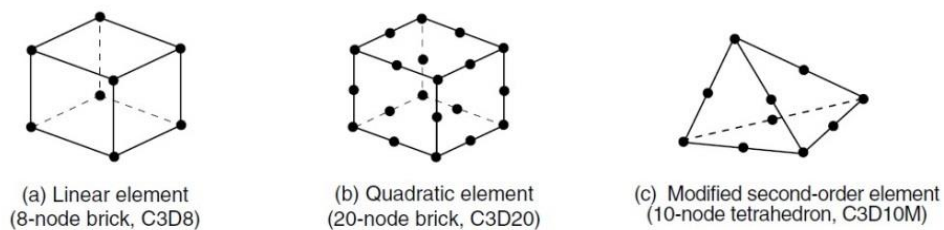
Where  $\sigma_{ij}$  and  $\epsilon_{ij}$  are the tension and strain components, E the Young's modulus, and  $\nu$  the Poisson coefficient.

### 3.9.3 Element Types

In Abaqus® , the geometries under analysis can be modelled with two types of volumetric elements: the tetrahedral and hexahedral, which remains the isoparametric element most used for three-dimensional elasticity.

Abaqus® admits two formulations of this element. The linear element of 8 nodes, identified as C3D8, and the quadratic of 20 nodes, C3D20 (Figure 3.9 a and b).

At each node, for both elements, there are three degrees of freedom, corresponding to three possible displacements. Thus, the element of 8 nodes, has 24 degrees of freedom, a number three times lower than the 60 degrees of freedom of the element of 20 nodes [35].



**Figure 3.9: Three dimensional elements,  
(a) 8 nodes, (b) 20 nodes, (c) 10 nodes, from [35]**

As for the tetrahedral, there is a linear element of 4 nodes, C3D4 and a quadratic element with 10 nodes, the C3D10 (Figure 3.9 c).

Any of the four elements allows two kinds of numerical integration; reduced or full integration. The reduced integration is identified by a R in the element code. For example, C3D20R, indicates a three-dimensional element of 20 nodes, being a quadratic with reduced integration.

### 3.10 The Classical Approach to the Stress Intensity Factor Calculation

In order to have a full understanding of the LEFM, it is necessary to evaluate the geometries with the classical approach for the stress intensity factor calculation.

In the classical approach, according to [28], in two-dimensional problems quadrilateral elements are collapsed to triangles where three nodes occupy the same point in space, like what is shown on Figure 3.10. For three dimensions problems, a brick element is degenerated to a wedge (Figure 3.11).

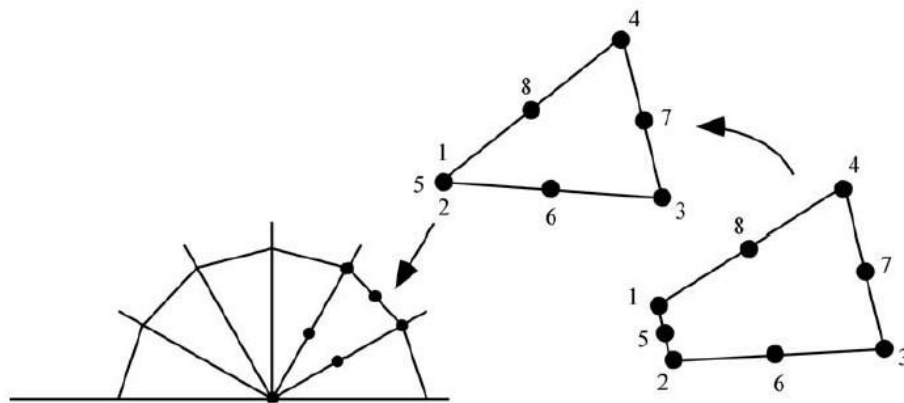


Figure 3.10: Degeneration of a quadrilateral element into a triangle at the crack tip [28]

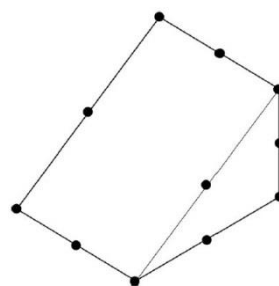
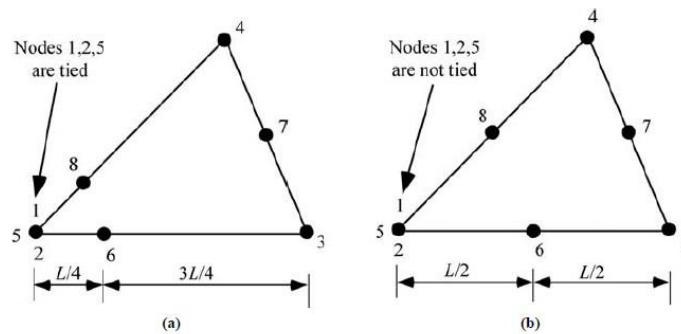


Figure 3.11: Degeneration of a brick element into a wedge [28]

In elastic problems, the nodes at the crack tip are normally tied, and the mid-side nodes moved to the 1/4 points. This modification is necessary to introduce a  $1/\sqrt{r}$  strain singularity in the element, which brings numerical accuracy due to the fact that the analytical solution contains the same term.

A similar result can be achieved by moving the midside nodes to 1/4 points in non collapsed quadri-lateral elements, but the singularity would exist only on the element edges; collapsed elements are preferable in this case because the singularity exists within the element as well as on the edges.

When a plastic zone forms, the singularity no longer exists at the crack tip. Consequently, elastic singular elements are not appropriate for elastic-plastic analyses. Figure 3.12 shows an element that exhibits the desired strain singularity under fully plastic conditions

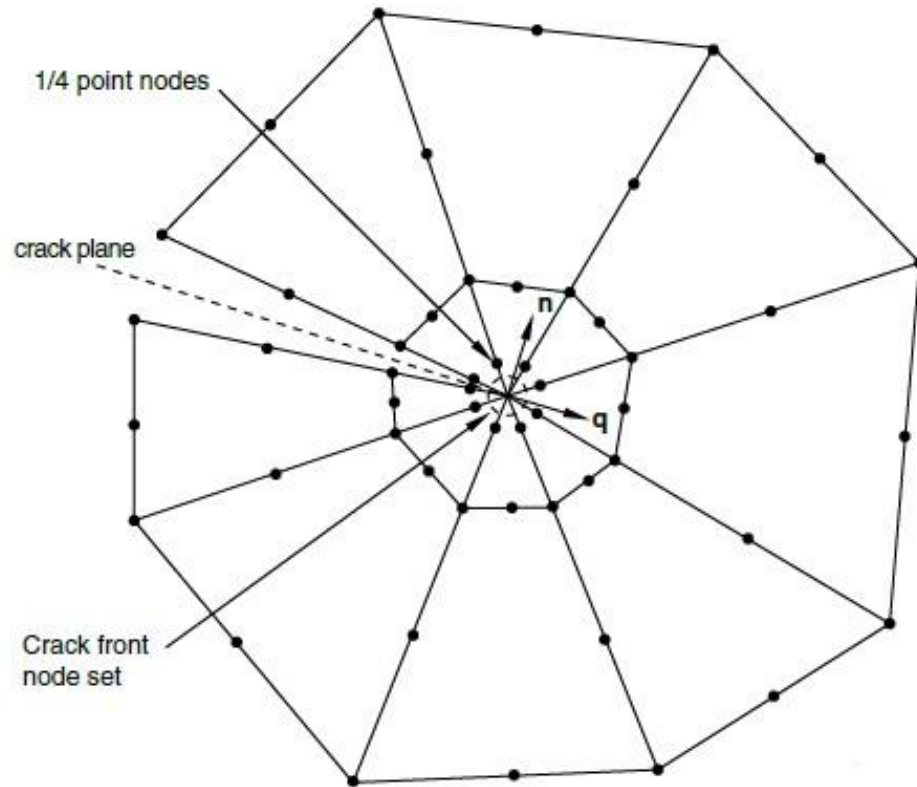


**Figure 3.12: Crack-tip elements for elastic and elastic-plastic analyses.**

**Element (a) produces a  $1/\sqrt{r}$  strain singularity, while (b) exhibits a  $1/r$  strain singularity (a) Elastic singularity element and (b) plastic singularity element [28]**



According to [28], [35] for typical problems, the most efficient mesh design for the crack-tip region is the “spider-web” configuration (Figure 3.13), consisting of concentric rings of quadrilateral elements that are focused

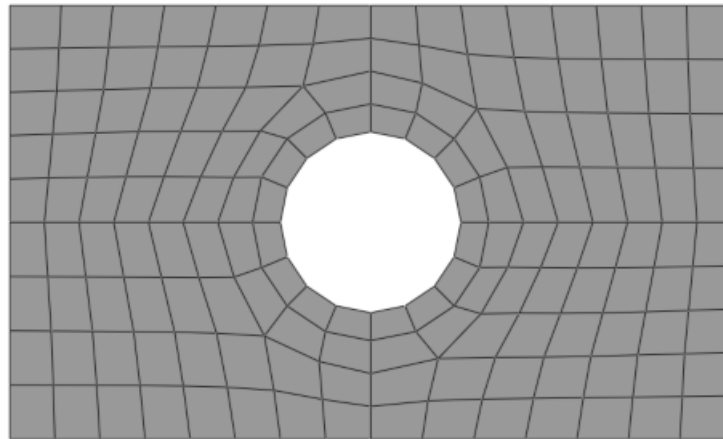


**Figure 3.13: Spider-web mesh from [35]**

toward the crack tip. The elements in the first ring are degenerated to triangles, as described above. Since the crack tip region contains stress and strain gradients, the mesh refinement should be greater at the crack-tip. The spider-web design allows a smooth transition from a fine mesh at the tip to a coarser. In addition, this configuration results in a series of smooth, concentric integration domains (contours) for the J-Integral calculation.

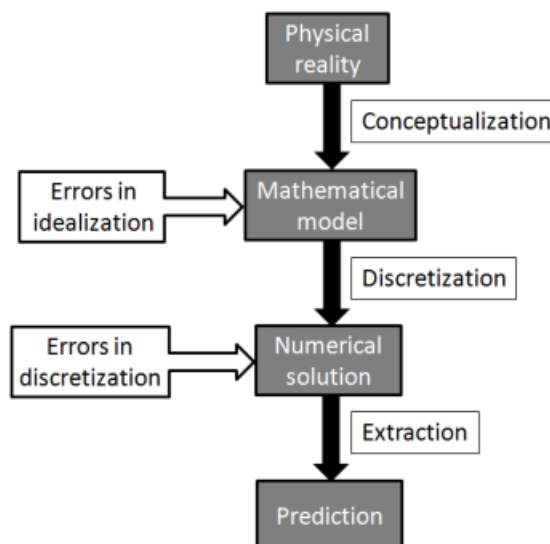
### 3.11 Finite element analysis techniques

Finite element analysis (FEA) is one of the most powerful and pervasive numerical methods used in modern engineering practice. A central principle of FEA is subdividing the solution domain into smaller, geometrically simple pieces which are called elements, in a process called discretization. An example discretization, or mesh, of a plate with a hole in it is shown in Figure 3.14



**Figure 3.14: Example of discretization**

The finite element method is an approximation of an exact answer and therefore has some amount of error. These errors can come from errors in idealization or discretization, as depicted in Figure 3.15.



**Figure 3.15: Numerical simulation process.**

### **3.11.1 Available tools and softwares**

In the FEM, the structure is subdivided into discrete elements. Different Element types can be used to cover the problem. Elements are connected at node, where continuity of displacement field is imposed. Displacements at nodes depend on the element stiffness. In the FEM, the structure is subdivided into discrete elements. Different Element types can be used to cover the problem. Elements are connected at node, where continuity of displacement field is imposed. Displacements at nodes depend on the element stiffness and computational of the nodal forces. For structural problems, numerical solution consists of computing nodal displacements. Stress and strain distributions throughout the body, as well as the crack parameters such as SIF, can be inferred from the nodal displacements. A number of commercial FEM packages have the ability of crack modelling and performing the fracture mechanics calculations. There is also some non-commercial code, as the FRANC2D, which is developed by the Cornell University, being surprisingly easy to learn and offering many capabilities. Finite element analysis can be carried out by several available software like ABAQUS, ANSYS, and LS- DYNA etc. These software are user friendly and give a wide range of analysis options. Static, dynamic, fluid, thermal and electromechanical problems can be analysed by means of those codes.

In this thesis, the ABAQUS© was used, it can solve linear and nonlinear problems. It was designed to be able to investigate many links of nonlinearities such as geometrical material or multi-physic domains. Some specialized modules allow investigation of several behaviour of material in presence of plasticity, buckling, electromechanical coupling and even fracture. Numerical tools are evaluated to solve nonlinear problems by an automatic updating of the set-up to assure the numerical convergence and an accurate result.

### **3.12 Conclusion**

In the preceding sections of the report, the reader has been introduced with the theory and basics of LEFM, alongwith the different approaches that have been developed over the years by qualitatively and quantitatively assess the phenomenon of fracture. The utility of the stress intensity factor as a single parameter for prediction of crack behaviour is the most important aspects of LEFM. The soundness of the theory can be gauged with the similarity in results obtained by various researchers like Griffith and Irwin. The different design approaches suggested by the LEFM method are now being applied in harmony with classical design and LEFM has in-fact taken over classical design methodologies in areas like pressure vessels, nuclear containment chambers, boiler vessel design, explosive weaponry design and other areas that require explicit results rather than mere theoretical or limit load analysis.

## **CHAPTER 4**

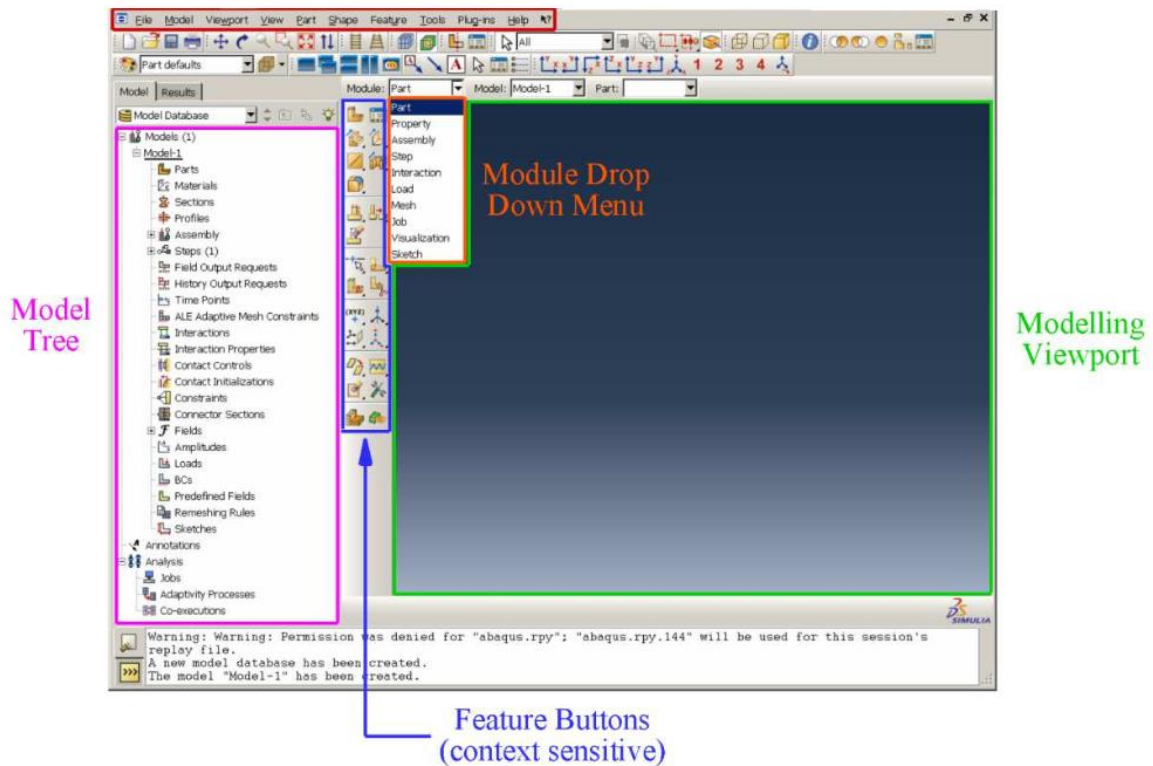
### **SIF AND J-INTEGRAL DETERMINATION USING ABAQUS®**

#### **4.1 Using Abaqus/CAE (v6.14)**

Figure 4.1 shows the graphical user interface of Abaqus/CAE version 6.14 upon initial start up of the software. Abaqus has a number of ways in which modelling and presentational tools can be utilised and these are explained in more detail in the Abaqus User's Manuals (Abaqus 2014a). As with the majority of Windows programs, across the top of the window is the tool bar. In Abaqus, this is content sensitive and the options presented change depending on the current task that the user is trying to achieve. This is dependent on which module is currently selected. The modules are listed in the drop-down menu in Figure 4.1, as well as in Table 4.1, which details the function and key features of each module. When a different module from this drop-down menu is selected, the options available on the tool bar change. However, most of the basic modelling options can be achieved by using the buttons directly alongside the modelling viewport. At the left of the screen is the model tree. This can be navigated by expanding the available options and clicking the relevant title to access the appropriate modelling tool menus.

Table 4.1 lists the modules available in Abaqus/CAE v6.10 and explains their basic functions and key features. There are significantly more tools and settings available within the program, and those used within the work of this thesis are detailed when their use is discussed.

### Tool Bar (context sensitive)



**Figure 4.1: Graphical user interface of Abaqus/CAE v6.14 upon start up.**

**Table 4.1: Outline of Abaqus/CAE v6.14 modules.**

Module	Description	KeyFeatures	
Part	Used to define geometry of parts. Simple CAD functions are available, but files can be imported from more advanced CAD packages such as SolidWorks.	Create Part	Create deformable and rigid 2D and 3D parts.
		Regenerate Features	If changes are made to a part, assembly, etc, the features must be regenerated for the changes to take effect.
		Create Partition	Split created parts into regions which can make applying properties, loads, boundary conditions simpler, and give more control over meshing.

Property	Used to create materials and sections, and apply them to created parts.	Create Material	Define material properties.
		Create Section	Define cross sectional properties.
		Assign Section	Each part or region must have a section assigned to it.
Assembly	Insert parts into an assembly as “instances”, which can then be manipulated individually.	Instance Part	Insert instances of created parts into the assembly.
		Translate/Rotate Instance	Position each instance as required within the assembly.
Step	Steps are essentially intermediate points within the simulation where parameters can be altered.	Create Step	Create intermediate steps within the simulation and define the way each one will be solved.
		Create FieldOutput	Choose which outputs are required in each step of the simulation.
Interaction	Define interactions between parts in the assembly, such as contact interactions.	Create Interaction	Select potentially interacting surfaces and define how the simulation will treat them.
		Create Interaction Property	Define the details of the interactions of part surfaces.
		Contact Controls	Advanced contact settings.
Load	Used to create loads and boundary conditions.	Create Load	Define type of loading and application region.
		Create Boundary Condition	Define type of boundary condition and application region.
Mesh	Create finite element meshes on parts.	Seed Part Instance	Sets a global mesh seed that is applied to all edges on the selected part.
		Seed Edge	Define a mesh seed on a selected edge.
		Mesh Part Instance/Region	Create mesh based on currently applied mesh seeds.
		Assign Mesh Controls	Select element shape and meshing technique for selected part or region.

Mesh (continued)	Create finite element meshes on parts.	Assign Element Type	Choose type of elements to be used in selected part or region.
		Verify Mesh	Assess mesh quality based on element shape and size. Check for potential analysis
Job	Create jobs for submission, write input files and monitor running	Create Job	Create jobs for analysis.
		Monitor	Check progress of currently running job.
Visualization	Show requested field outputs after (or during) a simulation.	Plot Contours on Deformed Shape	Quickest and simplest way of viewing results of a simulation.
Sketch	Similar to the part module, but just the CAD drawing tool.	Create Sketch	Opens the CAD drawing tool, without subsequently creating a part. Sketches can be opened in the Part module.



## 4.2 Finite Elements in Fracture Mechanics

In linear elastic fracture mechanics (LEFM) the stress field ahead of the crack-tip in a body with an arbitrary crack varies in a  $1/\sqrt{r}$  distribution. The stress intensity factors (SIF) in LEFM provide a measure of the magnitude of the singularity of the singular stresses at the crack-tip associated with various modes of deformation. Researchers have presented analytical solutions for the three basic modes of loading for varying crack sizes and relatively simple-shaped domains. An extensive collection of such work can be found in various handbooks such as Murakami (1987, 1992), Sih (1973), Tada et. al. (1973) [29] and Rooke and Cartwright (1976). However for realistic complex shapes that are usually encountered in practice, more general techniques are required. The very versatile finite element method enables such computation.

The direct application of finite element method in treatment of cracks using conventional element converges very slowly due to lack of singularity representation. It is necessary to develop an extremely fine grid near the crack-tip in order to represent the form of singularity and accurate extraction of SIF's. This led to the development of numerous singular elements, which incorporate the necessary  $1/\sqrt{r}$  stress singularity either explicitly or implicitly in the formulation, where  $r$  is radial distance from the crack tip to a point in the singular element. Amongst these elements, the quarter point element (QPE) is the popular and widely used. Virtually all commercial finite element packages have incorporated these elements for analysis of fracture mechanics problem.

Large numbers of techniques are available for numerical determination of SIF's. Of the various methods widely used, the following deserve mention:

- 1 The displacement correlation technique (Shih et al., 1976)
- 2 Quarter point displacement technique (Shih et al., 1976)
- 3 Virtual crack extension method (Parks, 1974)
- 4 J-integral (Ishikawa et al., 1979), (ABAQUS ver.6.7.1, 2007)
- 5 Displacement extrapolation technique (ANSYS, 2005)
- 6 Modified crack closure integral method (Rybicki and Kannien, 1977)

### 4.3 SIF Extraction for a 2D centre cracked plate of Finite Dimensions

#### Problem Description:

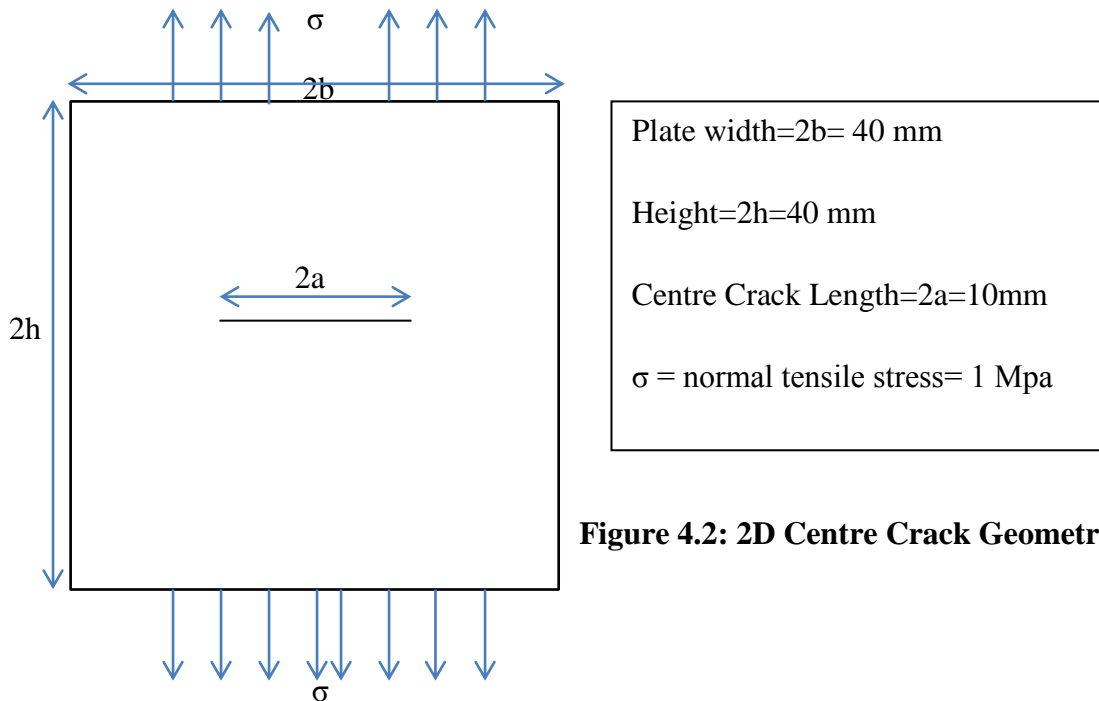




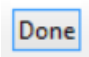
Figure 4.2: 2D Centre Crack Geometry


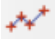

#### 4.3.1 Procedure used in Abaqus

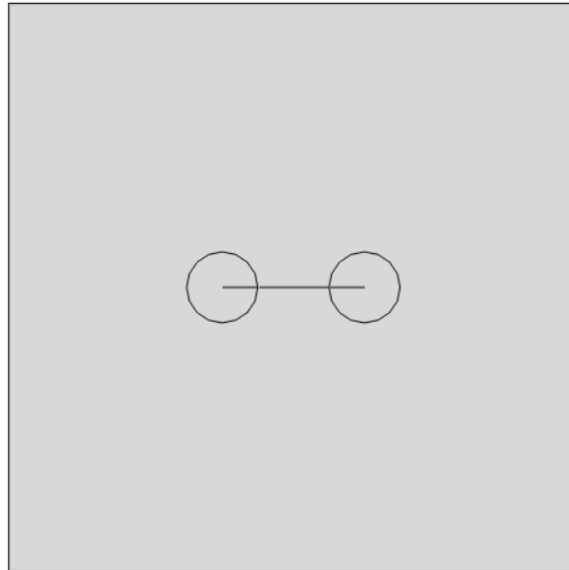
##### I. Creating a part

First create “**Part**” which defines the geometry of the individual components of model and, therefore, the building blocks of an ABAQUS/CAE model. We will start the Center Crack problem by creating a two-dimensional, deformable shell part.

Click **Part** menu>create...>select *2D Planer* in modeling space, *Deformable* type, *shell* feature

Select **Create Lines (Rectangle)**  and draw a rectangle. Then click **Add dimension**  and give length and breadth of 40 mm and then click .

Then click **Partition Face:Sketch**  and create Line  of 10 mm in center and two circles  of 5 mm diameter at the both end of line. Then our final geometry looks like below-



This is a square shape part of 40 mm size and crack is at center of 10 mm length with normal tensile stress of 1 Mpa.


## II. Creating the material properties

Now define “**Property**” of the part. In this problem the part is made of steel and assumed to be linear elastic with Young’s modulus (E) of 210 GPa and Poisson’s ratio ( $\nu$ ) of 0.33. Thus, we will create a single linear elastic material with these properties.

Young's Modulus	Poisson's Ratio
210000	0.33

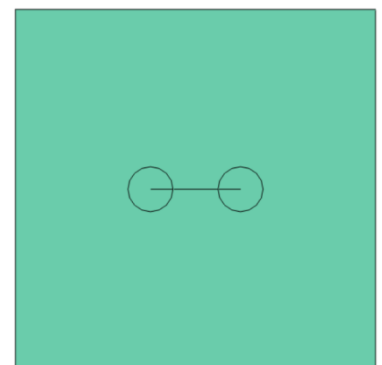
**Property module**>Click **Create Material** 

>create...>Mechanical>Elasticity>Elastic>*Isotropic* type,  
E=210 Gpa,  $\nu=0.33$

Then **Section** menu>create...  >*Solid* category,  
*Homogenous* type

**Section** menu>Assignment Manager... 


>create...>select whole part to assign the property to that part



After Section assignment color of part will change into **Green**.

### III. Defining the assembly

Now go to “**Assembly**” module. Each part that we create is oriented in its own coordinate system and is independent of the other parts in the model. Although a model may contain many parts, it contains only one assembly. We define the geometry of the assembly by creating instances of a part and then positioning the instances relative to each other in a global coordinate system. An instance may be independent or dependent. Independent part instances are meshed individually, while the mesh of a dependent part instance is associated with the mesh of the original part.

**Assembly** module>**Instance** menu  >create...>select *Part* and select *Instance type Independent* (mesh on instance)


### IV. Configuring the analysis

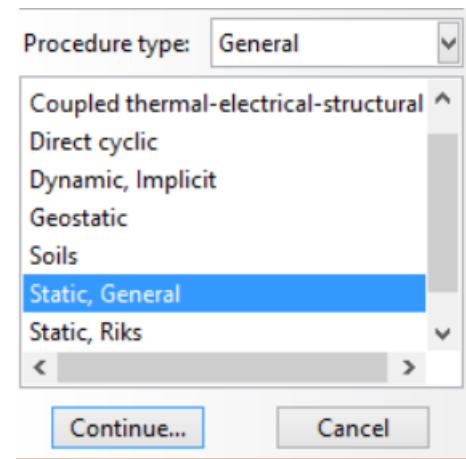
Now create “**Step**”. This is a single event, so only a single analysis step is needed for the simulation. Thus, the analysis will consist of two steps overall:

- An initial step, in which we will apply boundary conditions that constrain the ends of the frame.
- An analysis step, in which we will apply a concentrated load at the center of the frame.

ABAQUS/CAE generates the initial step automatically, but we must create the analysis step. We may also request output for any steps in the analysis.

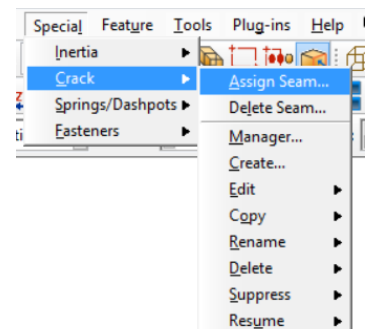
There are two kinds of analysis steps in ABAQUS: **general analysis steps**, which can be used to analyze linear or nonlinear response, and **linear perturbation steps**, which can be used only to analyze linear problems.

**Step** module>step menu>create...  >select *Procedure type* as *General* and click *Static, General*>continue...>Nlgeom off>click OK



### V. Defining the Crack

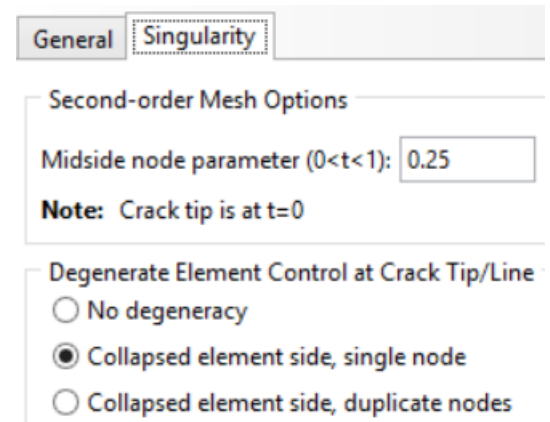
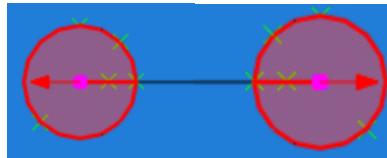
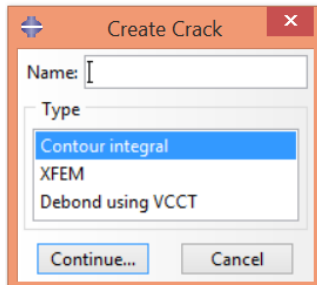
Now go to “**Interaction**” module. In this module we will define Crack. So first define **seam**.



Click **Special** menu>Crack>Assign seam...>select seam region.

(The center line is our seam region.)

Click Special menu>Crack>create...>**Contour Integral type**>then select *Crack Front*,  
*Crack tip*, and *q-vector*.




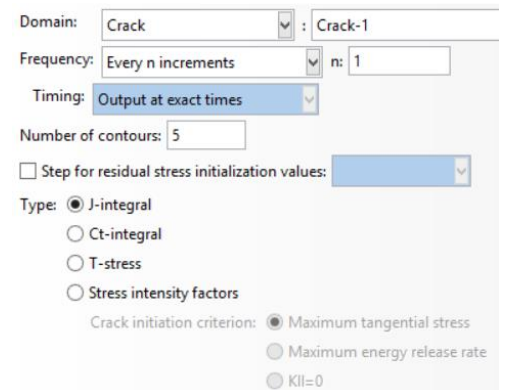
Since our part is linear elastic hence choose *strain singularity* and put *Midside node parameter* value as .25 and choose *Collapsed element side, single node*.

## VI. Defining the History Output

After creating crack always assign History Output Requests from step module.

**Step** module>**Output** menu> **History Output**

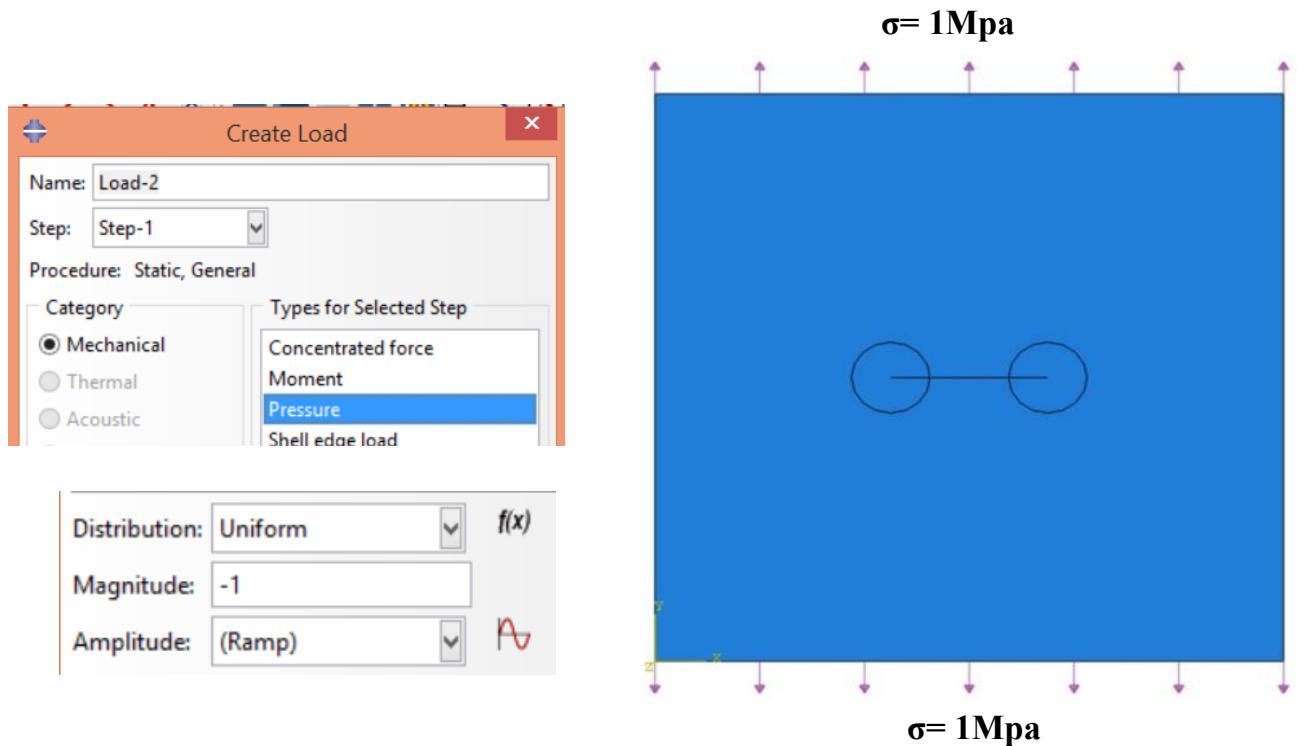
**Requests**>create... >continue...>select **Crack** in *Domain*>*Number of Contours: 5*>select **J-integral**




Do same to select **Stress Intensity Factors** and create another History Output Request.

## VII. Applying Boundary Conditions and Loads to the model



Prescribed conditions, such as loads and boundary conditions, are step dependent, which means that we must specify the step or steps in which they become active. Now that we have defined the steps in the analysis, we can define prescribed conditions.

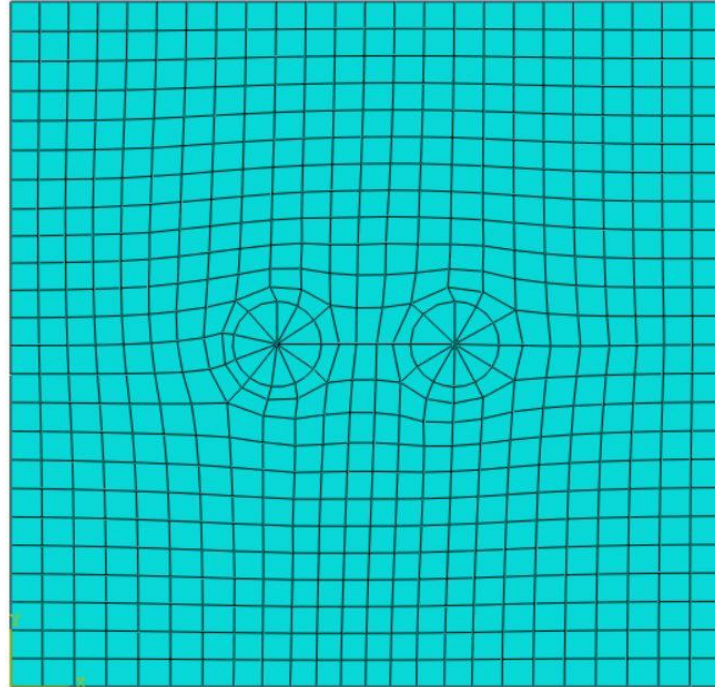


**Load** module>**Load** menu>create...  >select step, **Mechanical** category, **Pressure**>now select surface for load (top and bottom)>*Uniform* Distribution, *Magnitude* -1 Mpa (because of tensile in nature) .

## VIII. Meshing the model

We will now generate the finite element mesh. We can choose the meshing technique that ABAQUS/CAE will use to create the mesh, the element shape, and the element type. The default meshing technique assigned to the model is indicated by the color of the model that is displayed when we enter the Mesh module.

**Mesh** module>**mesh** menu>**controls...**  >select *crack front region*>select **Tri** element now select *rest part* and choose **Quad** element and Free, ***Medial Axis Algorithm***.  
Mesh menu>**instance...**  >ok to mesh the part instance.



**Total no. of Nodes= 1915**

**Total no. of elements= 609**

**Figure 4.3: 2D centre crack plate mesh**

## IX. Creating Input file and Run the Job

```
** MATERIALS

*Material, name=Material-1

*Elastic

210000., 0.33

** STEP: Step-1

*Step, name=Step-1, nlgeom=NO

*Static
```

Name	Model	Type	Status	Write Input
Job-1	pressure	Full Analysis	Completed	Data Check

Job module>create...>*Write Input*

then **submit** the job and analyze the job.

## X. RESULTS :

In the visualization module, we can get the deform part and different output like stress, strain, displacement, translation which we have set in the field outputs. Also

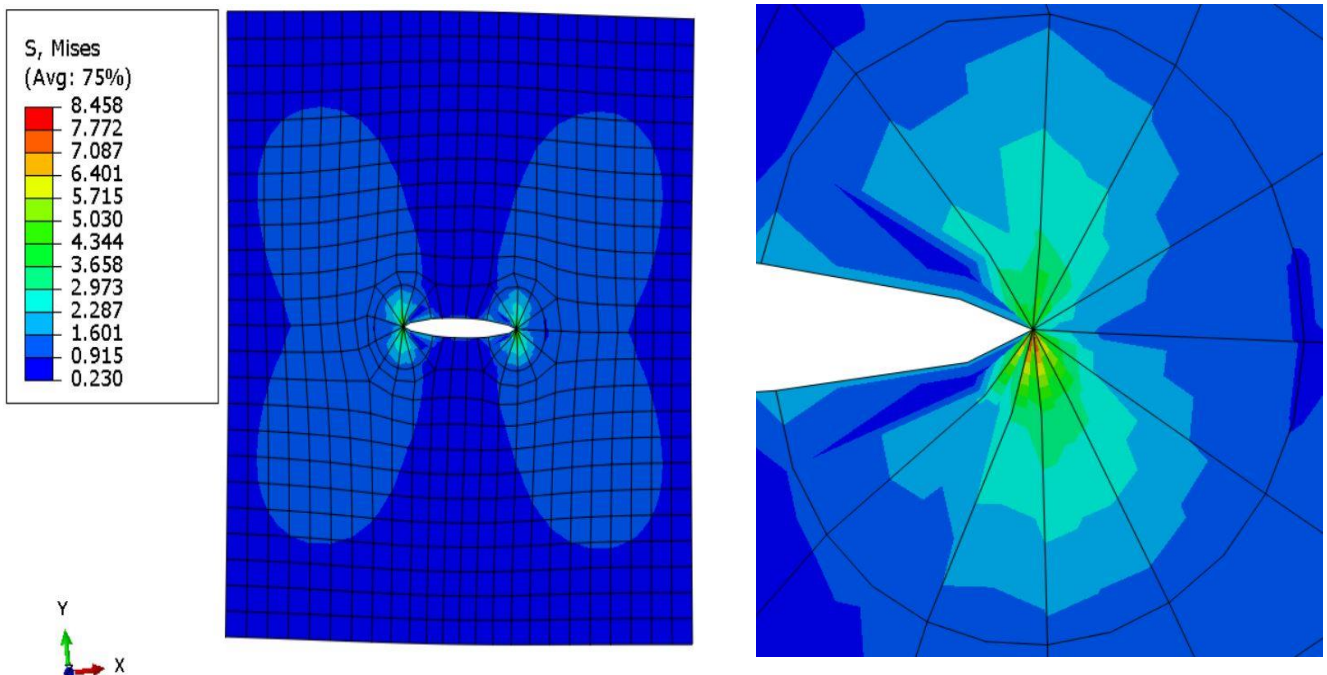



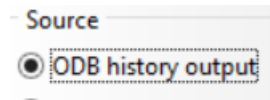
Figure 4.4: 2D centre crack plate von-mises stress contour



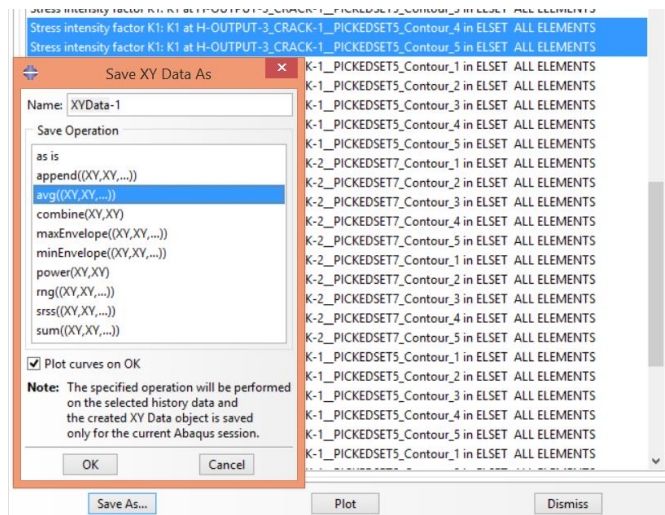
we can get results for crack like J-Integral, stress intensity factor which are set in History outputs.

Above are the different contours of deformed part.

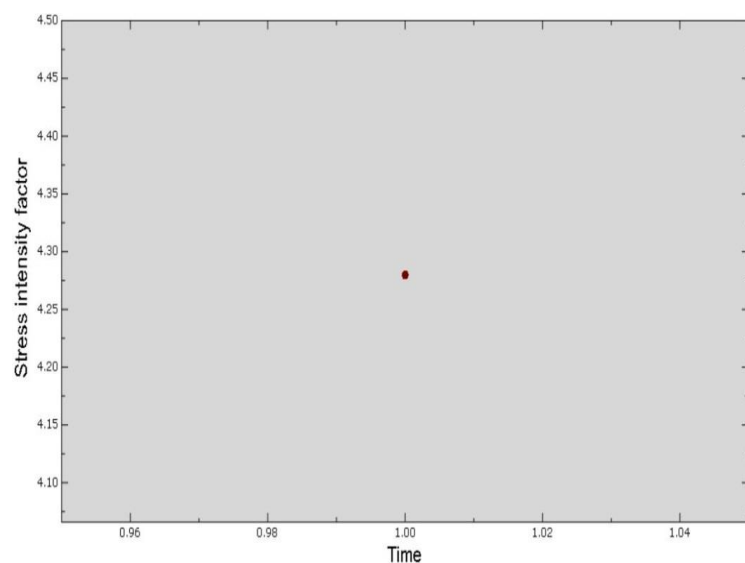
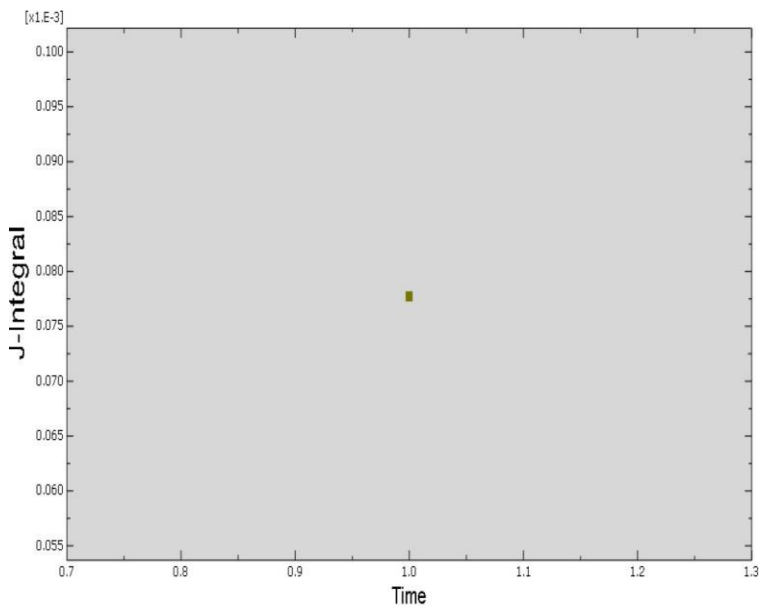
To get Stress Intensity factor, First click create xy data  then odb history output



Now we can find Stress intensity factor or we can filter name by type \*K1\*. Then we should select higher contour values and get average of it.



Similarly we can do for J-integral.



### 4.3.2 Analytical solution

Since stress intensity factor  $K_I = \sigma \sqrt{\pi a} \cdot F\left(\frac{a}{b}\right)$

Here “F(a/b)” is a factor, which depends on geometry and location of crack. Empirical formula given for F(a/b) for center crack by Tada, Paris and Irwin in Handbook [8]

$$F\left(\frac{a}{b}\right) = \frac{1 + \frac{a}{2b} + .326 * \left(\frac{a}{2b}\right)^2}{\sqrt{1 + \frac{a}{2b}}}$$

here  $\sigma = 1$  MPa       $a = 5$  mm       $b = 20$  mm

After solving we get  $F(a/b) = 1.0798699$

Hence stress intensity factor  $K_I = 1 * \sqrt{\pi * 5} * 1.0798699 = 4.279877 \text{ MPa}\sqrt{\text{mm}}$

Since J-Integral (J) =  $\frac{K^2 * (1 - \nu^2)}{E}$

$$\text{So } J = \frac{4.279877^2 * (1 - .33^2)}{210000} = 7.77266 * 10^{-5} \text{ N/mm}$$

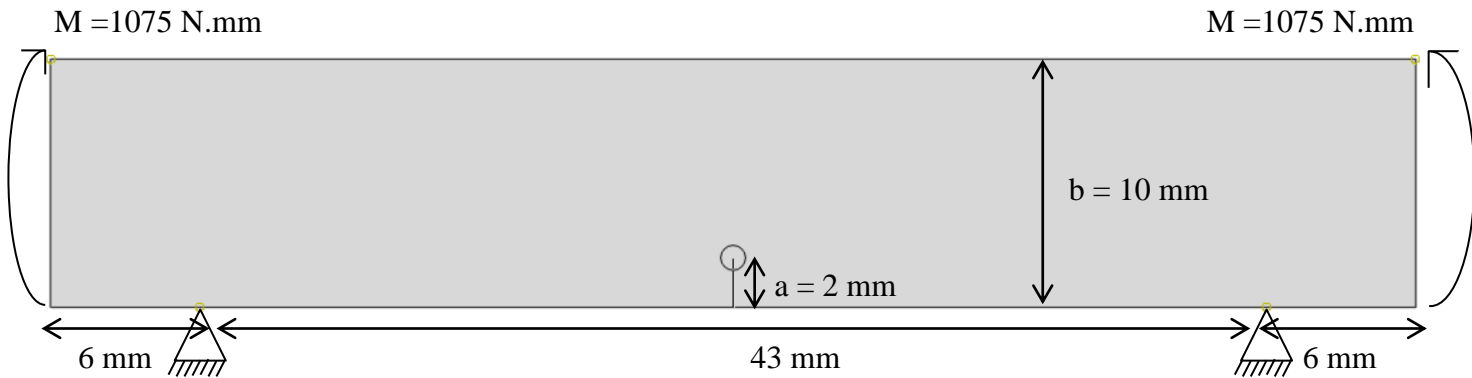
### 4.3.3 Comparison results of Abaqus with Analytical Solution

**Table 4.2: Comparison of results of 2D Centre Crack**

	Abaqus Results	Analytical Results	Error %
Stress Intensity Factor (K) $\text{MPa}\sqrt{\text{mm}}$	4.27985	4.279877	<b>.0006 %</b>
J-Integral (J) $\text{N/mm}$	$7.77258 * 10^{-5}$	$7.77266 * 10^{-5}$	<b>.001%</b>

## 4.4 SIF Extraction for Crack in a Three Point Bend Specimen (Moment applied)

### 4.4.1 Problem Description and Abaqus Procedure

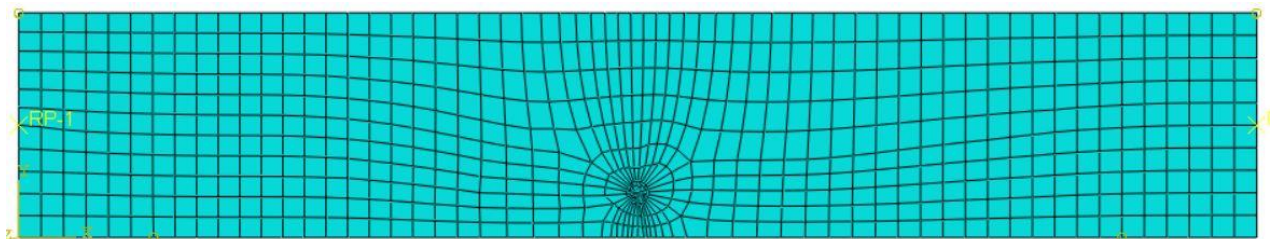


**Figure 4.5: Three Point Bend Specimen (Moment applied)**

In this problem, the crack length  $a$  is 2 mm and specimen width is 10 mm. Length of specimen is 55 mm. Bending Moment applied at the end is 1075 N.mm. Linear Elastic Material properties given are  $E = 200$  GPa, and  $\nu = .3$ , young modulus and poisson ratio respectively.

In abaqus for moment applied, given at a node. Hence we have to constraint the both end surface node to a single node. For this Kinematic Coupling is used in Interaction Module.

Since at crack tip focused mesh is necessary, hence at crack tip a circle of radius 0.5 mm is drawn which facilitates swept meshing also.



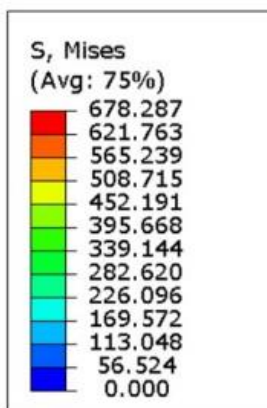
**Figure 4.6: Three Point Bend Specimen mesh**

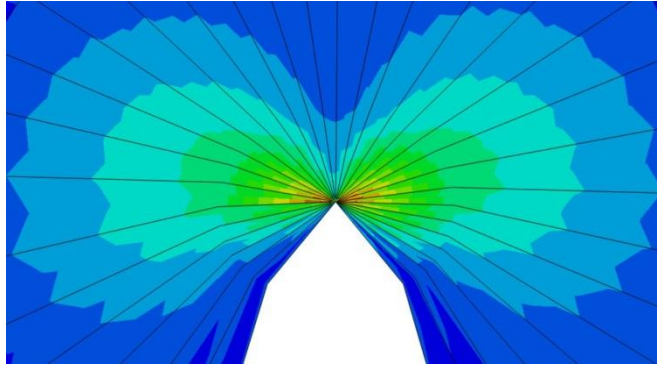
CPE4R ELEMENTS, of quadratic reduced integration plain strain elements are used.

## Results

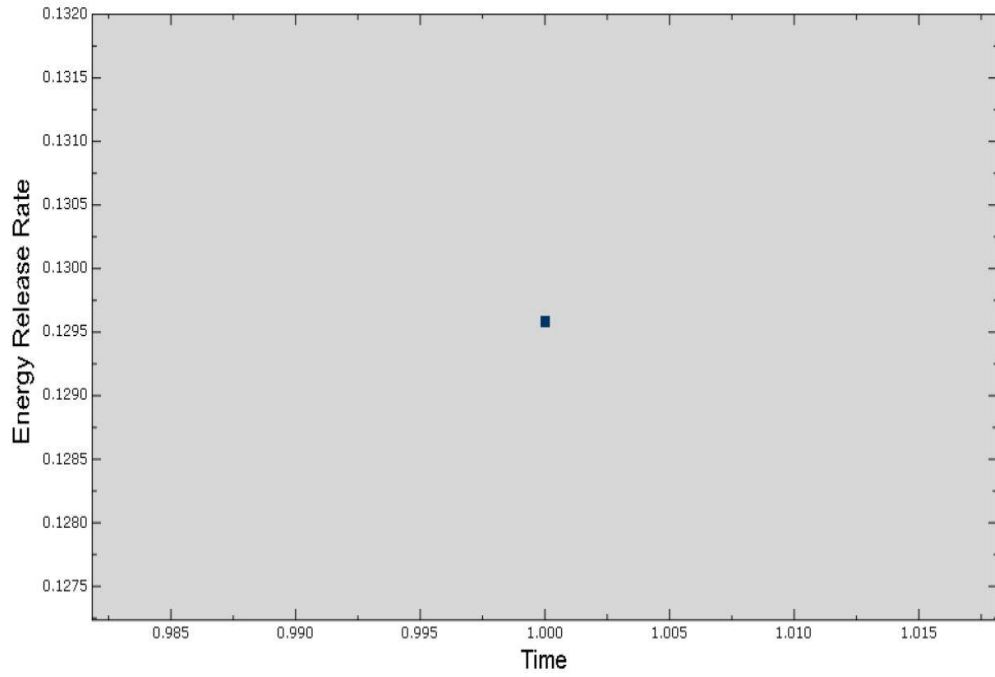
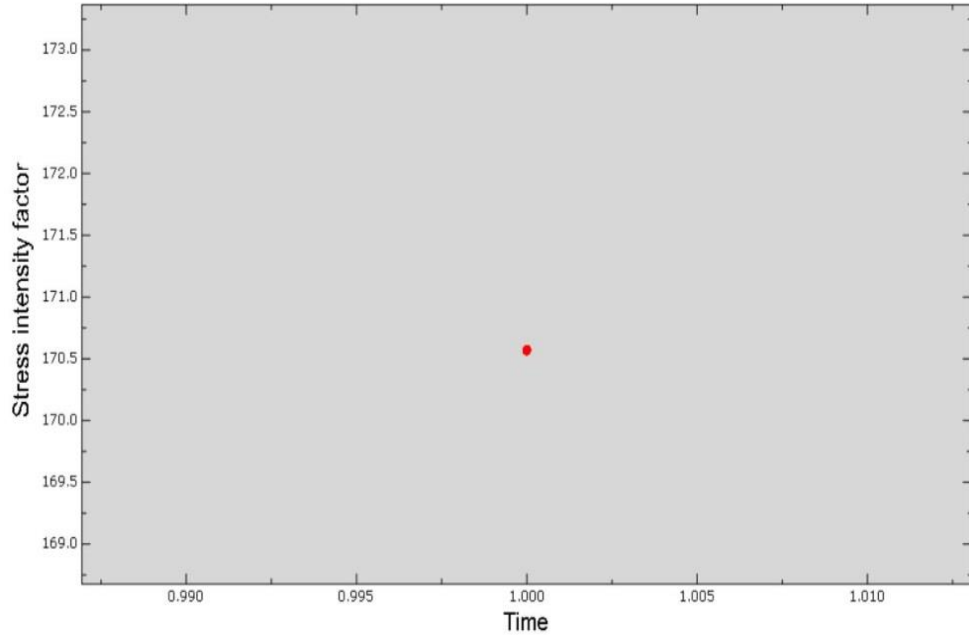
### INPUT FILE CODES

```
*Element, type=CPE8R
*Material, name=Material-1
*Elastic
200000., 0.33
** STEP: Step-1
*Step, name=Step-1, nlgeom=NO
*Static
1., 1., 1e-05, 1.
** BOUNDARY CONDITIONS
** Name: BC-1 Type: Displacement/Rotation
*Boundary
_PickedSet59, 1, 1
_PickedSet59, 2, 2
** LOADS
** Name: Load-1 Type: Moment
*Load
_PickedSet57, 6, -1075.
** Name: Load-2 Type: Moment
*Load
_PickedSet58, 6, 1075.
** HISTORY OUTPUT: H-Output-4
*Contour Integral, crack name=H-Output-4_Crack-1, contours=5, crack tip nodes,
type=K FACTORS
_PickedSet5, _PickedSet6, 0., 1., 0.
```





**Figure 4.7: Three Point Bend Specimen von-mises stress contour**



#### 4.4.2 Analytical solution

Since stress intensity factor  $K_I = \sigma \sqrt{\pi a} \cdot F\left(\frac{a}{b}\right)$

Here “F(a/b)” is a factor, which depends on geometry and location of crack. Empirical formula given for F(a/b) for center crack by Tada, Paris and Irwin in Handbook [8]

$$\text{Since } \sigma = \frac{6M}{b^2} = \frac{6 \cdot 1075}{10 \cdot 10} = 64.5 \text{ MPa}$$

$$\text{And } F\left(\frac{a}{b}\right) = 1.122 - 1.40 \cdot \frac{a}{b} + 7.33 \cdot \left(\frac{a}{b}\right)^2 - 13.08 \cdot \left(\frac{a}{b}\right)^3 + 14 \cdot \left(\frac{a}{b}\right)^4$$

After solving, F(a/b) = 1.05296

$$\text{Hence } K_I = 64.5 \cdot \sqrt{\pi \cdot 2} \cdot 1.05296$$

$$\mathbf{K_I = 170.24 \text{ MPa}\sqrt{\text{mm}}}$$

$$\text{Since J-Integral (J) = } \frac{K^2 \cdot (1 - \nu^2)}{E}$$

Hence we get, J = **0.1291277** N/mm

#### 4.4.3 Comparison results of Abaqus with Analytical Solution

**Table 4.3: Comparison of results for Three point Bend Specimen**

	Abaqus Results	Analytical Results	Error %
Stress Intensity Factor (K) $\text{MPa}\sqrt{\text{mm}}$	170.571	170.24	<b>.19445%</b>
J-Integral (J) $\text{N/mm}$	.129587	.1291277	<b>.3557%</b>

## 4.5 SIF Extraction for a 3D centre through cracked plate of Finite Dimensions

As shown in Figure 4.8, which is symmetrically cut in yz plane from full part, a finite plate with a centre through crack is loaded in tension.

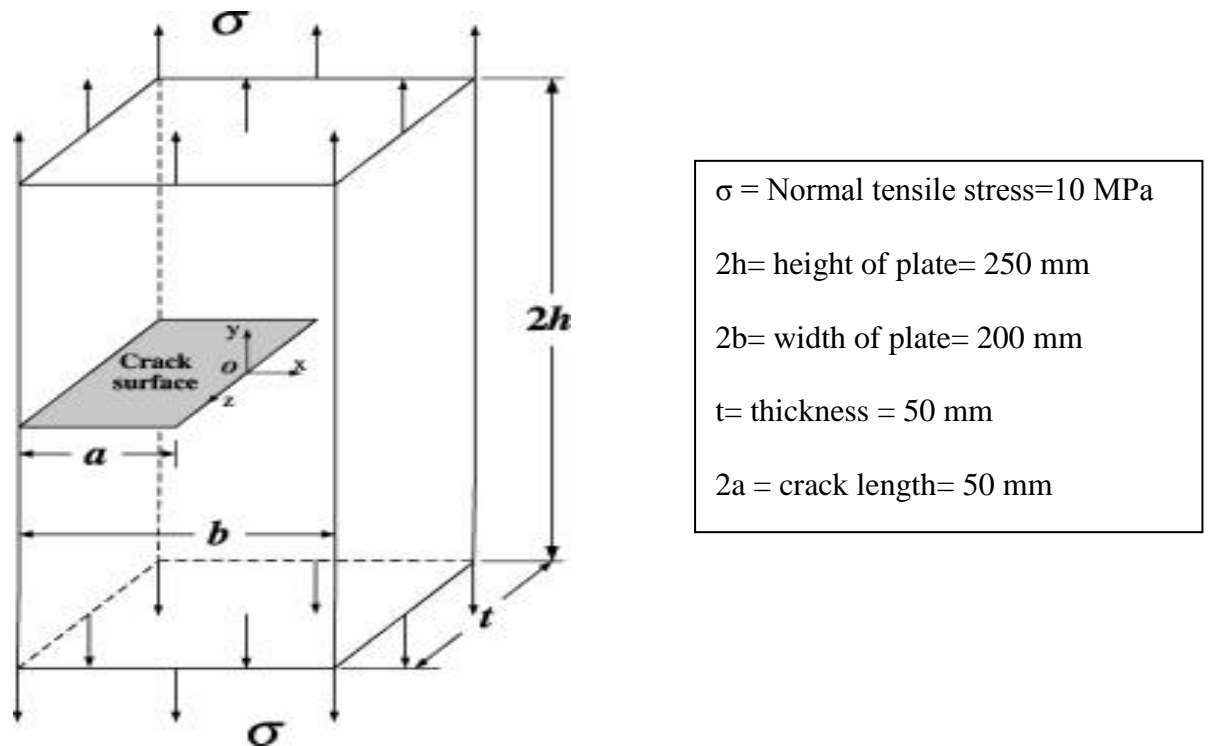


Figure 4.8: 3D centre through cracked plate(half part)

It is proposed to determine the SIF of the crack using ABAQUS ver 614 a simple instance like the above was chosen to validate and compare the results obtained by finite element simulation with published analytical solutions.

For material definition, SS-304 was chosen, having  $E = 193$  GPa,  $\nu = 0.30$ .

ABAQUS provides values of the J-integral; stress intensity factor, and as a function of position along a crack front in three-dimensional geometries. Several contours can be used; and, since the integral should be path independent, the scatter in the values obtained with different contours can be used as an indicator of the quality of the results. The domain integral method used to calculate the contour integral in ABAQUS generally gives accurate results even with rather coarse models, as is shown in this case. The size of the crack-tip singular has been kept at 6.25% of the crack length [8]. The geometry analysed is a semi-elliptic crack in a half-space and is



shown in Figure 4.8. The crack is loaded in mode-I by far-field tension. The mesh is shown in Figure 4.10. 20-node, quadratic brick reduced-integration (C3D20R) elements are used; with the mid side nodes moved to the quarter-point position on those element edges that focus onto the crack tip nodes. This quarter-point method provides a  $1/\sqrt{r}$  strain singularity and thus improves the modelling of the strain field adjacent to the crack tip. The q-vector is used to specify the crack extension direction, as shown in Figure 4.9,[8]. The mesh extends out far enough to cause the boundary conditions on the far faces of the model to have negligible effect on the solution. Taking advantage of symmetry only 1/8th of the plate with half crack length is modelled with symmetry boundary conditions at midplane surface and free outer surfaces. Four rings of elements surrounding the crack tip are used to evaluate the contour integrals, which gives a total of five J-Integral contours, including the contour at the crack tip.


#### 4.5.1 Procedure used in Abaqus

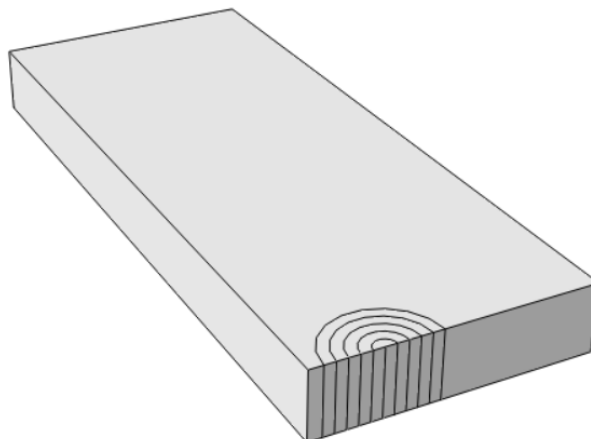
##### I. Creating a Part:

Click **Part** menu>create...>select **3D** in modeling space, **Deformable** type, **solid** shape and type **Extrusion**.

Then first create rectangle of **100 mm x 250 mm** and Blind it of **25 mm**.

Then we have to Partition the face . From the left face create a circle  of center at 25 mm from left face at bottom and radius of 4mm. Similarly draw other 4 circles of 8,12,16,20 mm radius. Also create a partition from the center and through depth.

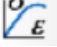
Now we select *partition cell:extend face*  and select the circular face and extend it to depth. Then we have the following part-






## II. Creating the material properties:

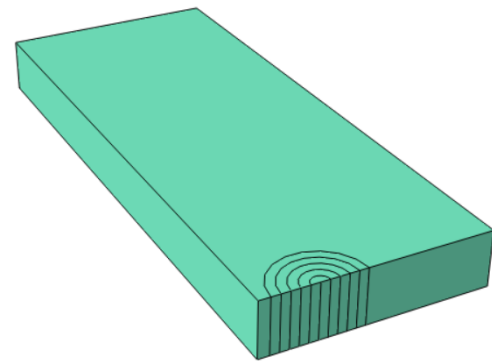
Now define “**Property**” of the part. In this problem the part is made of steel and assumed to be linear elastic with Young’s modulus (E) of 193 GPa and Poisson’s ratio ( $\nu$ ) of 0.3. Thus, we will create a single linear elastic material with these properties.

**Property** module>Click **Create Material**   
>create...>Mechanical>Elasticity>Elastic>Isotropic type, E=193 Gpa,  $\nu=0.3$


Young's Modulus	Poisson's Ratio
193000	0.3

Then **Section** menu>create...  >Solid category, Homogenous type


**Section** menu>Assignment Manager...   
>create...>select whole part to assign the property to that part  
After Section assignment color of part will change into Green.

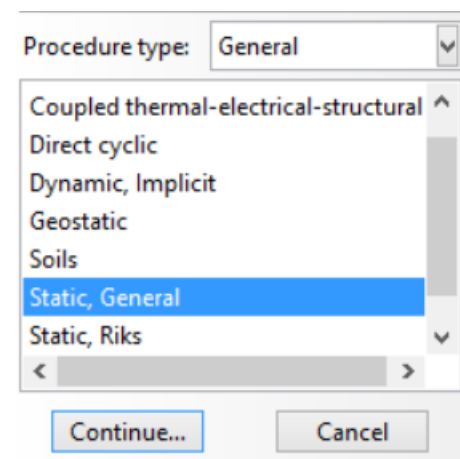


## III. Defining the assembly:

**Assembly** module>**Instance** menu   
>create...>select Part and select Instance type Independent (mesh on instance)

## IV. Configuring the analysis:

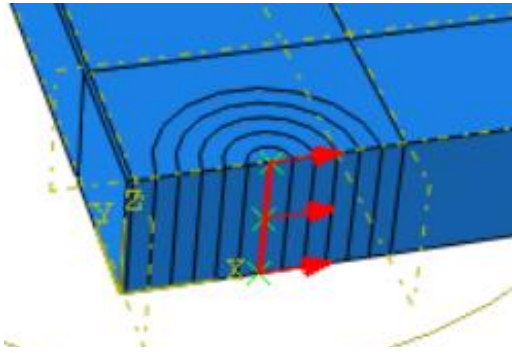
**Step** module>step menu>create...  >select Procedure type as General and click Static, General>continue...>Nlgeom off>click OK



## V. Defining the Crack :

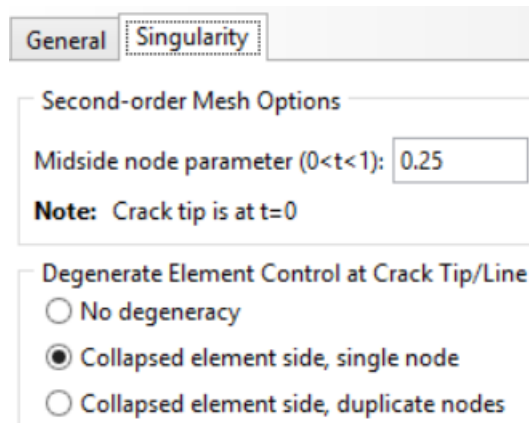
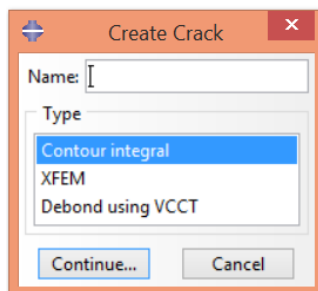
Because the crack is on side hence there is no need to define seam.

Click Special menu>Crack>create...>**Contour Integral type**>then select *Crack Front*, *Crack tip*, and *q-vector*.



**Figure 4.9: crack extension direction shown by q-vector**

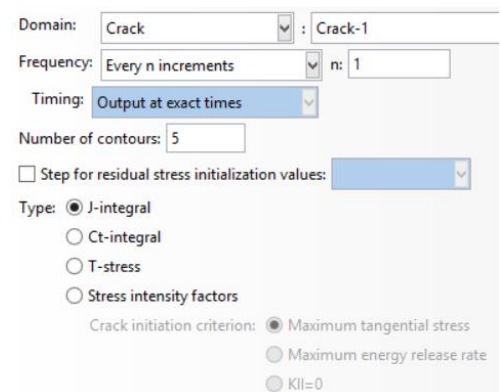
Since our part is linear elastic hence choose *strain singularity* and put *Midside node parameter* value as .25 and choose *Collapsed element side, single node*



## VII. Defining the History Output


After creating crack always assign History Output Requests from step module. **Step module>Output menu> History**

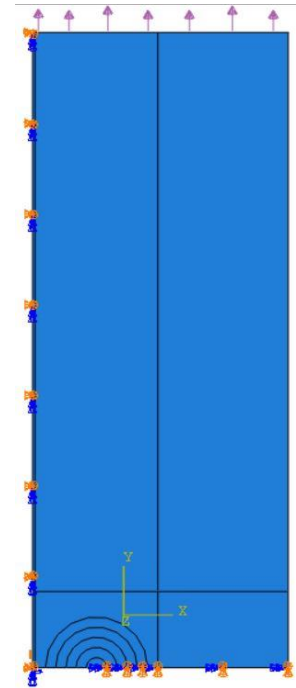
**Output Requests>create...**  
>continue...>select **Crack** in *Domain>Number of Contours: 5>select J-integral*



Do same to select **Stress Intensity Factors** and create another History Output Request.

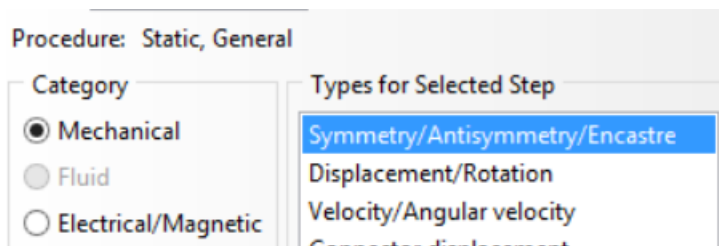
### VIII. Applying Boundary Conditions and Loads to the model

**Load** module>**Load** menu>create...  >select step, *Mechanical* category, *Pressure*>now select surface for load (top and bottom)>*Uniform* Distribution, *Magnitude* -10 Mpa (because of tensile in nature) .

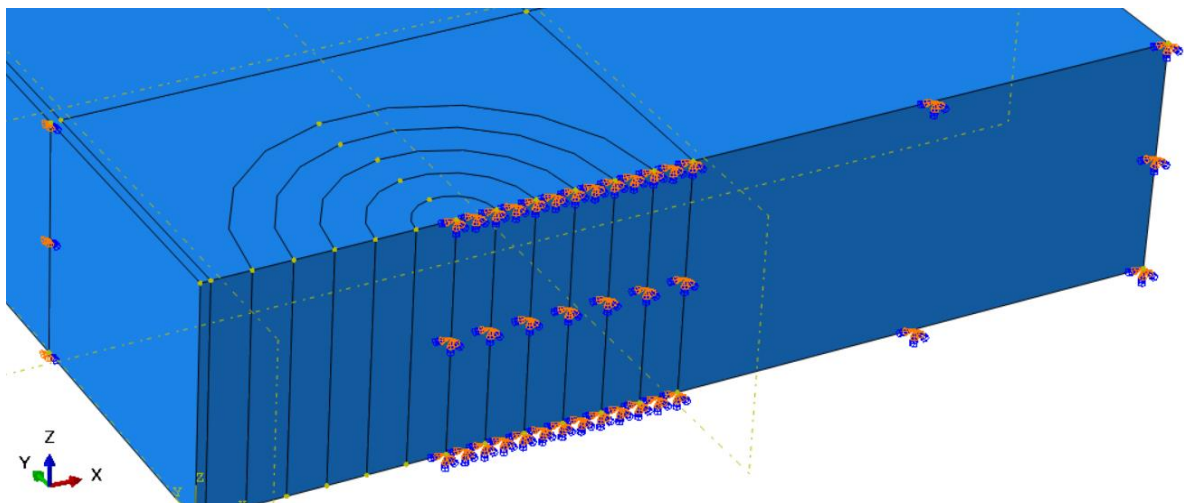


For Boundary condition click create Boundary condition 

Then select mechanical category and **encastre** option.

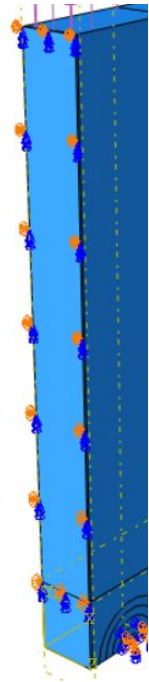


Select the lower bottom region and click done.



Again create a boundary condition for left face as **YASYMM**  
( $U_1=U_3=UR_2=0$ )

- XASYMM ( $U_2 = U_3 = UR_1 = 0$ ; Abaqus/Standard only)
- YASYMM ( $U_1 = U_3 = UR_2 = 0$ ; Abaqus/Standard only)
- ZASYMM ( $U_1 = U_2 = UR_3 = 0$ ; Abaqus/Standard only)




### IX. Meshing the model:

Mesh module>mesh menu>controls...  >select *crack front cell region*>select

Wedge element

now select *rest part* and choose **Hex** element and sweep, **Medial Axis Algorithm**.

Mesh menu>instance...  >ok to mesh the part instance.

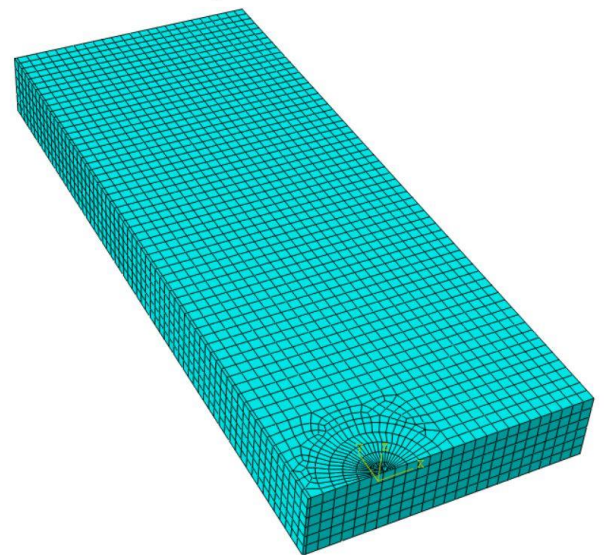
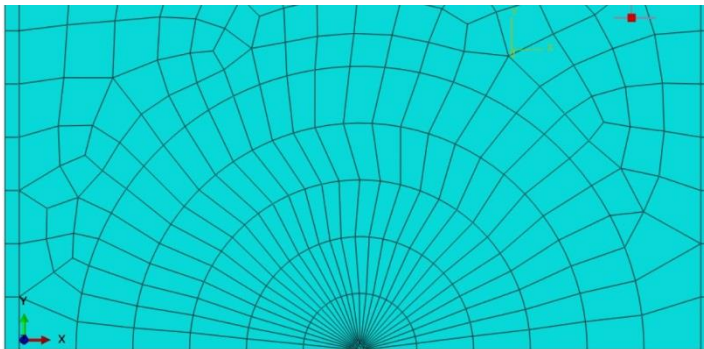


Figure 4.10: 3D centre through crack mesh

## X. RESULTS :

In the visualization module, we can get the deformed part and different output like stress, strain, displacement, translation which we have set in the field outputs. Also we can get results for crack like J-Integral, stress intensity factor which are set in History outputs.

Below are the different contours of deformed part

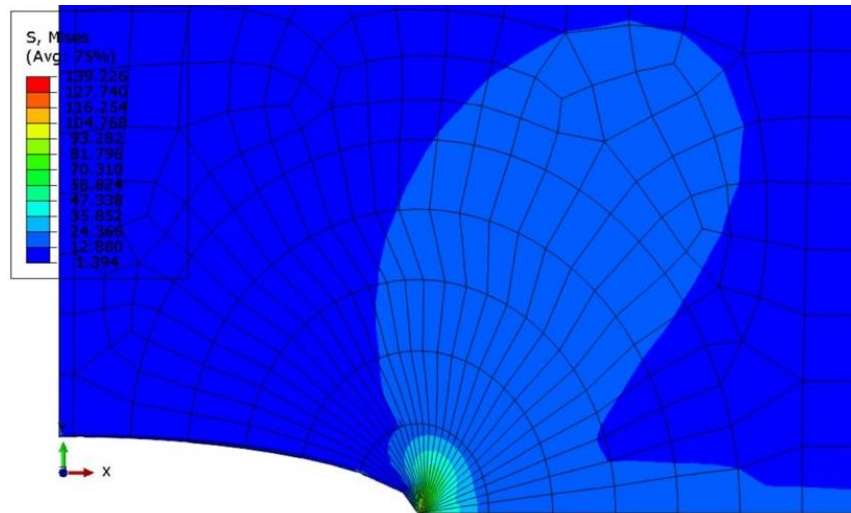


Figure 4.12: 3D centre crack von-mises stress contour

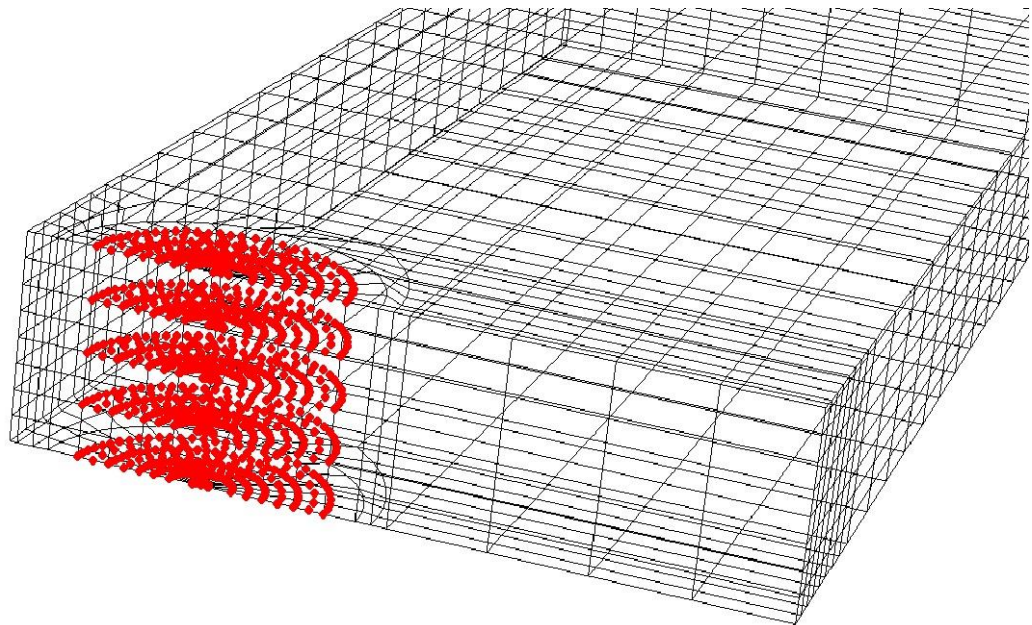
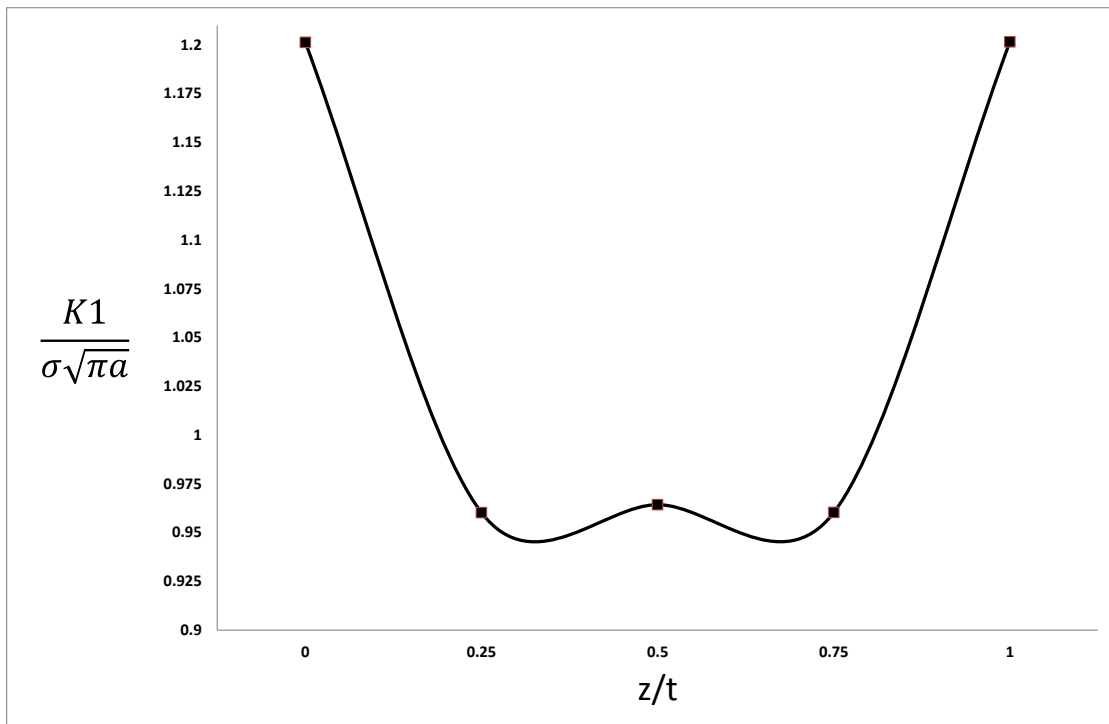


Figure 4.11: J-Contour layers along the thickness of plate

The values of  $K_I$  have been tabulated below with respect to the corresponding layer (relative position  $z$  with respect to plate thickness  $t$ ). For accuracy, the values obtained from the J-Integral of the contour at the crack-tip have been omitted[35]

**Table 4.4: SIF results for various layers**

Layer no. [(z/t)]	$K_I$ (Contour II)	$K_I$ (Contour III)	$K_I$ (Contour IV)	$K_I$ (Contour V)	$K_I$ (Layer Avg.)
1[0]	106.026	106.315	106.627	106.877	106.4613
2[0.25]	84.6351	85.0375	85.2757	85.4489	85.0993
3[0.5]	84.9518	85.4019	85.6505	85.842	85.4616
4[0.75]	84.6373	85.0403	85.2785	85.4594	85.1039
5[1.00]	106.049	106.344	106.663	106.898	106.4885



**Figure 4.13: SIF variation over the plate**

## 4.5.2 Analytical Solutions

For the crack configuration considered for analysis and SIF determination, Irwin (1957), Brown(1966), Koiter(1956), Tada(1973) have suggested analytical solutions. The solutions proposed conform to the general equation  $K_I = \sigma\sqrt{\pi a} \cdot F\left(\frac{a}{b}\right)$ . The SIF value, determined from ABAQUS, has been compared with these analytical solutions, deviations, if any, have been noted.

1. Irwin (1957): 
$$F\left(\frac{a}{b}\right) = \sqrt{\frac{2b}{\pi a}} \tan \frac{\pi a}{2b}$$
2. Brown (1966): 
$$F\left(\frac{a}{b}\right) = 1 + 0.0128\left(\frac{a}{b}\right) - 0.288\left(\frac{a}{b}\right)^2 + 1.525\left(\frac{a}{b}\right)^3$$
3. Tada (1973) 
$$F\left(\frac{a}{b}\right) = \frac{1 + 0.5\left(\frac{a}{b}\right) + 0.370\left(\frac{a}{b}\right)^2 - 0.44\left(\frac{a}{b}\right)^3}{\sqrt{1 - \frac{a}{b}}}$$
4. Koiter(1956): 
$$F\left(\frac{a}{b}\right) = \frac{1 - 0.5\left(\frac{a}{b}\right) + 0.326\left(\frac{a}{b}\right)^2}{\sqrt{1 - \frac{a}{b}}}$$

**Table 4.5: SIF determined from analytical solutions**

Solution Method	$K_I \text{ MPa}\sqrt{\pi a}$
Irwin (1957)	93.4703
Brown (1966)	91.9751
Tada (1973)	91.8372
Koiter (1956)	89.5583

The determination of the SIF distribution is of vital importance in fracture mechanics analysis, with conventional FE solver packages, it is convenient to assess such problems. As tabulated above, we can see there is no major difference between published analytic values and those determined by ABAQUS. The differences are within benchmark limits prescribed by NAFEMS, UK [8]

## **CHAPTER 5**

### **HERTZ CONTACT ANALYSIS USING FINITE ELEMENT METHOD**

#### **5.1 Introduction**

Study of deformation of solids under contact is called contact mechanics, comprising of mechanics of material and continuum mechanics. Contact mechanics provides the information for safe and energy efficient design of mechanical elements in contact, while continuum mechanics provides for analysis of the kinematics and the mechanical behaviour of materials modelled as a continuous mass rather than as discrete particles. Heinrich Hertz introduced the idea on contact mechanics in 1881. In mechanical engineering and tribology, Hertzian contact stress is a description of the stress within mating parts. This kind of stress may not be significant most of the time, but may cause serious problems if not take it into account in some cases. After Hertz's work, people do a lot of study on the stresses arising from the contact between two elastic bodies. An improvement over the Hertzian theory was provided by Johnson et al. (around 1970) with the JKR (Johnson, Kendall, Roberts) Theory. In the JKR-Theory the contact is considered to be adhesive. And then a more involved theory (the DMT theory) also considers Van der Waals interactions outside the elastic contact regime, which give rise to an additional load. In general machines are designed with a set of elements to reduce cost, ease of assembly and manufacturability etc. One also needs to address stress issues at the contact regions between any two elements; stress is induced when a load is applied to two elastic solids in contact. If not considered and addressed adequately serious flaws can occur within the mechanical design and the end product may fail to qualify. Stresses formed by the contact of two radii can cause extremely high stresses, the application and evaluation of Hertzian contact stress equations can estimate maximum stresses produced and ways to mitigate can be sought. Hertz developed a theory to calculate the contact area and pressure between the two surfaces and predict the resulting compression and stress induced in the objects. The roller bearing assembly and spur



gear pair assembly is an example where the assembly undergoes fatigue failure due to contact stresses.

This chapter provides a brief introduction to the Hertzian contact stress theory and in this chapter Hertz contact stress values obtained by analytical calculation is validated using finite element analysis (ABAQUS®).

## **5.2 Hertz Contact Theory[41]**

Theoretically, the contact area of two spheres is a point, and it is a line for two parallel cylinders. As a result, the pressure between two curved surfaces should be infinite for both of these two cases, which will cause immediate yielding of both surfaces. However, a small contact area is being created through elastic deformation in reality, thereby limiting the stresses considerably. These contact stresses are called Hertz contact stresses, which were first studied by Hertz in 1881. The Hertz contact stress usually refers to the stress close to the area of contact between two spheres of different radii.

The Hertz contact theory remains the foundation for most contact problems encountered in engineering. It applies to normal contact between two elastic solids that are smooth and can be described locally with orthogonal radii of curvature such as a toroid. Further, the size of the actual contact area must be small compared to the dimensions of each body and to the radii of curvature. Hertz made the assumption based on observations that the contact area is elliptical in shape for such three-dimensional bodies. The Hertz equations are important in the engineering of kinematic couplings particularly if the loads carried are relatively high. The equations simplify when the contact area is circular such as with spheres in contact. At extremely elliptical contact, the contact area is assumed to have constant width over the length of contact such as between parallel cylinders.

Hertz theory does not account for tangential forces that may develop in applications where the surfaces slide or carry traction. Extensions to Hertz theory approximate this behaviour to reasonable accuracy.

Hertz stress refers to the stress and deformation generated on two cylindrical rollers in contact under applied load. The stresses in between two rollers are critical, as a single line contact takes place between the rollers. As the force flow lines will be intersecting at the contact region stress concentration takes place and high stress generated at contact occurs. In contrast this chapter focuses upon two dimensional, line contacts. This approach to modelling contact is more relevant to ground gears where the surface finish is generally consistent with a two dimensional, plane strain simplification.

### **5.2.1 Assumptions and Idealizations:**

In Hertz's classical theory of contact, he focused primarily on non-adhesive contact where no tension force is allowed to occur within the contact area. The following assumptions are made in determining the solutions of Hertzian contact problems:

- I. The strains are small and within the elastic limit.
- II. Each body can be considered an elastic half-space, i.e., the area of contact is much smaller than the characteristic radius of the body.
- III. The surfaces are continuous and non-conforming.
- IV. The bodies are in frictionless contact.

### **Characteristics of Contact Stresses**

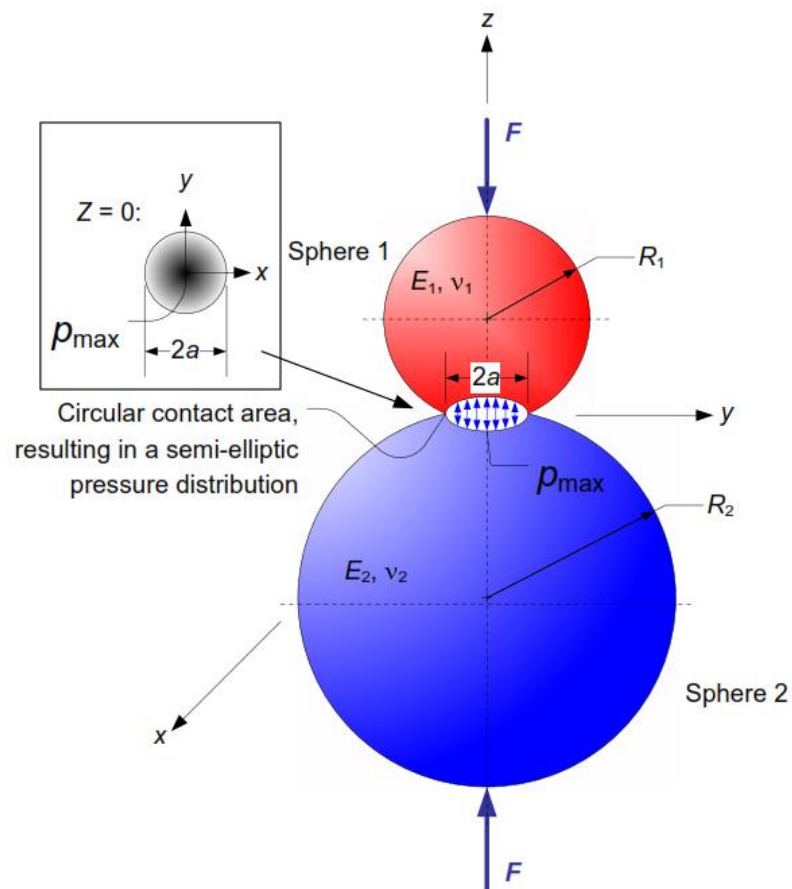
1. Represent *compressive* stresses developed from surface pressures between two curved bodies pressed together;
2. Possess an area of contact. The initial point contact (spheres) or line contact (cylinders) become area contacts, as a result of the force pressing the bodies against each other;
3. Constitute the principal stresses of a triaxial (three dimensional) state of stress;
4. Cause the development of a critical section below the surface of the body;
5. Failure typically results in flaking or pitting on the bodies' surfaces.

## Two Design Cases

Two design cases will be considered,

1. Sphere – Sphere Contact (Point Contact → Circular Contact Area)
2. Cylinder – Cylinder Contact (Line Contact → Rectangular Contact Area)

### 5.2.2 Sphere – Sphere Contact



**Figure 5.1: Two Sphere in Contact**

Consider two solid elastic spheres held in contact by a force  $F$  such that their point of contact expands into a circular area of radius  $a$ , given as:

$$a = \sqrt[3]{\frac{3F \left[ \frac{1-\nu_1^2}{E_1} + \frac{1-\nu_2^2}{E_2} \right]}{4 \left( \frac{1}{R_1} + \frac{1}{R_2} \right)}} \quad (5.1)$$

Where

$F$  = applied force

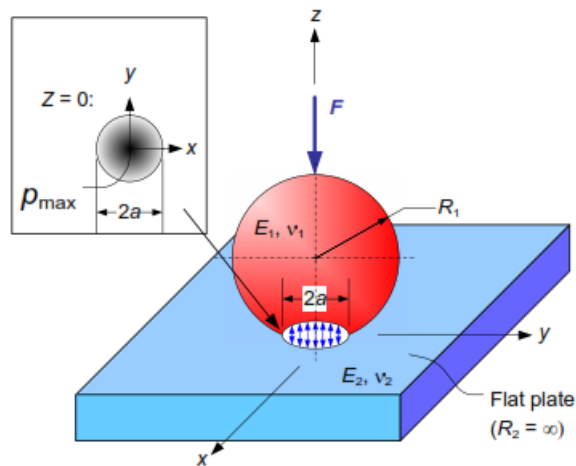
$\nu_1, \nu_2$  = Poisson's ratios for spheres 1 and 2

$E_1, E_2$  = elastic moduli for spheres 1 and 2

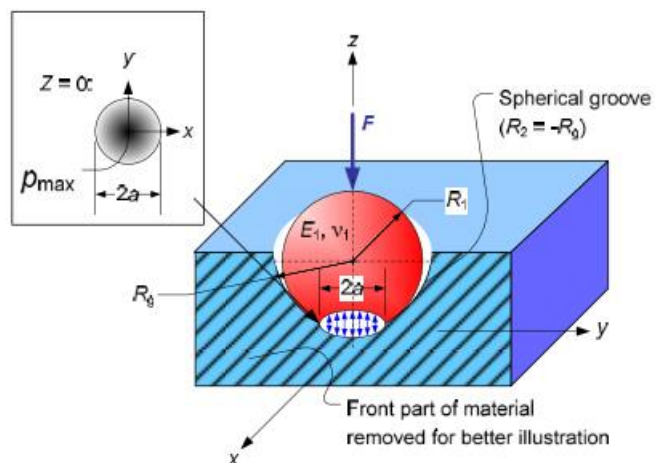
$R_1, R_2$  = radius of spheres 1 and 2

This general expression for the contact radius can be applied to two additional common cases:

1. Sphere in contact with a plane ( $R_2 = \infty$ );



2. Sphere in contact with an internal spherical surface or 'cup' ( $R_2 = -R$ )



Returning to the sphere-sphere case, the maximum contact pressure,  $P_{\max}$  occurs at the centre point of the contact area.

$$P_{\max} = \frac{3F}{2\pi a^2} \quad (5.2)$$

### State of Stress

- The state of stress is computed based on the following mechanics:
  1. Two planes of symmetry in loading and geometry dictates that  $\sigma_x = \sigma_y$ ;
  2. The dominant stress occurs on the axis of loading:  $\sigma_{\max} = \sigma_z$ ;
  3. The principal stresses are  $\sigma_1 = \sigma_2 = \sigma_x = \sigma_y$  and  $\sigma_3 = \sigma_z$  given  $\sigma_1, \sigma_2 \geq \sigma_3$ ;
  4. Compressive loading leads to  $\sigma_x, \sigma_y$ , and  $\sigma_z$  being compressive stresses.
- Calculation of Principal Stresses

The principal stresses  $\sigma_1$ ,  $\sigma_2$ , and  $\sigma_3$  are generated on the z-axis:

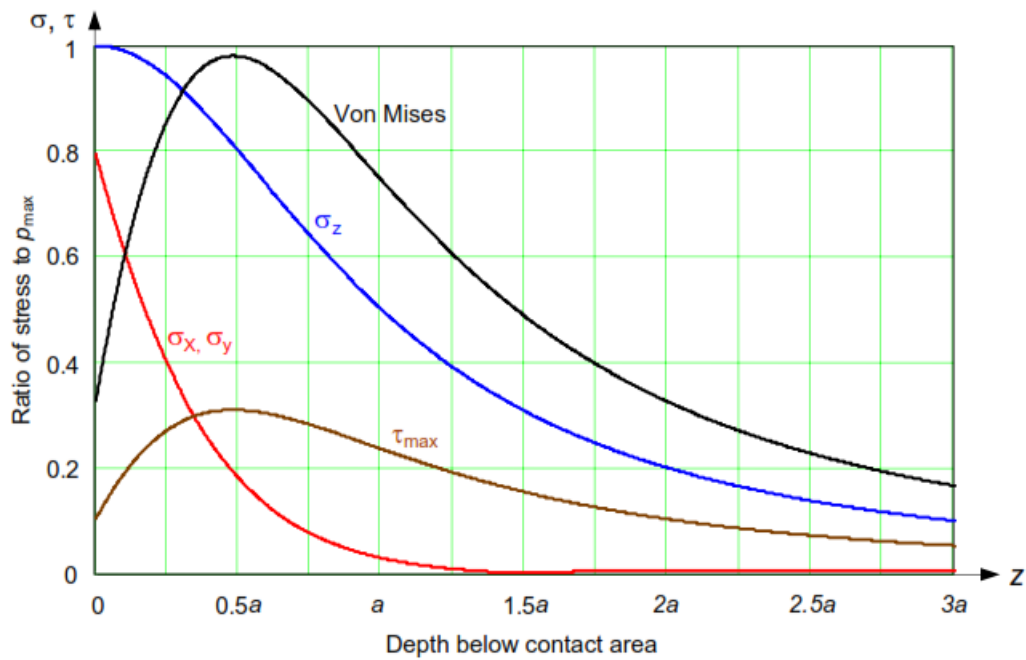
$$\sigma_1 = \sigma_2 = \sigma_x = \sigma_y = -p_{\max} \left[ (1 + \nu) \left( 1 - \left| \frac{z}{a} \right| \arctan \left| \frac{a}{z} \right| \right) - \frac{1}{2 \left( \frac{z^2}{a^2} + 1 \right)} \right] \quad (5.3)$$

$$\sigma_3 = \sigma_z = -p_{\max} \left( \frac{z^2}{a^2} + 1 \right)^{-1} \quad (5.4)$$

The Principal shear stresses are found as:

$$|\tau_1| = |\tau_2| = \tau_{\max} = \left| \frac{\sigma_1 - \sigma_3}{2} \right| \quad |\tau_3| = 0 \quad (5.5)$$

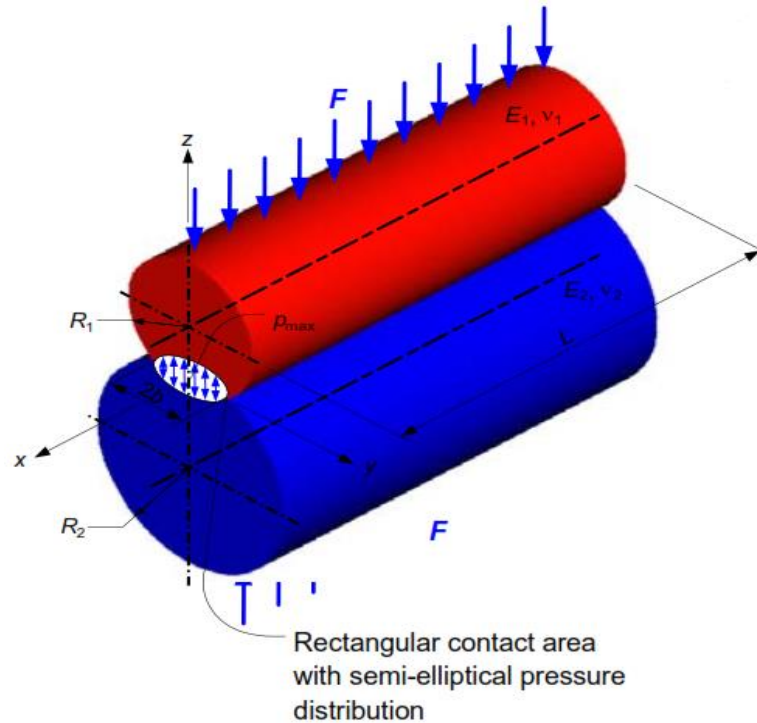
If the maximum shear stress,  $\tau_{\max}$ , and principal stresses,  $\sigma_1, \sigma_2$ , and  $\sigma_3$ , are plotted as a function of maximum pressure,  $p_{\max}$ , below the surface contact point, the plot of Figure 5.2 is generated. This plot, based on a Poisson's ratio of  $\nu = 0.3$ , reveals that a critical section exists on the load axis, approximately  $0.48a$  below the sphere surface. Many authorities theorize that this maximum shear stress is responsible for the surface fatigue failure of such contacting elements; a crack, originating at the point of maximum shear, progresses to the surface where lubricant pressure wedges a chip loose and thus creates surface pitting.



**Figure 5.2: Magnitude of the stress components below the surface as a function of maximum pressure of contacting spheres.**

### 5.2.3 Cylinder–Cylinder Contact

Consider two solid elastic cylinders held in contact by forces  $F$  uniformly distributed along the cylinder length  $L$ .



**Figure 5.3: Two Cylinders in Contact**

The resulting pressure causes the line of contact to become a rectangular contact zone of half- width  $b$  given as:

$$b = \sqrt{\frac{4F \left[ \frac{1-\nu_1^2}{E_1} + \frac{1-\nu_2^2}{E_2} \right]}{\pi L \left( \frac{1}{R_1} + \frac{1}{R_2} \right)}} \quad (5.6)$$

Where  $F$  = applied force

$\nu_1, \nu_2$  = Poisson's ratios for spheres 1 and 2

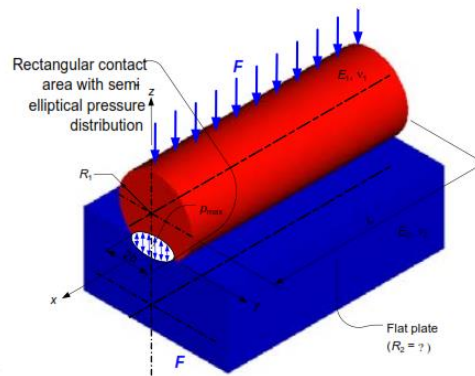
$E_1, E_2$  = elastic moduli for spheres 1 and 2

$R_1, R_2$  = radius of spheres 1 and 2

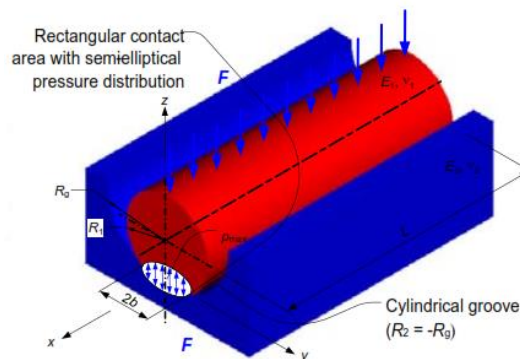
$L$  = length of cylinders 1 and 2 ( $L_1 = L_2$  assumed)

This expression for the contact half-width,  $b$ , is general and can be used for two additional cases which are frequently encountered:

1. Cylinder in contact with a plane, e.g. a rail ( $R_2 = \infty$ );



2. Cylinder in contact with an internal cylindrical surface, for example the race of a roller bearing ( $R_2 = -R$ ).



The maximum contact pressure between the cylinders acts along a longitudinal line at the center of the rectangular contact area, and is computed as:

$$P_{\max} = \frac{2F}{\pi b L} \quad (5.7)$$

### State of Stress

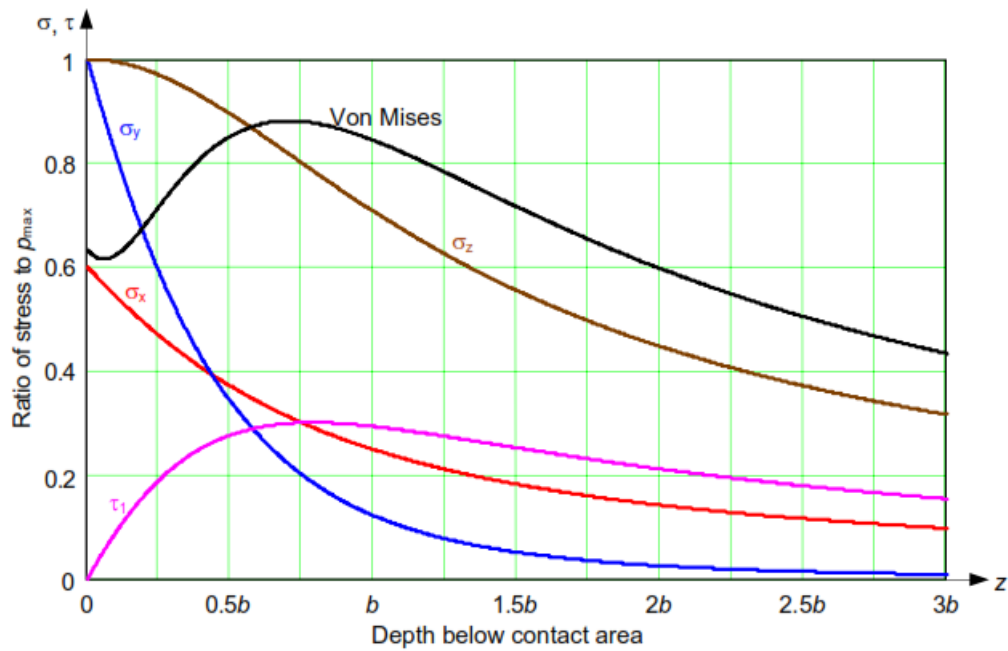


- The state of stress is computed based on the following mechanics:
  1. One planes of symmetry in loading and geometry dictates that  $\sigma_x \neq \sigma_y$  ;
  2. The dominant stress occurs on the axis of loading:  $\sigma_{\max} = \sigma_z$  ;
  3. The principal stresses are  $\sigma_x$  ,  $\sigma_y$  and  $\sigma_3 = \sigma_z$
  4. Compressive loading leads to  $\sigma_x$ ,  $\sigma_y$ , and  $\sigma_z$  being compressive stresses.

The principal stresses  $\sigma_1$ ,  $\sigma_2$ , and  $\sigma_3$  are generated on the z-axis.

$$\begin{aligned}
 \sigma_1 = \sigma_x &= -2\nu p_{\max} \left[ \sqrt{\frac{z^2}{b^2} + 1} - \left| \frac{z}{b} \right| \right] \\
 \sigma_2 = \sigma_y &= -p_{\max} \left[ \left( 2 - \left( \frac{z^2}{b^2} + 1 \right)^{-1} \right) \sqrt{\frac{z^2}{b^2} + 1} - 2 \left| \frac{z}{b} \right| \right] \\
 \sigma_3 = \sigma_z &= -p_{\max} \left[ \sqrt{\frac{z^2}{b^2} + 1} \right]^{-1} \\
 \tau_1 &= \left| \frac{\sigma_2 - \sigma_3}{2} \right|, \quad \tau_2 = \left| \frac{\sigma_1 - \sigma_3}{2} \right|, \quad \tau_3 = \left| \frac{\sigma_1 - \sigma_2}{2} \right|
 \end{aligned} \tag{5.8}$$

When these equations are plotted as a function of maximum contact pressure up to a distance  $3b$  below the surface contact point, the plot of Figure 5.4 is generated. Based on a Poisson's ratio of 0.3, this plot reveals that  $\tau_{\max}$  attains a maxima for  $\zeta_b = z/b = 0.786$  and  $0.3p_{\max}$ .



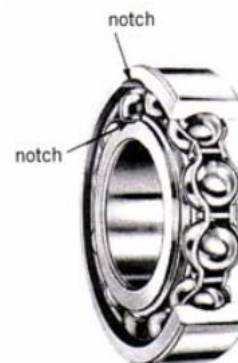
**Figure 5.4: Magnitude of stress components below the surface as a function of maximum pressure for contacting cylinders.**

### 5.2.4 Applications

The stresses and deflections arising from the contact between two elastic solids have practical application in hardness testing, wear and impact damage of engineering ceramics, the design of dental prostheses, gear teeth, and ball and roller bearings. Principles of contact mechanics are implemented towards applications such as locomotive wheel-rail contact, coupling devices, braking systems, tires, bearings, combustion engines, mechanical linkages, gasket seals, metalworking, metal forming, ultrasonic welding, electrical contacts, and many others. Current challenges faced in the field may include stress analysis of contact and coupling members and the influence of lubrication and material design on friction and wear. Applications of contact mechanics further extend into the micro- and nanotechnological realm.



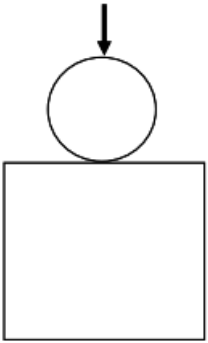
Gears



Rotary ball bearing

## 5.3 Hertz contact modelling in ABAQUS® (2D Cylinder Roller Contact)

### 5.3.1 Problem Description [42]

Title	2D Cylinder Roller Contact
Contact features	<ul style="list-style-type: none"> <li>• Advancing contact area</li> <li>• Curved contact surfaces</li> <li>• Deformable-deformable contact</li> <li>• Friction stick-slip along the contact line</li> <li>• Comparison of linear and quadratic elements</li> </ul>
Geometry	<p>2D plane strain</p> <ul style="list-style-type: none"> <li>• Block height = 200 mm</li> <li>• Block width = 200 mm</li> <li>• Cylinder diameter = 100 mm</li> </ul> 
Material properties	$E_{punch} = 210 \text{ kN} / \text{mm}^2$ $E_{foundation} = 70 \text{ kN} / \text{mm}^2$ $\nu_{punch} = \nu_{foundation} = 0.3$
Analysis type	<p>Linear elastic material          Geometric non-linearity          Non-linear boundary conditions</p>
Displacement boundary conditions	<p>Symmetry displacement constraints (half symmetry)          Bottom surface of the foundation is fixed (<math>u_x = u_y = 0</math>)</p>
Applied loads	Vertical point load $F = 35 \text{ kN}$
Element type	<p>2D plane strain</p> <ul style="list-style-type: none"> <li>• 4 node linear elements</li> </ul>
Contact properties	<p>2 different cases:</p> <ul style="list-style-type: none"> <li>• coefficient of friction <math>\mu = 0.0</math>(frictionless)</li> </ul>
FE results	<ol style="list-style-type: none"> <li>1. Plot of contact pressure against distance from centre of contact</li> <li>2. Comparison of result with Analytical solution</li> </ol>

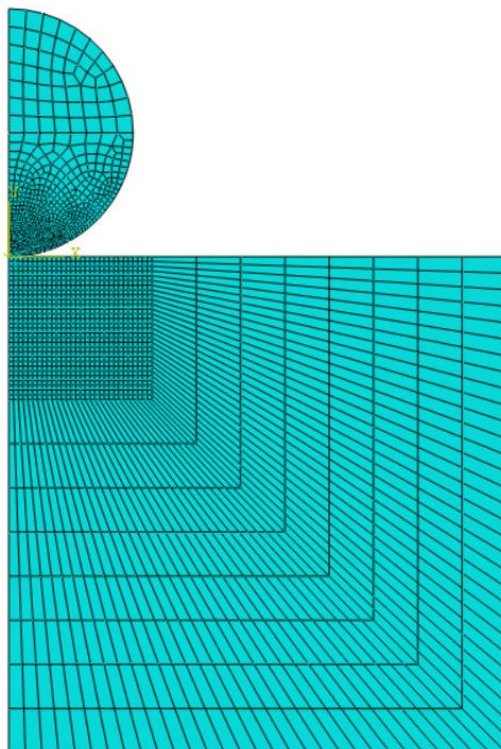
A steel cylinder is pressed into an aluminium block. It is assumed that the material behaviour for both materials is linear elastic. The cylinder is loaded by a

point load with magnitude  $F = 35 \text{ kN}$  in the vertical direction. A 2D approximation (plane strain) of this problem is assumed to be representative for the solution. An analytical solution for the frictionless is known.

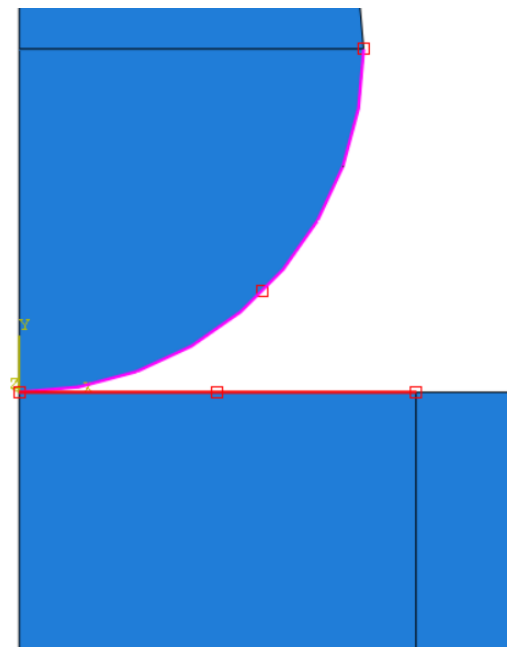
### 5.3.2 FEM Solution

A set of numerical solutions has been obtained with the FE programs Abaqus/Standard. Typical element meshes applied for the determination of the target solutions are shown in Figure 5.6. The block consisted of 1380 elements and the cylinder of 1199 elements. Numerical solutions have been obtained with plane strain linear elements using reduced integration and with fully integrated quadratic plane strain elements (CPE4R) (applied nominal thickness 1 mm)

In the contact algorithm, hard contact (i.e. based on direct coupling of the displacements using automatically generated constraint equations) has been used. For the simulations with frictionless contact The slave nodes (contacting nodes) have been set to the nodes on the cylinder; the master nodes (contacted nodes) have been set to the upper edge of the block.

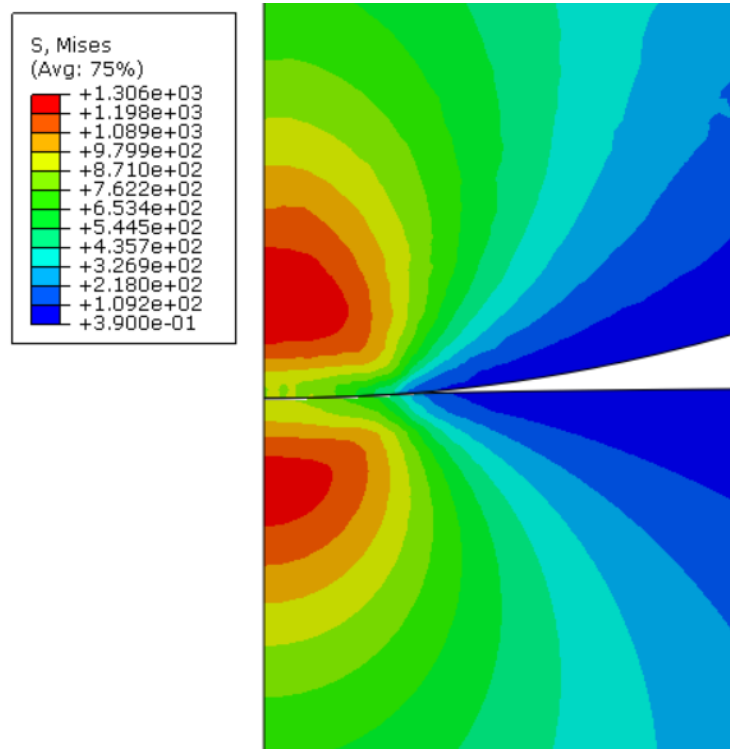


**Figure 5.6: 2d cylinder roller contact mesh**

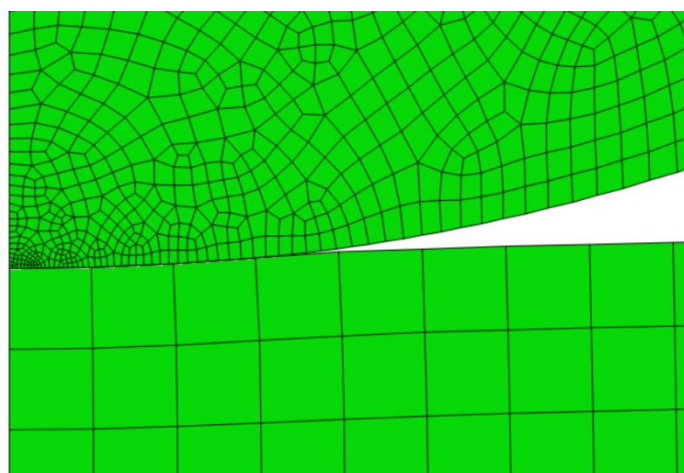


**Figure 5.5: 2d cylinder roller contact master-slave surface**

The obtained lengths of the contact zones in Abaqus Standard is  $5.88 < b < 6.42$ . The exact length of the contact zone cannot be determined due to the discrete character of contact detection algorithms (nodes are detected to be in contact with an element edge). It is clear however that the numerical solution is in good agreement with the analytical one.



**Figure 5.8: 2d cylinder roller contact von-mises stress contour at magnification factor=1**



**Figure 5.7: 2d cylinder roller contact deformed shape at magnification factor=1**

### 5.3.3 Analytical solution

An analytical solution for this contact problem can be obtained from the Hertzian contact formulae [section 5.2.3] for two cylinders (line contact).

The half contact width 'b' is given by Equation (5.6). Take  $F= 35000$  N,  $\nu_1=\nu_2=0.3$ ,  $E_1=210000$  MPa,  $E_2=70000$  MPa,  $R_1=50$  mm,  $R_2=\infty$ ;  $L= 1$  mm

Then we get half contact width **b= 6.2146** mm

The maximum contact pressure is given by Equation (5.7) and we get max. contact pressure  **$P_{\max}= 3585.362$**  MPa

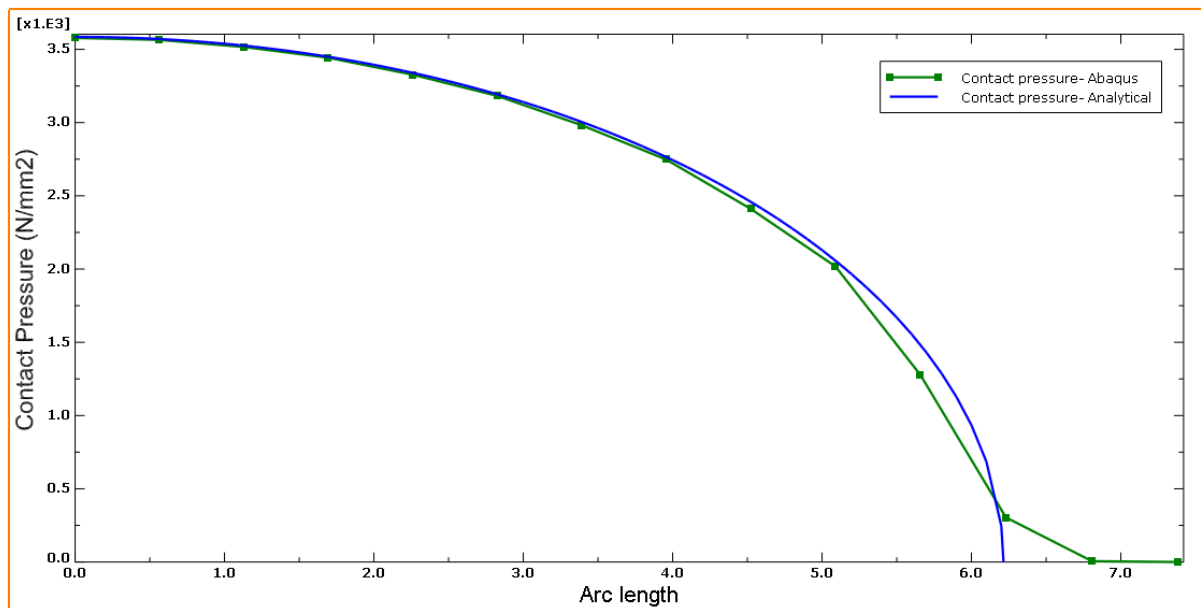
Using the normalised coordinate  $\xi = x/b$  with  $x$  the Cartesian x-coordinate, the pressure distribution is given by:

$$P= P_{\max} \cdot \sqrt{1 - \xi^2}$$

So

$$P= 3585.362 \cdot \sqrt{1 - \left(\frac{x}{6.2146}\right)^2}$$

A plot of the Hertzian contact solution for the pressure and the solutions along the nodes of the cylinder obtained with finite element solution ABAQUS is shown in Figure 5.9.



**Figure 5.9: Comparison of Analytical and FEM ABAQUS Solution**

Now calculation of Principal stresses and Maximum shear stress can be done by using Equation (5.8).

Below is the comparison Table 5.1 of theoretically obtained stresses and the stresses obtained by ABAQUS. Here stresses calculated at depth of  $z= 4.6064$  mm, hence  $z/b= .7412$ .

**Table 5.1: Comparison result of 2D cylinder roller contact of ABAQUS with Analytical**

	Analytical	ABAQUS	Error %
<b>Half contact width b mm</b>	6.2146	6.0459	2.71458
<b><math>\sigma_1=\sigma_x</math> MPa</b>	-1083.22	-1062.75	1.8901
<b><math>\sigma_2=\sigma_y</math> MPa</b>	-730.335	-673.91	7.725
<b><math>\sigma_3=\sigma_z</math> MPa</b>	-2880.41	-2868.58	0.4107
<b><math>\tau_{max}</math> MPa</b>	1075.038	1097.335	2.0741

### 5.3.4 Conclusion

The comparison of manual analytical result, and finite element analysis results shows the finite element analysis results are acceptable. As the difference in result is within 10%. This difference is due to the approximation made as two half cylinder instead of full cylinder. The result shows in order to obtain proper results in finite element analysis, proper elements has to be selected with suitable degrees of freedom, assigning appropriate contacts between element and by providing accurate boundary conditions helps to compute most accurate contact stress values. The value of contact stress is very important, as the stress value changes with contact area. The higher the contact area the stress generated will be less and vice-versa. In various engineering applications line contact exists between bearing, rollers, spur gears etc , therefore in order to capture accurate results proper care to be taken while meshing and assigning contacts depending on complexity of problem. The contact stress between rollers is important in order to ensure the stress generated is within elastic limits, this also helps predict accurately the fatigue life by plotting the value of stress in S-N curve (stress vs number of cycles) of the material. Based on required fatigue life the stress

values can be optimized by modifying permissible load carrying capacity or by changing roller dimensions.



## **CHAPTER 6**

# **FINITE ELEMENT FORMULATION IN METAL CUTTING**

### **6.1 Introduction**

The advent and continuous improvements of digital computers have made finite element analysis a useful analytical tool which has been applied very efficiently in almost every area of engineering field. One of the most important reasons that finite element analysis is so widely used is that it can be routinely used. There are a definite set of several basic and distinct steps used in the FEM simulations:

- 1) Discretization of the continuum.
- 2) Selection of the interpolation function.
- 3) Determination of the element properties.
- 4) Assembly of the element properties in order to obtain the system equations.
- 5) Determination of the constraints and other boundary conditions.
- 6) Solution of the system equations.
- 7) Computation of the derived variables.

### **6.2 Model Formulation**

The selection of an appropriate formulation or approach is of prime importance especially for problems involving nonlinearity and large deformations. There are mainly three ways to formulate the problems involving the motion of deformable materials, given as:

- Lagrangian approach
- Eulerian approach
- Arbitrary Lagrangian Eulerian (ALE) approach

The formulations are distinguished from each other by mesh descriptions, kinetics and kinematics description.

### **6.2.1 Lagrangian**

Lagrangian formulation is mainly used in solid mechanics problems. Here the FE mesh is attached to work piece material and cover the whole of the region under analysis. This makes it highly preferable when unconstrained flow of material is involved. Lagrangian formulation is broadly used in metal cutting simulation due to ability to determine geometry of the chip from incipient stage to steady state and this geometry is a function of cutting parameters, plastic deformation process and material properties. Therefore, boundaries and shape of the chip do not have to be known a priori. Besides, chip separation criteria can be defined to simulate discontinuous chips or material fracture in metal cutting models which are based on Lagrangian formulation.

Although there are many advantages of Lagrangian formulation, it has also shortcomings. Metal being cut is exposed severe plastic deformation and it causes distortion of the elements. Therefore, mesh regeneration is needed. Secondly, chip separation criteria must be provided. This drawback of formulation can be eliminated by using an updated Lagrangian formulation with mesh adaptivity or automatic remeshing technique.

### **6.2.2 Eulerian**

In Eulerian formulation, the FE mesh is spatially fixed and the material flow through the control volume which eliminates element distortion during process. Besides, fewer elements required for the analysis, thereby reducing the computation time. Cutting is simulated from the steady state and therefore there is no need for separation criteria in Eulerian based models.

The drawback of Eulerian formulation is a need in determining the boundaries and the shape of the chip prior to the simulation. Also the chip thickness, the tool-chip contact length and the contact conditions between tool-chip must be kept constant during analysis which makes Eulerian formulation does not correspond to the real deformation process during metal cutting.

### 6.2.3 Arbitrary Lagrangian-Eulerian (ALE)

The best features of Lagrangian and Eulerian formulations have been combined and called Arbitrary Lagrangian-Eulerian (ALE). In ALE formulation, the FE mesh is neither fixed spatially nor attached to the work piece material. The mesh follows the material flow and problem is solved for displacements in Lagrangian step, while the mesh is repositioned and problem is solved for velocities in Eulerian step.

The idea used in metal cutting simulation is to utilize Eulerian approach for modelling the area around the tool tip where cutting process occurs. Therefore, severe element distortion is avoided without using remeshing. Lagrangian approach is utilized for the unconstrained flow of material at free boundaries. Furthermore shape of the chip occurs as a function of plastic deformation of the material. For an explanatory demonstration of the differences between Eulerian, Lagrangian and ALE descriptions see Figure 6.1

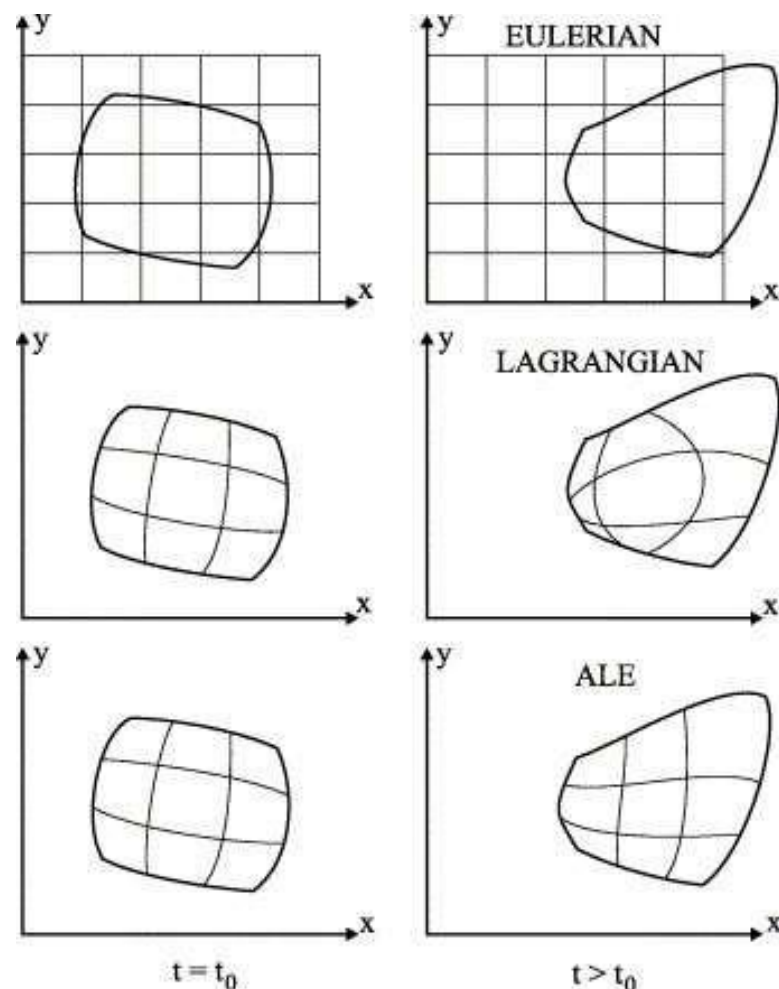


Figure 6.1: An explanatory demonstration of the Eulerian, Lagrangian and ALE formulations. Figure from Proudian [44]

### 6.2.3.1 Boundaries in ALE methods

The ALE method can be applied to a wide range of problems by defining the movement of the mesh and the form of the boundaries. There are two primary types of boundaries for ALE domains, Eulerian and Lagrangian boundaries, with the main difference that the material points are allowed to flow across Eulerian boundaries while across Lagrangian boundaries they are not. At a Lagrangian boundary the nodes follow the material in the direction normal to the boundary making the mesh cover the same material domain during the entire analysis.

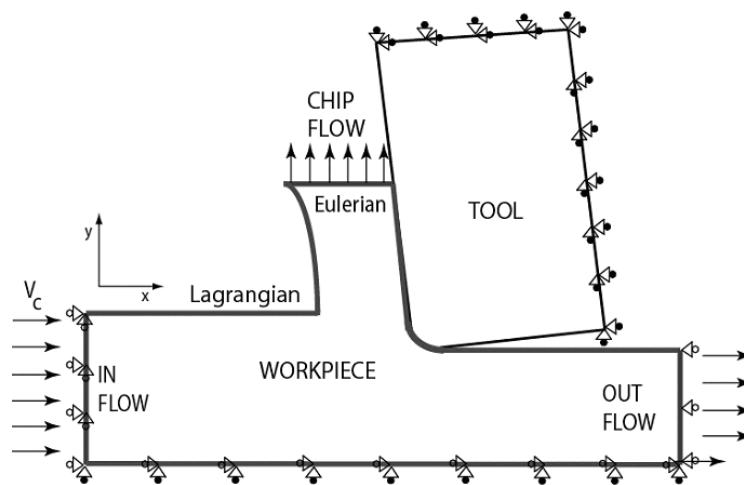


Figure 6.2: Eulerian and Lagrangian boundary conditions in ALE simulation(Source: Ozel, et al. 2007)[45]

### 6.2.3.2 Mesh-update procedures

The mesh-update procedure is defined by several different algorithms and choices e.g. the remeshing criteria - which nodes to move and when, smoothing algorithms and geometric aspects such as: geometric enhancement and curvature refinement.

ALE adaptive meshing is not performed equally over the entire mesh but serves to reshape the mesh where necessary. The ALE adaptive mesh algorithm in ABAQUS always strives to reduce element distortion by improving element aspect ratio (i.e. to get all sides of the element to be of the same length) sometimes under the option to preserve initial mesh gradation [35].

There are several algorithms for relocating the nodes to the new mesh. In ABAQUS/Explicit there are two quite basic options, either a volume-weighted average of the element centres or an average of the positions of the adjacent nodes connected by an element edge. A more complicated smoothing algorithm is based on a higher-order average of the eight (in the 2D case) nearest nodes.

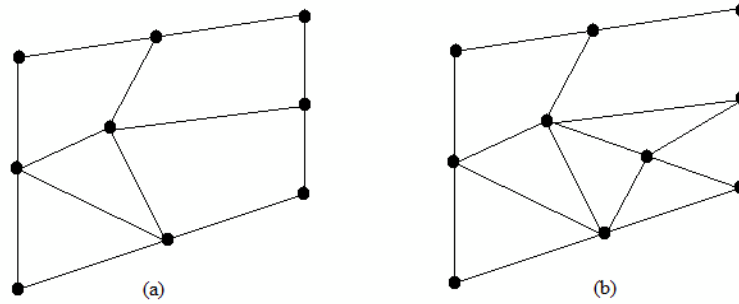
In ABAQUS/Explicit there is an extra choice for the mesh-update procedure called curvature refinement. The functionality of this is to "pull more elements into areas of high curvature" [35].

The remeshing criteria in ABAQUS is not based on an error function but simply stated as a frequency telling how often the mesh is to be updated. Another parameter stated is the number of iterations for the relocation of the nodes. In ABAQUS/Explicit these iterations, which are performed according to chosen smoothing algorithm, are called mesh sweeps. The mesh sweeps can be based either on the current nodal position (often used for Lagrangian problems) or on the nodal position in the end of the previous adaptive mesh increment (recommended for Eulerian problems)

### **6.3 Meshing**

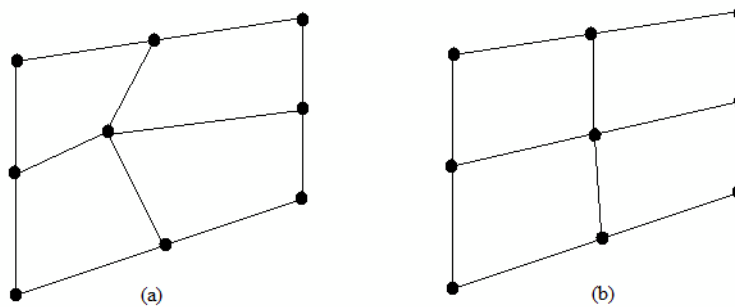
A continuous region is divided discrete region called elements in FE analysis. This procedure is called discretization or meshing. Initial designed FE mesh can not hold its original shape and it is distorted due to severe plastic deformation during metal cutting or metal forming processes. The distortion causes convergence rate and numerical errors. To handle with this problem a new FE mesh must be generated in means of changing the size and distribution of the mesh. This is called adaptive mesh procedure.

One of adaptive mesh procedure is remeshing technique and it includes the generation of a completely new FE mesh out of the existing distorted mesh. Second one is called refinement technique which is based on increasing the local mesh density by reducing the local element size as shown in Figure 6.4



**Figure 6.4: Refinement: (a) Initial local mesh, (b) Reducing element size**

The last adaptive mesh technique is smoothing which includes reallocating the nodes to provide better element shapes as shown in Figure 3.3



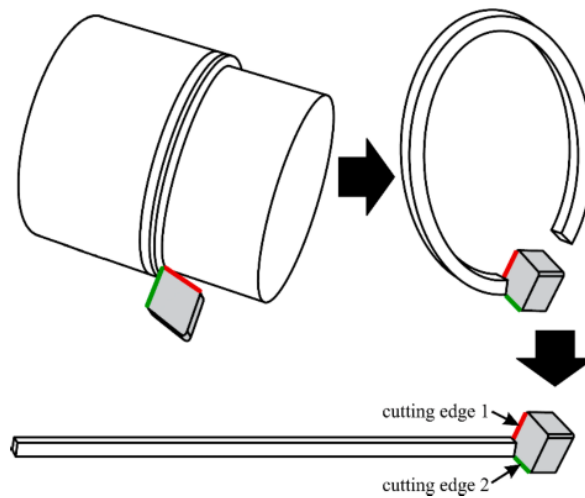
**Figure 6.3: Smoothing: (a) Initial local mesh, (b) Reallocating of the nodes**

The adaptive mesh procedure decreases solution errors during calculation therefore it increases the accuracy of the simulation. For these reasons, the adaptive mesh procedure must be used in FE simulations including severe plastic deformation such as metal cutting and metal forming.

## 6.4 Geometry Modelling

Creating the geometry of the problem domain is the first and foremost step in any analysis. The actual geometries are usually complex. The aim should not be simply to model the exact geometry as that of the actual one, instead focus should be made on how and where to reduce the complexity of the geometry to manageable one such that the problem can be solved and analyzed efficiently without affecting the nature of problem and accuracy of results much. Hence, proper understanding of the mechanics of the problem is certainly required to analyze the problem and examine the geometry of the problem domain. It is generally aimed to make use of 2 D elements rather than 3 D elements since this can drastically reduce the number of degrees of freedom (DOFs).

To simulate a three dimensional process in two dimensions it is essential to define a proper projection of the 3D case to 2D. The turning process is simplified by considering only a small segment from the workpiece. Since the depth of cut, feed rate and the simulated workpiece arc is negligibly small compared to the radius of the workpiece, the segment is considered to be straight. In this particular machining process, two edges of the tool are involved in cutting, while in the 2D simulation, only one cutting edge could be taken into account. Therefore, before the simulations, it also has to be decided which cutting edge is considered as



**Figure 6.5: Illustration of the 3D-2D projection**

dominant, and which one is neglected. In this study, the simulated cutting edge is indicated in Figure 6.5 [17] as cutting edge 1.

## 6.5 Governing Equations

The governing equations of a body undergoing deformation consists of two sets of equations, namely, the conservations laws of physics and the constitutive equations. The conservation laws can be applied to body of any material. But to distinguish between different materials undergoing deformation of varied degrees, one needs the constitutive equations.

### 6.5.1 Conservation laws:

The mass, momentum and energy equations governing the continuum are given as follows:

$$\dot{\rho} + \rho \operatorname{div} \vec{v} = 0 \quad (6.1)$$

$$\rho \dot{\vec{v}} = \vec{f} + \text{div } \sigma \quad (6.2)$$

$$\rho \dot{e} = \sigma : \mathbf{D} - \text{div } \vec{q} + r \quad (6.3)$$

where  $\rho$  is the mass density,  $\vec{v}$  material velocity,  $\vec{f}$  body forces,  $\sigma$  Cauchy stress tensor,  $e$  specific internal energy,  $\mathbf{D}$  strain rate tensor,  $\vec{q}$  heat flux vector and  $r$  is body heat generation rate. The superposed ‘ $\dot{\cdot}$ ’ denotes material derivative in a Lagrangian description and ‘ $:$ ’ denotes contraction of a pair of repeated indices which appear in the same order such as,  $A:B = A_{ij}B_{ij}$ .

The basic idea of using FEM is to discretize the above equations and then to seek a solution to the momentum equation.

### 6.5.2 Workpiece material constitutive equations:

Constitutive equations describe the thermo-mechanical properties of a material undergoing deformation. Based on the simplicity or complexity of the material behavior, there could be one constitutive equation or a set of constitutive equations that relate the deformation in the body to the stresses. The elastic response can be described by Hook’s law. Whereas, the constitutive equations of plasticity deal with yield criterion, flow rule and strain hardening rule. The yield criterion describes the stress state when yielding occurs, the flow rule defines increment of plastic strain when yielding occurs, and the hardening rule describes how the material is strain hardened as the plastic strain increases. For large deformation problems, as in case of machining, plasticity models based on von Mises yield criterion and Prandtl–Reuss flow rule are generally used to define the isotropic yielding and hardening [46].

It is known that during cutting process, the workpiece material is generally subjected to high levels of, strain, strain rate and temperature which significantly influences flow stress. Thus, accurate and reliable rate-dependent constitutive models are required that can reflect such phenomenon effectively. Johnson–Cook constitutive equation is one such model that considers the flow stress behavior of the work materials as multiplicative effects of strain, strain rate and temperature, given as follows [47]



$$\sigma = \left( A + B\varepsilon^n \right) \left( 1 + C \ln \frac{\dot{\varepsilon}}{\dot{\varepsilon}_0} \right) \left( 1 - \left( \frac{T - T_r}{T_m - T_r} \right)^m \right) \quad (6.4)$$

The first parenthesis is elastic-plastic term and it represents strain hardening. The second one is viscosity term and it shows that flow stress of material increases when material is exposed to high strain rates. The last one is temperature softening term. A, B, C, n and m are material constants that are found by material tests. T is instantaneous temperature,  $T_r$  is room temperature and  $T_m$  is melting temperature of a given material.

Johnson-Cook material model assumes that flow stress is affected by strain, strain rate and temperature independently.

## 6.6 Damage and Failure Model

A damage model should be incorporated in the damage zone along with the material as a chip separation criterion in order to simulate the movement of the cutting tool into workpiece without any mesh distortion near the tool tip. Specification of damage model includes a material response (undamaged), damage initiation criterion, damage evolution and choice of element deletion.

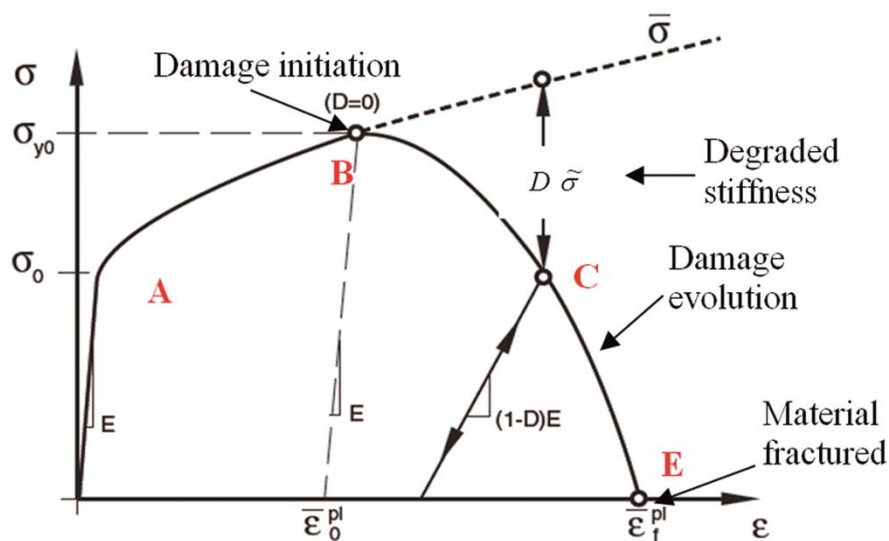


Figure 6.6: Stress-strain curve with damage degradation

Damage initiation criterion is referred to as the material state at the onset of damage. In the present case, Johnson–Cook damage initiation criterion has been employed. This model makes use of the damage parameter  $\omega_D$  defined as the sum of the ratio of the increments in the equivalent plastic strain  $\Delta\bar{\epsilon}^P$  to the fracture strain  $\epsilon^f$ , given as follows [35].

$$\omega_D = \sum \frac{\Delta\bar{\epsilon}^P}{\epsilon^f} \quad (6.5)$$

The Johnson-Cook damage model assumes that the equivalent strain at failure is of the form:

$$\bar{\epsilon}_f = \left[ D_1 + D_2 \exp\left(D_3 \frac{P}{\bar{\sigma}}\right) \right] \left[ 1 + D_4 \ln\left(\frac{\dot{\bar{\epsilon}}^{pl}}{\dot{\bar{\epsilon}}_0}\right) \right] \left[ 1 + D_5 \left(\frac{T - T_r}{T_m - T_r}\right) \right] \quad (6.6)$$

where P is the hydrostatic pressure and  $D_1$  to  $D_5$  are failure parameters determined experimentally. The damage constants can be determined by performing several experiments such as tensile test, torsion test and Hopkinson bar test. On the basis of results obtained, a graph is generally plotted between equivalent plastic strain at fracture and pressure stress ratio

The damage initiation criterion is met when  $\omega_D$  (Eq. (6.5)) reaches one [35]. Once the element satisfies the damage initiation criterion, it is assumed that progressive degradation of the material stiffness occurs, leading to material failure based on the damage evolution.

At any given time during the analysis, the stress tensor in the material is given by:

$$\sigma = (1 - D) \bar{\sigma} \quad (6.7)$$

Where  $\bar{\sigma}$  is the effective (undamaged) stress tensor computed in the current increment. When overall damage variable D reaches a value 1, it indicates that the material has lost its load carrying capacity completely. At this point, failure occurs and the concerned elements are removed from the computation.

The effective plastic displacement ( $\bar{u}^P$ ), after the damage initiation criterion is met can be defined with the evolution law as follow:

$$\bar{u}^p = L_e \bar{\epsilon}^p \quad (6.8)$$

where  $L_e$  is the characteristic length of the element and  $\bar{\epsilon}^p$  equivalent plastic strain. When a linear evolution of the damage variable with plastic displacement is assumed, the variable increases as per the following [61]:

$$D = \frac{L_e \bar{\epsilon}^p}{\bar{u}_f^p} = \frac{\bar{u}^p}{\bar{u}_f^p} \quad (6.9)$$

$$\bar{u}_f^p = \frac{2G_f}{\sigma_{y0}} \quad (6.10)$$

where  $\bar{u}_f^p$  is the plastic displacement at failure,  $G_f$  is the fracture energy per unit area and  $\sigma_{y0}$  is the value of the yield stress at the time when the failure criterion is reached.

The model ensures that the energy dissipated during the damage evolution process is equal to  $G_f$  only if the effective response of the material is perfectly plastic (constant yield stress) beyond the onset of damage. In this study,  $G_f$  is provided as an input parameter which is a function of fracture toughness  $K_C$ , Young's modulus  $E$  and Poisson's ratio  $\nu$  as given in the equation for the plane strain condition.

$$G_f = \left( \frac{1-\nu^2}{E} \right) K_C^2. \quad (6.11)$$

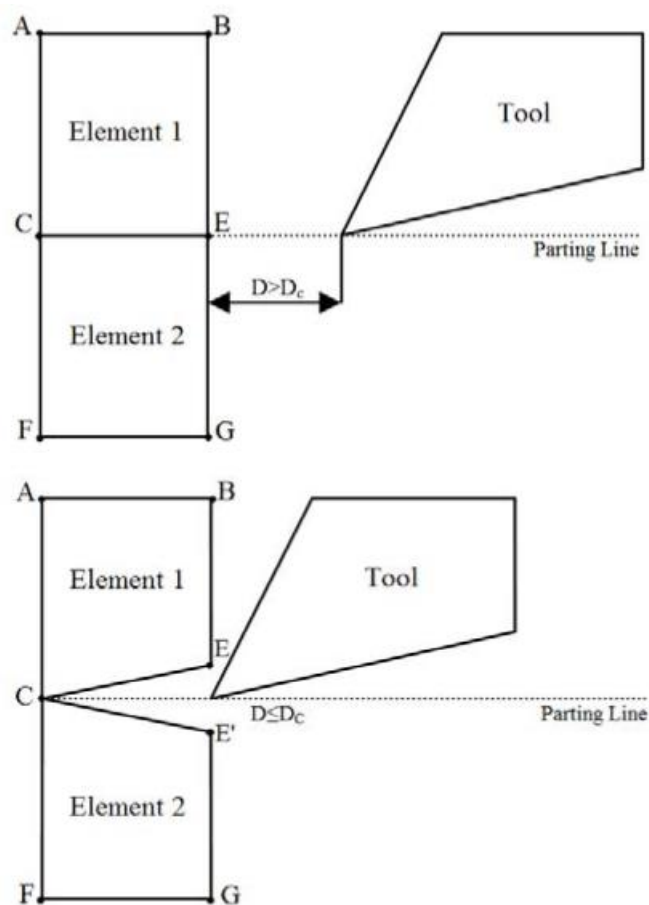
The ELEMENT DELETION = YES module along with the Johnson Cook damage model of the software enables to delete the elements that fail. This produces the chip separation and allows the cutting tool to penetrate further into the workpiece through a predefined path (damage zone).

## 6.7 Chip Separation Criteria

In real machining operations, continuous, discontinuous or segmented chips may occur. Two basic methods are used to provide real chip formation in a numerical method. First one is to define chip separation criteria along a pre-

defined line and the next one is to use continuous remeshing which is based on large plastic deformation.

A number of separation criteria can be grouped as geometrical and physical. According to geometrical criteria, chip separation is started when the tool tip approaches a node along the parting line within a critical distance. Then that node is separated from the work piece and it becomes part of the chip. This process can be seen in detail in Figure 6.7 [48]. When distance  $D$  between the tool tip and node  $E$  becomes equal or less than the critical distance  $D_c$ , the connectivity of the Element 2



**Figure 6.7: Geometrical Separation (Source: Mamalis, et al. 2001)**

changes and a new node  $E'$  occur in that element. Then the node  $E$  moves upwards along  $EB$  by small distance, whilst node  $E'$  moves downwards by a small distance along  $E'G$ .

This criterion is just based on geometrical considerations and the critical distance value is chosen arbitrarily. Because of that, it does not show real physical mechanism of chip formation. On the other hand chip separation can be easily

controlled. In literature, Komvopoulos and Erpenbeck (1990) used this technique as chip separation criteria to model orthogonal metal cutting.

According to the physical criteria, separation of nodes occurs when the value of predefined critical physical parameter is reached at a node or element. This critical physical parameter can be selected as strain, stress or strain energy density depending on work material properties and cutting conditions.

Strenkowski and Carroll (1985) used effective plastic strain criterion to simulate orthogonal cutting. When the effective plastic strain at a node closest to the tool tip is reached the predefined critical value, it is allowed to move from the work piece.

Physical criteria seem to be more accurate in modelling chip separation because they are based on work piece properties. However, the problem is to determine critical physical values for real process. For example, the strain energy of work piece material can be determined from a simple uniaxial tensile test of which mechanical conditions are significantly different from metal cutting. Therefore, using this value in modelling can not be reliable. Another example is using effective plastic strain. Effective plastic strain value changes significantly during the transition from transient to steady-state cutting and using this value as separation criterion can not act as a reliable criterion.

## **6.8 Friction Models**

Friction modelling plays significant role on results such as cutting forces, temperature and tool wear in metal cutting simulation. Hence, researchers focused on determining a friction model to represent the real behaviour of process. The most widely used ones in metal cutting simulation can be listed as follows.

### **6.8.1 Constant Coulomb**

In early metal cutting simulation, the simple Coulomb friction model was used on the whole contact zone with a constant coefficient of friction.

This model is defined as

$$\tau = \mu \sigma_n \quad (6.12)$$

Here,  $\tau$  is the frictional stress,  $\sigma_n$  is the normal stress and  $\mu$  is the coefficient of friction.

### **6.8.2 Constant Shear**

In shear friction model, frictional stress on rake face of tool is assumed to be constant and the low stress variation of  $\tau$  and  $\sigma_n$  are neglected.

This can be expressed by means of the following formulation:

$$\tau = mk \quad (6.13)$$

Where  $m$  is friction factor and  $k$  is shear flow stress of the work material.

### **6.8.3 Constant Shear in Sticking Zone and Coulomb in Sliding Zone**

According to Zorev (1963), two friction regions occur on rake face of tool. The first region is sticking zone where the frictional stress is constant. The next one is sliding zone where the normal stress is small. Therefore, constant shear friction model in sticking zone and Coulomb's theory in sliding zone can be used to model friction phenomenon.

The important thing in using this model is to determine the length of sticking and sliding zones. According to Shatla, et al. (2001), it was assumed that the length of the sticking region was equal to two times of the uncut chip thickness. However, it was noticed that the sticking region covered all the contact length in this way. Thus, Ozel(2006) [45] suggested that the length of the sticking zone was equal to the uncut chip thickness.

## **6.9 Chip-Tool Interface Model and Heat Generation**

A contact is defined between the rake surface and nodes of the workpiece material. Coulomb's law has been assumed in the present study to model the frictional conditions as the chip flows over the rake surface.

During the machining process, heat is generated in the primary shear deformation zone due to severe plastic deformation and in the secondary deformation zone due to both plastic deformation and the friction in the tool–chip interface. The steady state

two-dimensional form of the energy equation governing the orthogonal machining process is given as:

$$k \left( \frac{\partial^2 T}{\partial x^2} + \frac{\partial^2 T}{\partial y^2} \right) - \rho C_p \left( u_x \frac{\partial T}{\partial x} + v_y \frac{\partial T}{\partial y} \right) + \dot{q} = 0 \quad (6.14)$$

$$\dot{q} = \dot{q}_p + \dot{q}_f \quad (6.15)$$

$$\dot{q}_p = \eta_p \bar{\sigma} \dot{\epsilon}^p \quad (6.16)$$

$$\dot{q}_f = \eta_f J \bar{\tau} \dot{\gamma} \quad (6.17)$$

where  $q_p$  is the heat generation rate due to plastic deformation,  $\eta_p$  the fraction of the inelastic heat,  $q_f$  is the volumetric heat flux due to frictional work,  $\dot{\gamma}$  the slip rate,  $\eta_f$  the frictional work conversion factor considered as 1.0,  $J$  the fraction of the thermal energy conducted into the chip, and  $\bar{\tau}$  is the frictional shear stress. The value of  $J$  may vary within a range, say, 0.35 to 1 for carbide cutting tool [Mabrouki & Rigal, 2006]. In the present work, 0.5 (default value in ABAQUS) has been taken for all the cases. The fraction of the heat generated due to plastic deformation remaining in the chip,  $\eta_p$ , is taken to be 0.9 [Mabrouki et al., 2004][26]

## 6.10 ABAQUS Platform

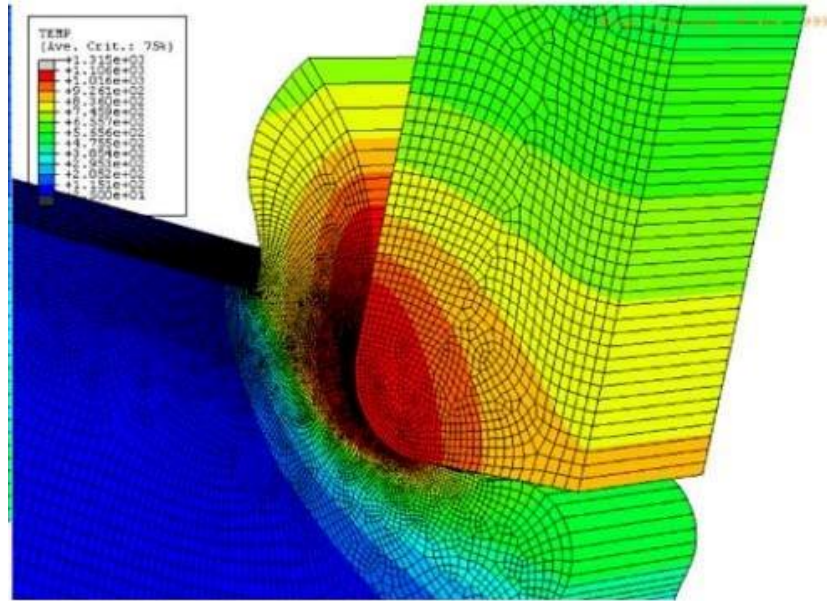
The type of software package chosen for the FE analysis of metal cutting process is equally important in determining the quality and scope of analysis that can be performed. There are currently large number of commercial software packages available for solving a wide range of engineering problems that might be static, dynamic, linear or non-linear. Some of the dominant general purpose FE software packages include ABAQUS, ANSYS, MSC/NASTRAN, SRDC- IDEAS, etc. It is obvious that different packages would possess different capabilities. This makes it critical to select the suitable software package with appropriate features required for performing a given analysis successfully. The present study selects ABAQUS as a platform to explore the capabilities of finite element method in analyzing various aspects of metal cutting process.

ABAQUS is known to be powerful general purpose FE software that can solve problems ranging from relatively simple linear analyses to the highly complex non-

linear simulations. This software does not have any separate module for machining as in the case of Deform or AdvantEdge. As a result, the user has to explicitly define the tool and the workpiece, process parameters, boundary conditions, mesh geometry and simulation controls. This may certainly require more skill, experienced user, effort and time to set up simulations as no preset controls and assumptions are available. But this is the feature that not only ensures very high level of details from modeling point of view but also a thorough analysis by allowing a precise control on boundary conditions, mesh attribute, element type, solver type and so on.

A complete ABAQUS program can be subdivided into three distinct modules, namely, ABAQUS/CAE, ABAQUS/Standard or ABAQUS/Explicit and ABAQUS/Viewer as shown in Fig. 3.8. These modules are linked with each other by input and output files. ABAQUS/Standard and ABAQUS/Explicit are the two main types of solvers that are available for performing analysis, ABAQUS/Explicit being mainly used for explicit dynamic analysis. It is said that the strength of ABAQUS program greatly lies in the capabilities of these two solvers. The model of the physical problem is created in the pre-processing stage, details of which such as discretized geometry, material data, boundary conditions, element type, analysis type and output request are contained in the input file. ABAQUS/CAE is divided into functional units called modules with the help of which the FE model can be created, input file can be generated and results can be extracted from the output file. Each module has been designed to serve a specific portion of the modeling task.





**Figure 6.8: Orthogonal metal cutting simulation by using Abaqus**  
(Source: Ozel, et al. 2007)

## **CHAPTER 7**

### **PRESENT MODEL AND SIMULATION OF METAL CUTTING**

#### **7.1 Introduction**

In previous chapters important parameters, and possible ways of modelling them in simulations of cutting, has been looked at through a literature study. In this chapter, details of modelling tool, work piece and cutting system are presented.

A finite element model of the machining process was developed from two-dimensional orthogonal analysis. Although two-dimensional analysis is a restrictive approach from practical point of view, it reduces the computational time considerably and provides satisfactory results regarding the details of the chip formation. A commercially available general purpose finite element package, ABAQUS/Explicit version 6.14 along with ALE technique was employed to conduct the simulation.

In the cutting operation, heat transfer largely depends on the cutting velocity. It is often assumed that at high cutting speeds, there is nearly no time for conduction to occur and adiabatic conditions may exist with high local temperatures in the chip. In the present work, firstly an adiabatic analysis was performed to obtain much clear shear bands on the chip surface. This helps in explaining the phenomena that leads to the formation of the saw-teeth chips. However, in real machining, ignoring the heat transfer is unacceptable and also it is not possible to determine the temperature field over the tool surface with adiabatic analysis module. This motivated to exploit the fully coupled temperature-displacement module of the Abaqus/Explicit. A very simple approach was followed to demonstrate the formation of both the continuous and segmented chip, namely in one case thermal conductivity of the workpiece was considered while in the other, it was neglected. Although neglecting the thermal conductivity makes the approach hypothetical to some extent, it aids in proper understanding of the chip segmentation process as seen in the case of adiabatic analysis as well as to understand the temperature field over the tool surface.

## 7.2 Tool Modelling

The 2 D FE model for the analysis of chip formation consists of a portion of the cutting tool and a block representing the workpiece. Since the cutting width is much larger than the undeformed chip thickness, plane strain condition was assumed. The cutting tool was assumed to be perfectly sharp. It is noted that width of the chip surface is the thickness of the material to be cut or the undeformed chip thickness which is actually equal to the feed in the orthogonal cutting conditions.

The geometric properties of the tool are given in Table 7.1

**Table 7.1: Geometric variables of the cutting tool**

Rake Angle, $\alpha$ (°)	Clearance Angle, $c$ (°)	Tip Radius, $r_T$ (mm)
-6	6	Sharp tip

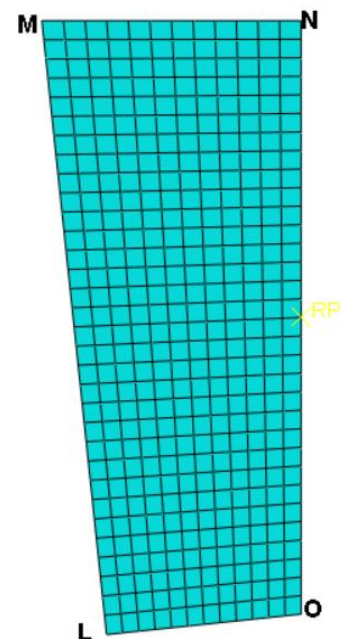
Tool material was selected tungsten carbide (WC). Thermal and mechanical properties of WC are given in Table 7.2

**Table 7.2: cutting tool properties (Ozel & Zeren, 2006)**

Material	$\rho$ (kg/m <sup>3</sup> )	E (GPa)	$\nu$	$C_p$ (J Kg <sup>-1</sup> K <sup>-1</sup> )	k (W m <sup>-1</sup> K <sup>-1</sup> )	$\alpha$ ( $\mu\text{m m}^{-1}$ K <sup>-1</sup> )
Carbide Tool	11900	534	.22	400	50	-

Finite element mesh of tool is modelled using 429 nodes and 384 elements. Isoparametric quadrilateral elements are used for the analysis. This design is shown in Figure 7.1

Four-node plane strain bilinear quadrilateral (CPE4RT) elements with reduced integration scheme and hourglass control are used for the discretization for the cutting tool.



**Figure 7.1: Cutting Tool Mesh**

### 7.3 Work piece Modelling

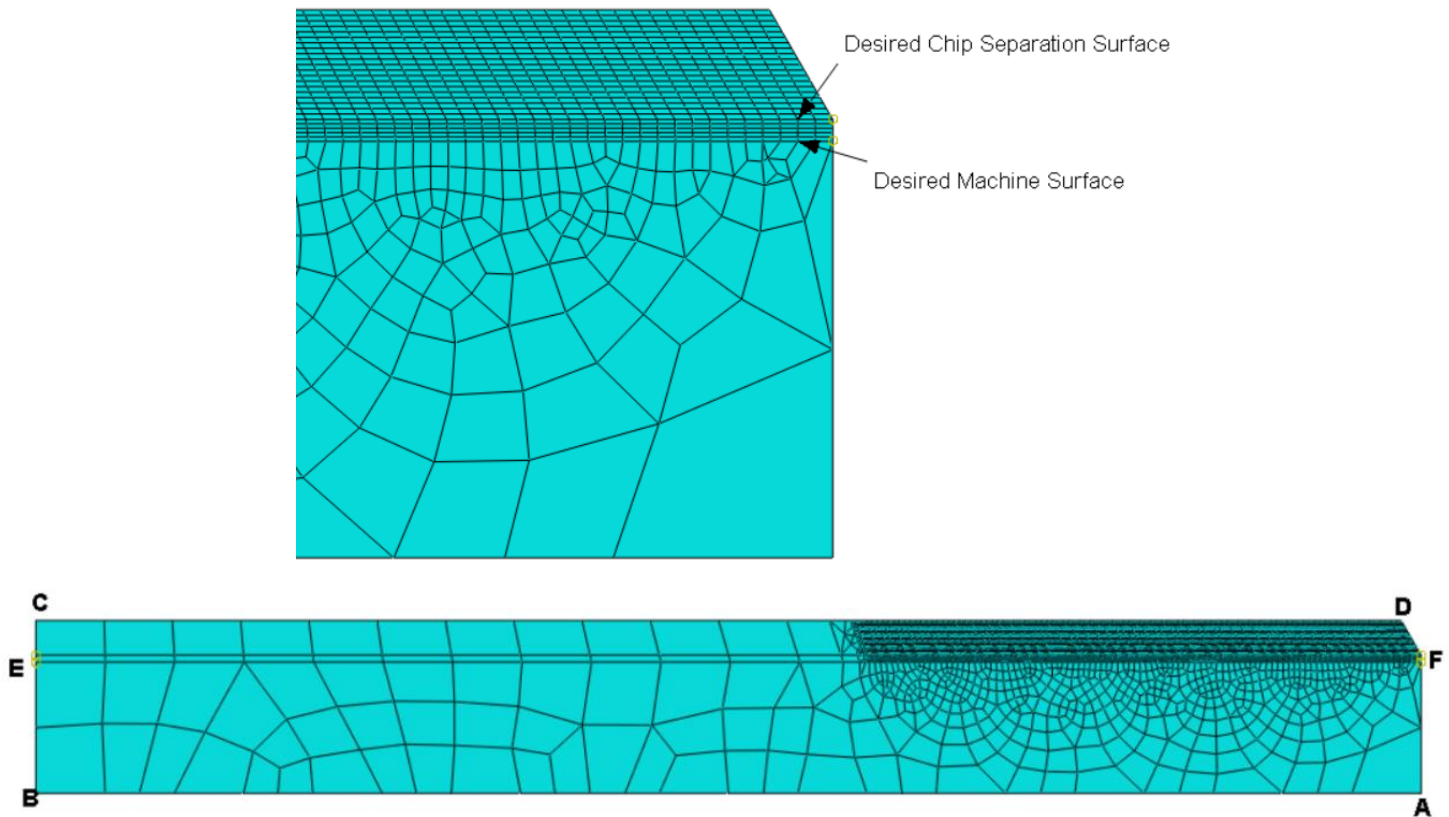
A chamfer was incorporated in the workpiece to form the initial chip without termination of program that may occur due to heavy distortion of elements at the starting part of the workpiece due to the negative rake of the cutting tool. Though in actual practice chamfer does not exist, it hardly matters in the simulation because the study is based on the steady state machining conditions.

An intermediate layer of elements known as damage zone has been considered in the workpiece block that defines the path of separation of chip from the workpiece material which is going to take place as the tool progresses. It is noted that width of the chip surface is the thickness of the material to be cut or the undeformed chip thickness which is actually equal to the feed in the orthogonal cutting conditions. Details of the geometric model and the working parameters have been shown in Figure 7.2 and Table 7.3, respectively.

**Table 7.3: Details of the geometric model and cutting parameters**

Description	Parameter	Values
Workpiece model geometry	Length (mm)	8
	Width (mm)	1
	Damage Zone Width (mm)	.04
Cutting Parameter	Feed, f (mm)	0.1, <b>0.2</b> , 0.3
	Cutting Velocity, V (m/min)	60, <b>100</b> , 180

The Figure 7.2 shows the desired chip separation surface and desired machined surface separated by a narrow line of sacrificial layer of elements called damage zone, width of which has been mentioned as  $\epsilon$ . It is noted that in reality these two surfaces should be same but such assumption has been taken only for the modeling purpose as a chip separation criterion where in  $\epsilon \rightarrow 0$ . Consequently, a very small value of  $\epsilon$  (0.04 mm) which is computationally acceptable has been taken as the width of the damage zone. The choice of the height of the designated damage zone is purely based on computational efficiency. It could be reduced further if faster



**Figure 7.2: Geometric Details and Mesh of Workpiece**

computing facilities are available. The material model is defined for the entire workpiece while the damage model is defined specifically in the damage zone such that when the accumulated damage in an element in the sacrificial layer immediately ahead of the tool exceeds one, the element is supposed to fail. It is then removed from the mesh and consequently the tool moves further into the workpiece.

The physical properties of the AISI 4340 workpiece such as, density ( $\rho$ ), Elastic modulus ( $E$ ), Poisson's ratio ( $\nu$ ), specific heat ( $C_p$ ), thermal conductivity ( $k$ ) and thermal expansion coefficient ( $\alpha$ ) are mentioned in Table 7.4 (Ozel & Zeren, 2006).

**Table 7.4: Workpiece properties (Ozel & Zeren, 2006)**

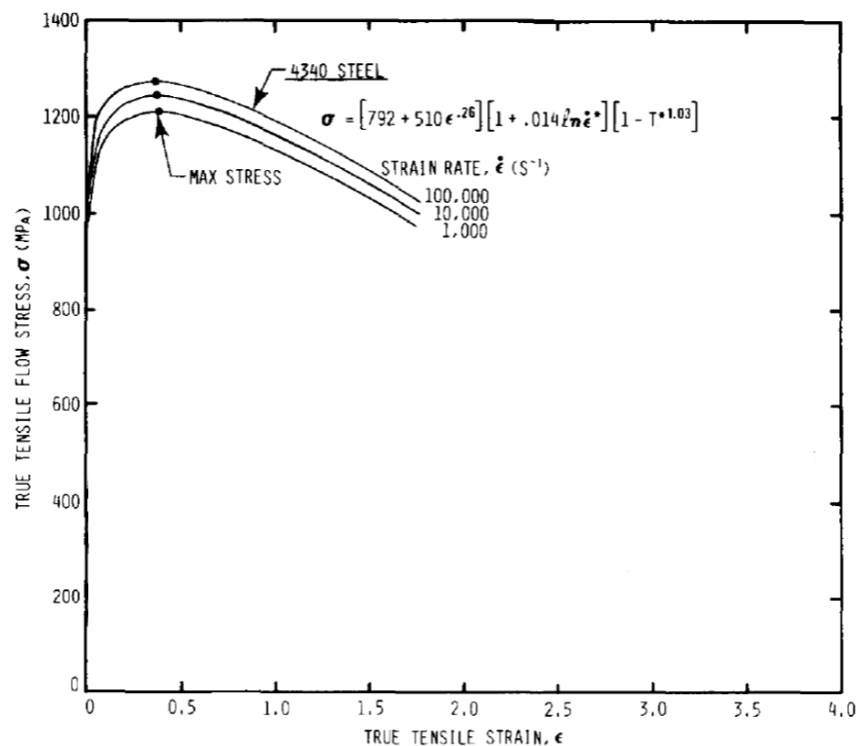
<b>Material</b>	<b><math>\rho</math> (kg/m<sup>3</sup>)</b>	<b>E (GPa)</b>	<b><math>\nu</math></b>	<b><math>C_p</math> (J Kg<sup>-1</sup> K<sup>-1</sup>)</b>	<b>k (W m<sup>-1</sup> K<sup>-1</sup>)</b>	<b><math>\alpha</math> (<math>\mu\text{m m}^{-1}</math> K<sup>-1</sup>)</b>
AISI 4340	7850	205	.30	475	44.5	13.7

Flow stress modelling of work piece material is very important to achieve satisfactory results from metal cutting simulation. In the analysis, AISI 4340 is selected as work piece material. Johnson-Cook material constitutive model is used to model the plastic behaviour of AISI 4340.

Material coefficients listed in Table 7.5 is used in calculating Johnson-Cook flow stress values-

**Table 7.5: Johnson-Cook parameters for AISI 4340  
(Johnson & Cook, 1983; Johnson & Cook, 1985)**

A (MPa)	B (MPa)	n	C	m	D <sub>1</sub>	D <sub>2</sub>	D <sub>3</sub>	D <sub>4</sub>	D <sub>5</sub>
792	510	.26	.014	1.03	.05	3.44	-2.12	.002	.61



**Figure 7.3: Adiabatic Stress-Strain relationship for AISI 4340**

Finite element mesh of work piece is modelled using 3209 nodes and 3139 isoparametric quadrilateral elements. The work piece is created at least 20 feeds long and 10 feeds high therefore the predicted results are not sensitive to the displacement boundary conditions and steady state can be reached. Mesh of

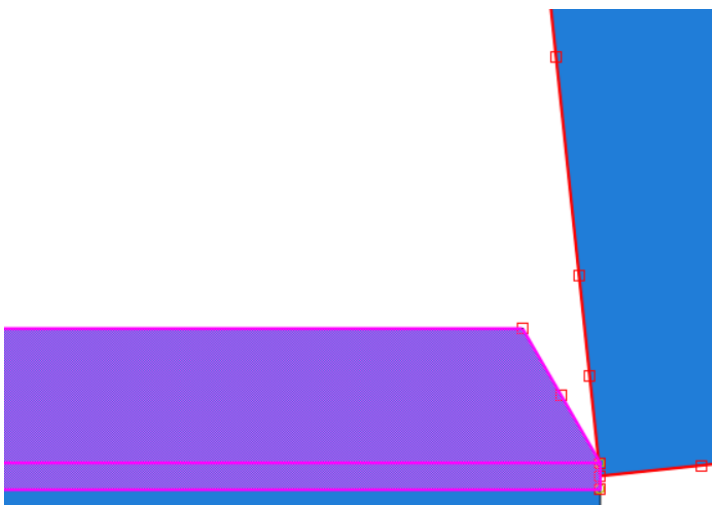
deformation zone is modelled very dense as shown in Figure 7.2. in order to reduce calculation time and obtain more accurate results.

## 7.4 System Modelling

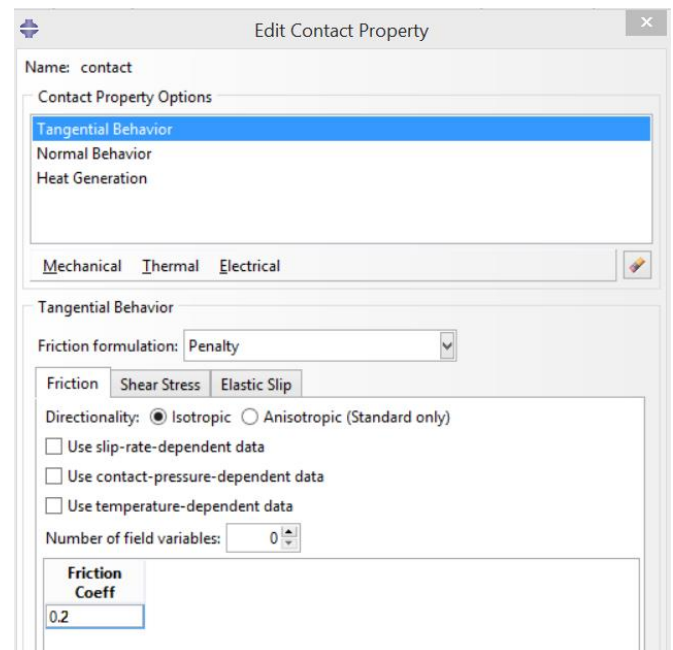
After modelling metal cutting components one by one, the next step is to assembly them due to cutting conditions.

### 7.4.1 Interfacial contact and friction

The contact between the workpiece and the tool is a penalty based hard contact in the normal direction where the tool is defined as the master surface and the workpiece is defined as the slave surface. This means that the surface of the workpiece is not allowed to penetrate the tool at any point, but that the opposite might occur if the mesh of the slave surface is too coarse Both the frictional forces and the friction-generated heat are included in the kinematic contact algorithm through TANGENTIAL BEHAVIOUR and GAP HEAT GENERATION modules of the software.



**Figure 7.4: Tool-Chip Surface-Node Interaction**



**Figure 7.5: Contact Property in Abaqus**

In the tangential direction a Coulomb friction model, with friction coefficient 0.2, has been used.

## 7.4.2 Boundary Conditions

### 7.4.2.1 Displacement Boundary Conditions

For the simulation of cutting operation, proper type of boundary conditions should be imposed. The kinematic boundary conditions are as follows:

For the workpiece:

$$u_y = 0 \text{ on AB, } u_x = 0 \text{ on BC, } v_x = V_c \text{ on ABEF}$$

where  $v_x$  is the velocity in X-direction,  $V_c$  is the cutting velocity, and AB, BC and ABEF refer to edges in Figure 7.2

The tool is supported by fixing the nodes on the boundary M-N-O in both x and y direction, refer Figure 7.1

### 7.4.2.2 Thermal Boundary Condition

In case of adiabatic analysis, no heat transfer is allowed from the top surface of the workpiece, exposed surface of the chip and the machined surface to the cutting tool and to the atmosphere. While for the coupled temperature displacement analysis, boundaries CDF and LM in Figure 7.1 and Figure 7.2 have convective heat transfer boundary conditions, with the overall heat transfer coefficient ( $h$ ), thermal conductivity ( $k$ ) and ambient temperature ( $T_o$ ) given as input:

$$-k \frac{\partial T}{\partial n} = h(T_o - T) \quad (7.1)$$

Rest of the surfaces for both tool and work piece were initially kept at ( $T_o$ ). It is noted that the heat transfer coefficient  $h$ , being the ratio of average heat flow across the interface to the temperature drop, is a function of several variables such as, contact pressure, temperature, contacting materials, etc. Due to difficulties in



measuring temperatures at tool-chip interface, there is hardly any data available for heat transfer coefficient for chip formation process. In the present work, simulations at a particular speed-feed combination were done for  $h$  varying within a range of 100-1000 kW/m<sup>2</sup> K. Since the difference in temperature was found to be very less with the change in heat transfer coefficient,  $h = 500$  kW/m<sup>2</sup> K was considered as a fair compromise. Moreover, this value has also been used by Coelho (2006) for machining AISI 4340 and thus, taken as the reference value for the entire set of simulations.

## **CHAPTER 8**

### **RESULTS AND DISCUSSION**

The type of chip formed affects the stress field generated in the workpiece which determines the residual stresses, cutting temperatures and cutting forces. Therefore, simulating the right kind of chip is essential for the proper analysis of the metal cutting process. This necessitates that FE simulations have the capability to develop both continuous and segmented chips. The present work considers the machining of AISI 4340 with a negative rake carbide tool. Experimental studies available in the literature show that segmented chips are produced for such type of tool-workpiece combination, specifically at higher cutting speeds. Thus, the goal of this work is to develop a finite element model that not only simulates the saw-tooth chips but also explains the mechanism governing it.

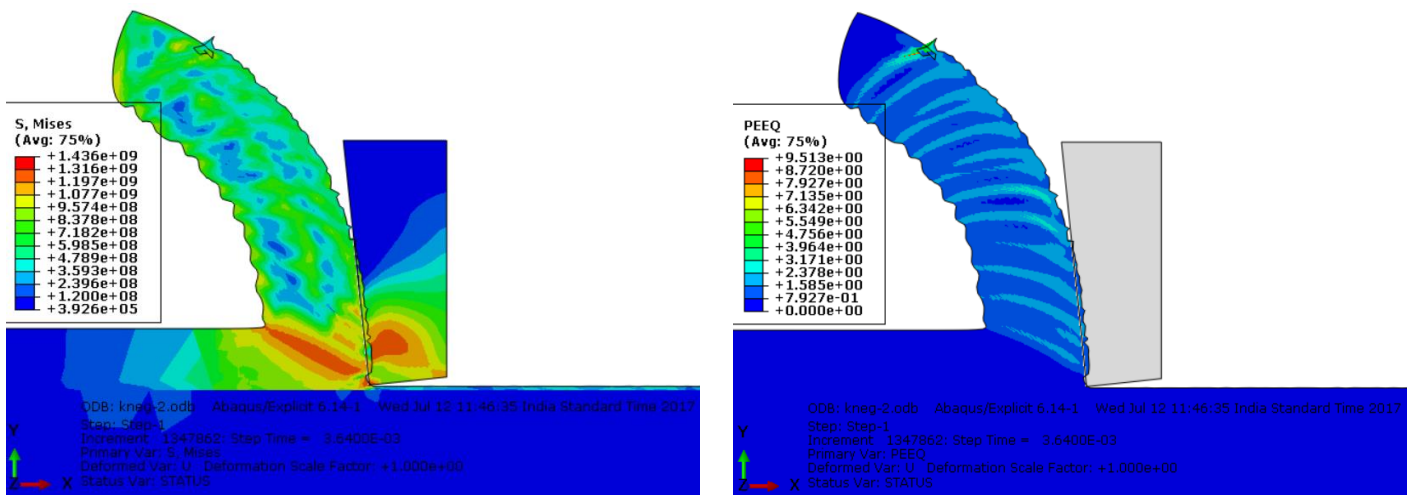
In this section, results dealing with von Mises equivalent stresses, equivalent strains, temperatures and machining forces during adiabatic analysis are presented showing the efficiency of this module to explain the chip formation phenomenon. But, in order to obtain more realistic results, fully coupled temperature displacement analysis was performed by considering the thermal conductivity of the workpiece in one case while neglecting it in the other case. Incorporating such variation in the given module shows the strong dependence of the chip morphology on thermal conductivity. Numerical results dealing with both the cases are presented and compared. The cutting force, thrust force and other related parameters were determined at different cutting speeds for each of the cases in coupled analysis. Feed values and cutting speeds are also varied for the chip formation in adiabatic analysis. Simulated results are then compared with each other as well as with the results available in the literature; thus, proving the validity of the developed FE model. The comparative study of the continuous and the segmented chips developed demonstrates the critical importance of modeling the correct type of chip.

## 8.1 Finite element modelling based on adiabatic analysis

As already mentioned, there is very less time for the heat conduction to occur at higher cutting speeds during machining and thus adiabatic hypothesis can possibly be imposed for the modeling of the chip formation process.

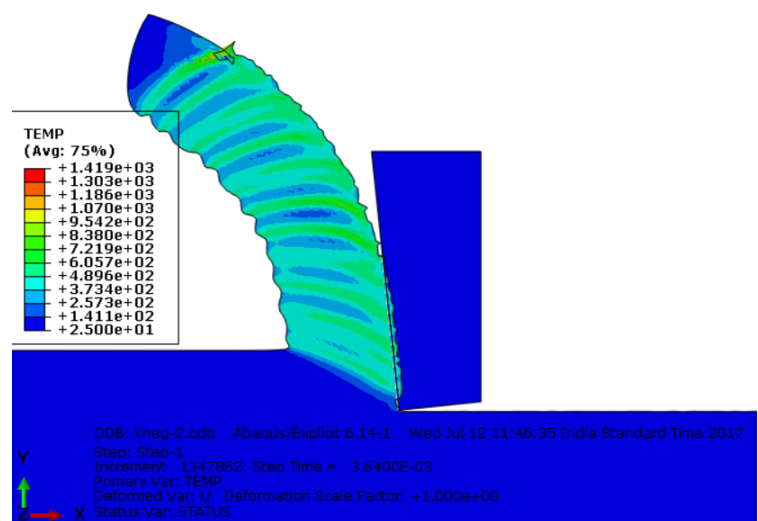
### 8.1.1 Chip morphology and its mechanism

Saw teeth or segmented chips are produced under adiabatic conditions with cutting parameters set at  $V_c = 100$  m/min and  $f = 0.2$  mm . The chip segmentation is the result of a softening state at elevated temperatures during tool-workpiece interaction. Figure 8.1 and Figure 8.2 are presented that help in explaining the mentioned phenomenon elaborately, (onset at about 3.64 ms)



**Figure 8.1: Von-mises stress and strain contours for segmented chip**

Chip formation begins with the bulging of the workpiece material in front of the tool. It can be seen that the stresses with the higher values are mainly distributed in the primary shear deformation zone, values ranging between 1.19–1.31 GPa, followed by the secondary shear deformation zone. At a particular instant, the stress along the primary shear zone becomes so high that it

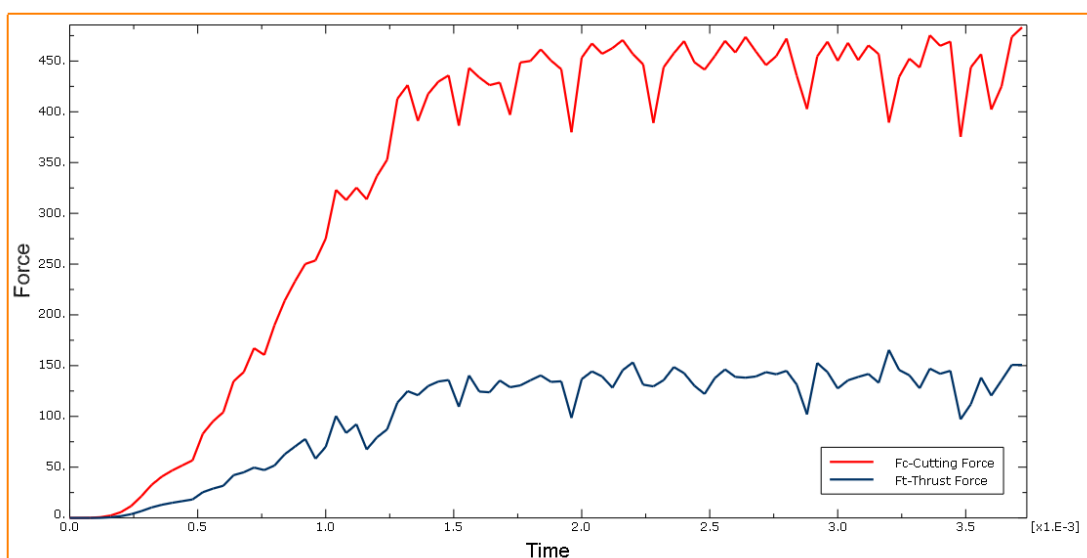


**Figure 8.2: Temperature Distribution**

causes higher strains, ranging from 2–2.5 as shown in Figure 8.1 and results in material damage. This causes a plastic deformation and localized heating. Consequently, rapid increase in temperature occurs near the tool tip that extends towards the chip free side causing the shear bands, known as the adiabatic shear bandings, to form. From the Figure 8.2. It is noted that the temperature in the primary shear deformation zone becomes as high as 600–700°C which continues to increase as we move towards the chip free side. This induces thermal softening on the back of the chip and decreases the chip thickness. Such high temperatures in the valleys of the saw tooth profile were also reported by Ng and Aspinwall (Ng et al., 1999). Then the repeated occurrence of bulging and the shear banding results in waved irregularities on the chip back in the form of saw-teeth.

Temperature rises gradually at the time of bulging of the chip but increases rapidly once the shear banding begins to form. Accordingly, regions of low and high temperatures occur alternately thus, giving a stripped pattern of temperature distribution as illustrated in Figure 8.2. As the cutting continues, because of the bulging of the chip the chip thickness gradually increases and so also the cutting forces. But the chip thickness decreases suddenly due to rapid increase of temperature and subsequent thermal softening.

Figure 8.3 shows the cutting force ( $F_c$ ) and thrust force ( $F_t$ ) developed during the process.



**Figure 8.3: Variation of Cutting Force and Thrust Force**

The segmented chip produced in the present case closely matches with the experimental results of Lima et al. (2005) [49], found under equivalent cutting conditions i.e.,  $V_c = 100$  m/min and  $f = 0.2$  mm. However, the predicted cutting forces are found to be underestimated when compared with the experimental values of Lima et al. (2005), with the deviation 10% .

### 8.1.2 Variation of feed and cutting speed

In order to validate the developed model, feed (uncut chip thickness) is varied over a range of 0.1–0.3 mm and its effect on the cutting and thrust forces are studied and compared with the existing results. Figure 8.4 shows the effect of feed rate on the turning forces  $F_c$  and  $F_t$  when cutting AISI 4340 steel at  $V_c = 100$  m/min. The cutting force and thrust force, as expected, increase almost linearly with increasing feed rate (Lima et al., 2005); thus confirming the results obtained by the present model.

Similarly, cutting speed was varied over a range of 60–180 m/min during the formation of the segmented chip by using adiabatic analysis and its effect on the cutting force and thrust force is shown in the Figure 8.5

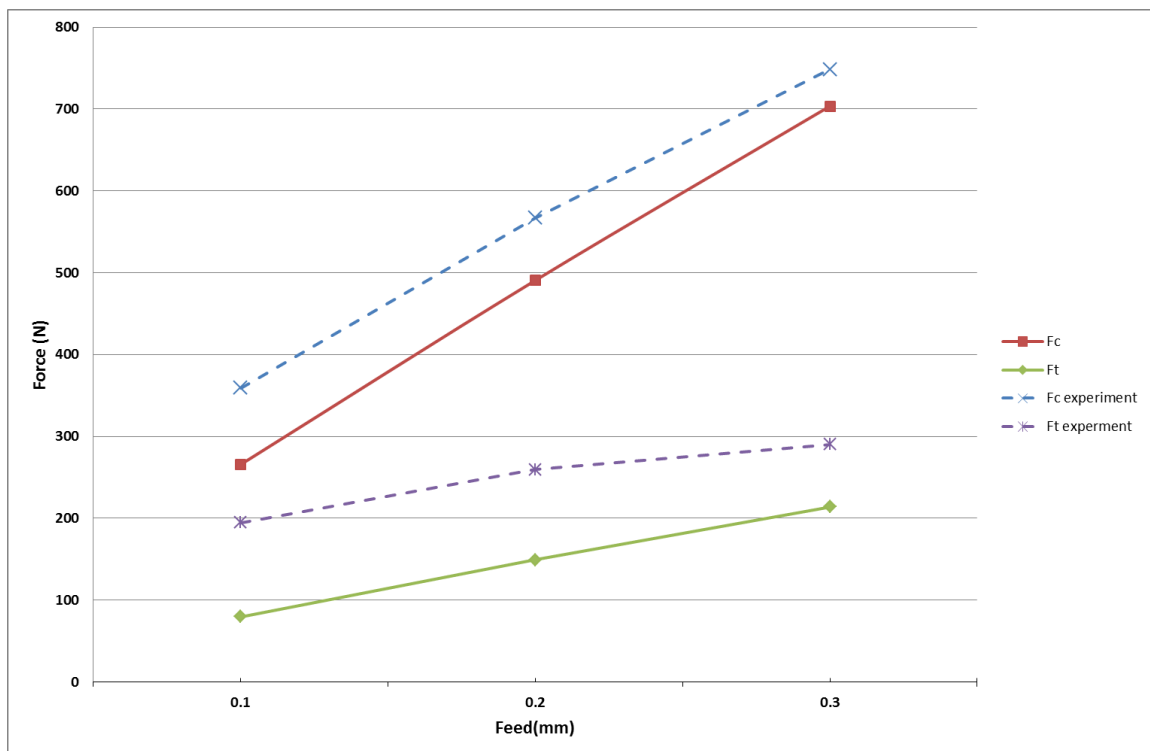
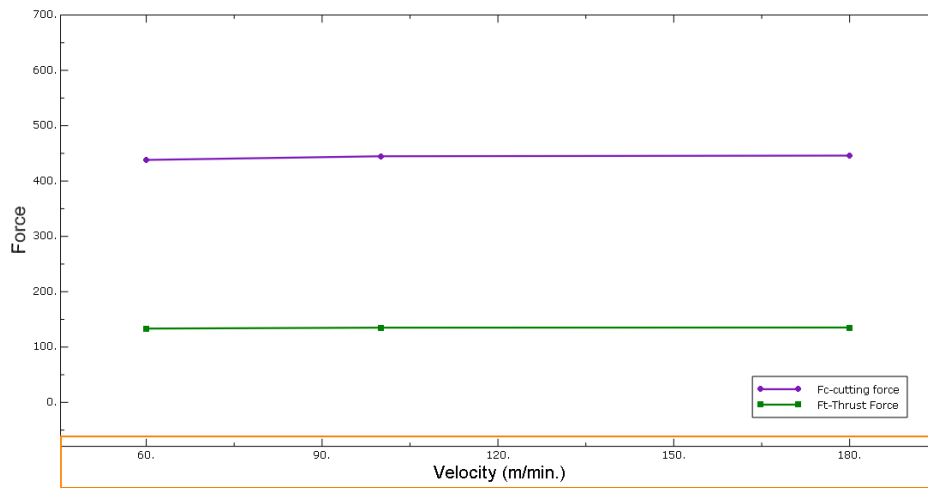


Figure 8.4: Effect of Feed on Fc and Ft



**Figure 8.5: Effect of cutting velocity on Fc and Ft**

It is observed that cutting force and thrust force remained almost constant over the varying cutting speeds. Similar observations were reported by Mabrouki et al. (2008) while simulating the segmented chips, considering adiabatic hypothesis, for machining of aluminium alloy.

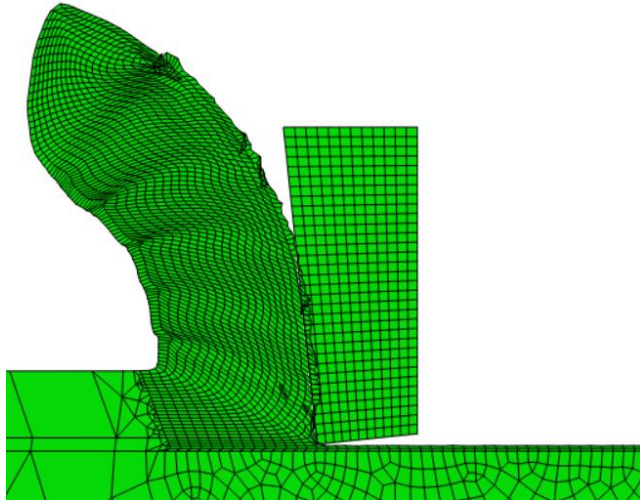
## **8.2 Finite element modeling based on fully coupled temperature-displacement analysis**

Adiabatic conditions in metal cutting, no doubt, make the study of chip formation simpler but are not completely acceptable as far as real machining conditions are considered. Thus, coupled temperature displacement analysis is considered that not only provides a more practical approach for the simulation of chip formation but also determines the temperature field on the tool surface. This information is very useful in the study of tool wear progress.

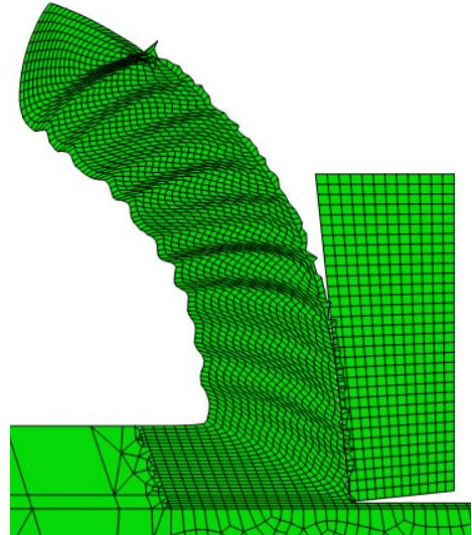
To demonstrate the ability of the model to simulate both continuous and segmented chips, thermal conductivity of the workpiece is considered in one case while neglected in the other case. The cutting speed was varied in both the cases and its effect on the cutting force was studied. This parametric study, in one way, helps in validating the developed models.

### **8.2.1 Chip morphology**

When the thermal conductivity of the workpiece material was considered in the coupled temperature displacement analysis, continuous chips were obtained in contrast to the previous section where segmented chips, were produced under the



**Figure 8.6: Deformed continuous chip mesh**



**Figure 8.7: Deformed Segmented chip mesh**

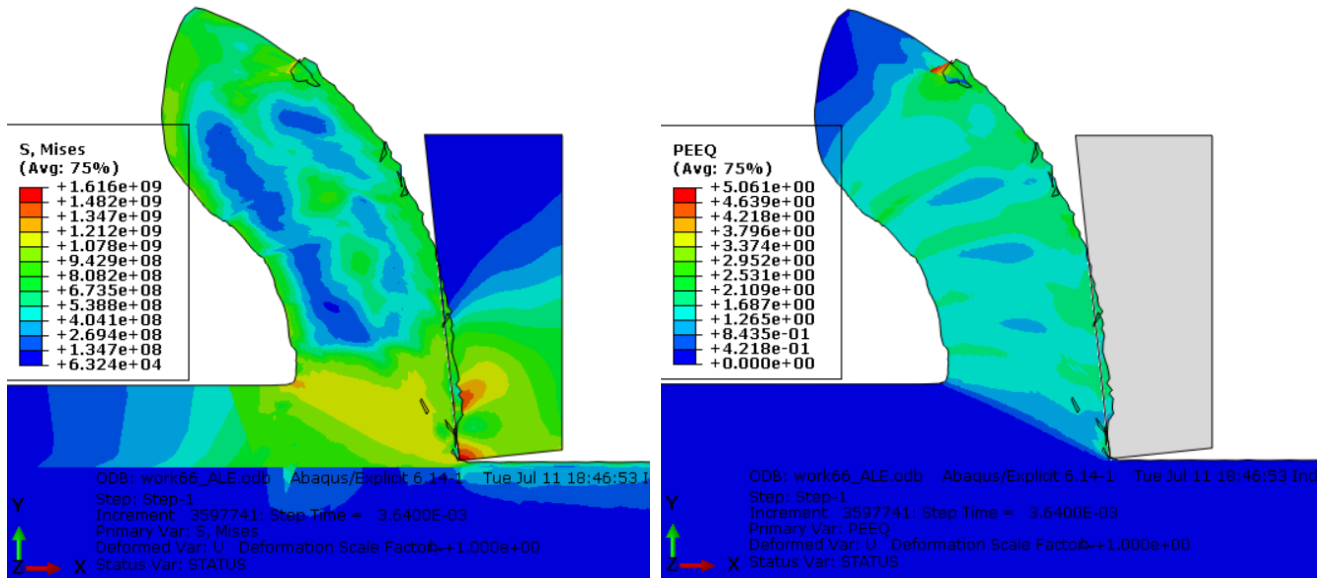
same cutting conditions. Figure 8.6 shows the deformed finite element mesh for the continuous chip formation.

Since adiabatic conditions allow maximum amount of heat to be retained on the chip surface, adiabatic shearing was very prominent; thus reproducing saw-teeth due to thermal softening on the back of the chip. While, in the case of coupled temperature analysis with thermal conductivity of the workpiece defined, heat conduction occurred and the heat generated due to plastic deformation was not confined to the primary shear deformation zone only. This produced uniform and continuous chips. On one hand, adiabatic hypothesis plays a vital role in simulating the segmented chips while on the other hand, these are unacceptable in real machining. Therefore, to simulate the correct type of chip in a more realistic manner, the simplest way is to combine the relevant features of both the approaches, i.e. to incorporate the adiabatic boundary conditions in the coupled temperature displacement analysis. It is possible by neglecting the thermal conductivity of the workpiece that allows the localized heating due to plastic deformation to extend from the tool tip towards the chip free side. This induces thermal softening and consequently, the saw tooth profile on the back of the chip. Figure 8.7 shows the

deformed finite element mesh for the segmented chip formation by neglecting the thermal conductivity of the workpiece.

Figure 8.8 and Figure 8.9 clearly depict the variation in distribution of equivalent von Mises stresses, equivalent strain and the temperature over the chip surface when the chip morphology changes.

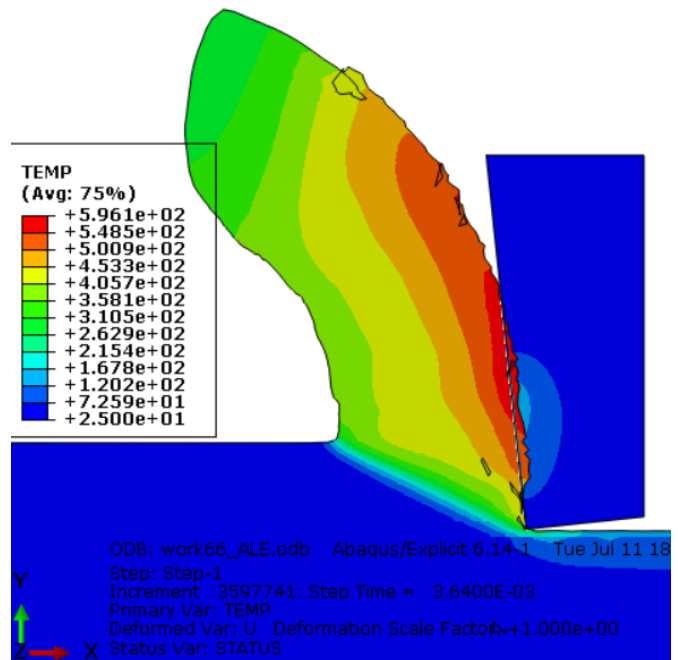
From Figure 8.9 and Figure 8.1, it is observed that the levels of stresses for both



**Figure 8.9: Von-mises stress and strain contours for continuous chip**

the cases were similar but the distribution pattern of the stresses varied significantly for continuous and segmented chips. In the segmented chips highly localized stresses

were found in the shear zone with values in the range of 1.19–1.24 GPa; same as those found in the case of adiabatic analysis. While in continuous chips the stresses are distributed over a wider region over the chip surface. Similar comparisons were reported by Ng and Aspinwall (1999) and Wu and Matsumoto (1990), thus confirming the results obtained.



**Figure 8.8: Temperature Distribution**

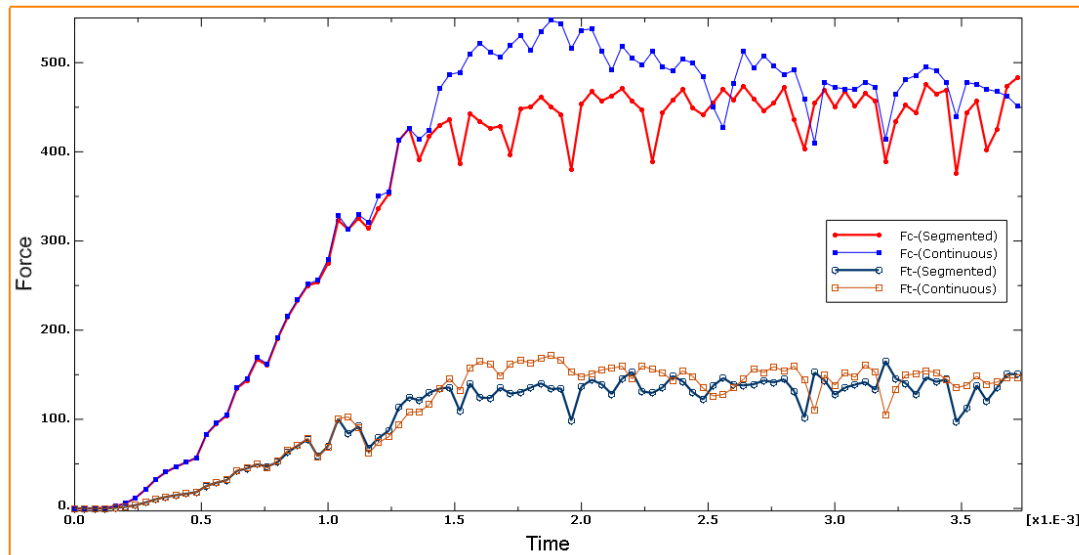


Figure 8.8 and Figure 8.2 show that the distribution of temperature over the chip surface, again, differs considerably in both the cases. The shear zone temperature for continuous chip was found to be lower, in the range of 250–300°C as compared to the segmented chips. Highest temperatures were observed along the tool-chip interface for the continuous chips, specifically in the sliding zone of the rake surface, the value corresponding to 550–600°C. As one moves from the tool tip towards the chip free surface, temperature decreases to 400°C. Shih (1996) found the location of maximum temperature in the same region while simulating the continuous chip formation.

## 8.2.2 Cutting forces

Figure 8.10 show the evolution of the forces  $F_c$  and  $F_t$  for cutting velocity 100 m/min. and feed 0.2 mm over time and Figure 8.11 show distribution of the normal stress  $\sigma_n$  and frictional stress  $\tau$  on the rake surface for both continuous and segmented chip formation, respectively.

The force signature shows that the cutting force corresponds to the type of chip produced in the



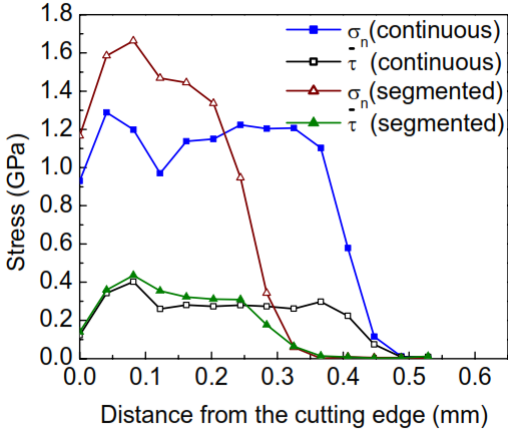
**Figure 8.10: Evolution of  $F_c$  and  $F_t$  for continuous and Segmented chip**

cutting process. During continuous chip formation, the cutting force did not show much fluctuation. Whereas, in the case of segmented chip formation, cutting force fluctuates due to change in the deformed chip thickness and thus, shows prominent depletion and accumulation of stresses.

It is also noted that the formation of continuous chips exhibited higher value of cutting force. Since the thermal conductivity of the workpiece material was negligible in the case of segmented chips, the material deformed more easily leading to lower value of cutting force. Baker (2003) [50] also found that cutting force is the largest for the case of no segmentation and degree of segmentation decreases as the conductivity is increased.

As already mentioned, bending of the chip was also highly prominent when the thermal conductivity of the workpiece was neglected. As a consequence, the tool chip contact length decreased. This is much clear in the Figure 8.11 which shows the normal stress and frictional stress distribution on the rake surface for continuous as well as segmented chip formation.

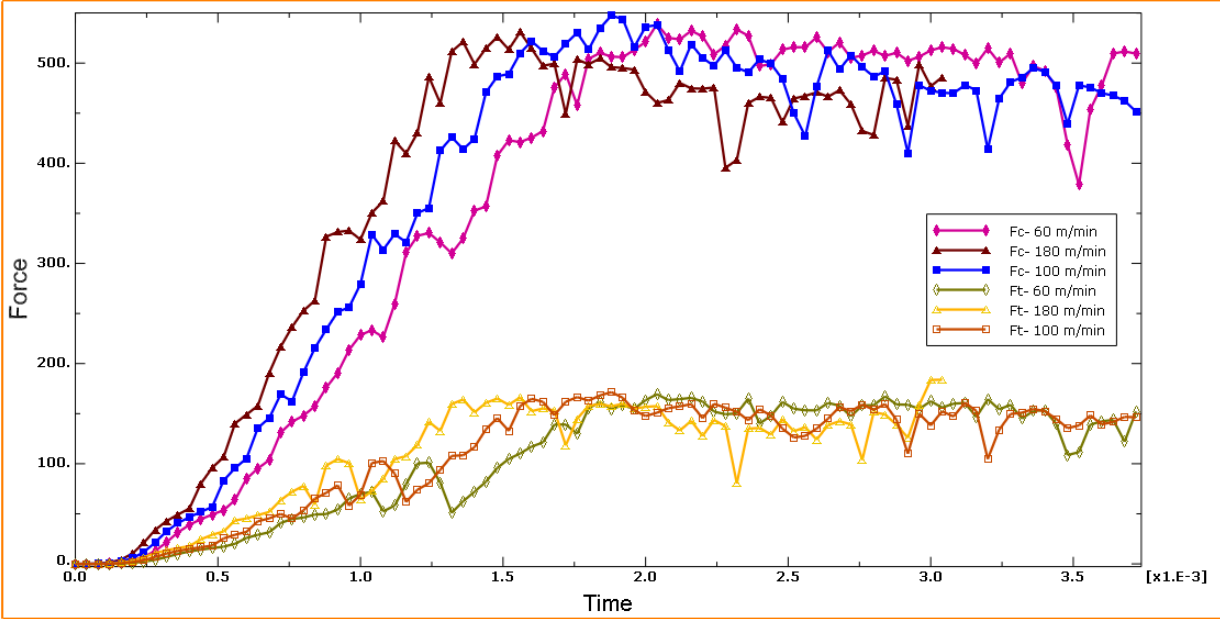
It is observed that the normal stress reaches its maximum value at a short distance away from the tool tip because no load acts at this location as the element gets deleted. Then gradually the normal stress decreases to zero at the point where the chip leaves the rake surface; thus indicating the tool-chip contact length (Shi et al., 2002) [51]. Since tool chip contact length is smaller for segmented chips, cutting force is lower. Besides, cutting forces are also known to vary with the deformed chip thickness. Thus, this can be attributed to the higher value of cutting force in continuous chip formation because a larger deformed chip thickness was observed with continuous chips.



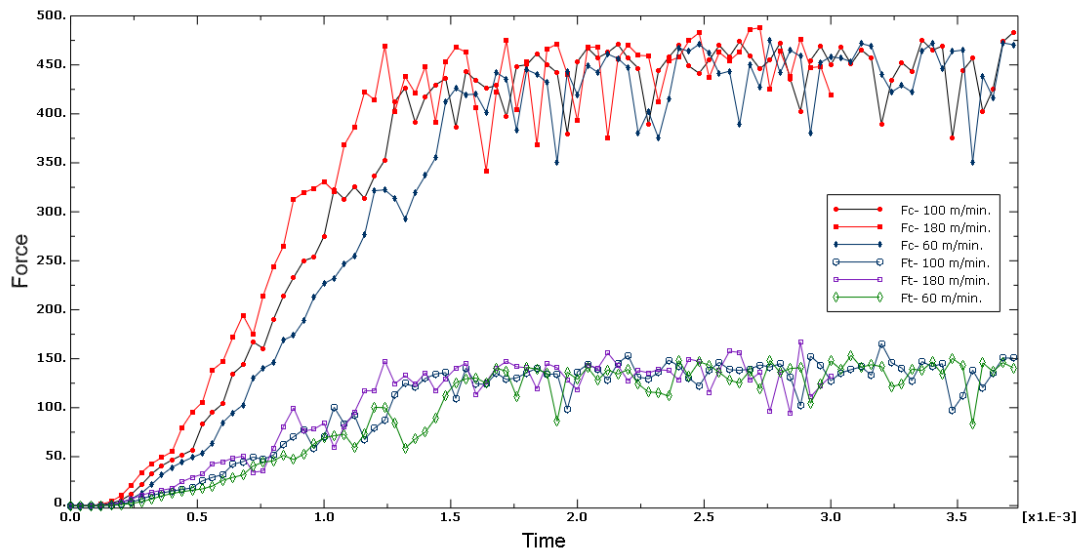
**Figure 8.11: Distribution of  $\sigma$  and  $\tau$  on rake surface**

**8.2.3 Variation of cutting speed & Feed**

The cutting speed was varied over a range of 60–180 m/min at a feed of 0.2 mm for both continuous and segmented chip formation. Figure 8.12 and Figure 8.13 show the variation of  $F_c$  and  $F_t$  at different cutting velocities for continuous chips and segmented chips, respectively. It is known that as the cutting velocity increases the cutting force and thrust force decrease.



**Figure 8.12: Variation of  $F_c$  and  $F_t$  for continuous chip at different cutting velocity**



**Figure 8.13: Variation of Fc and Ft for segmented chip at different cutting velocity**

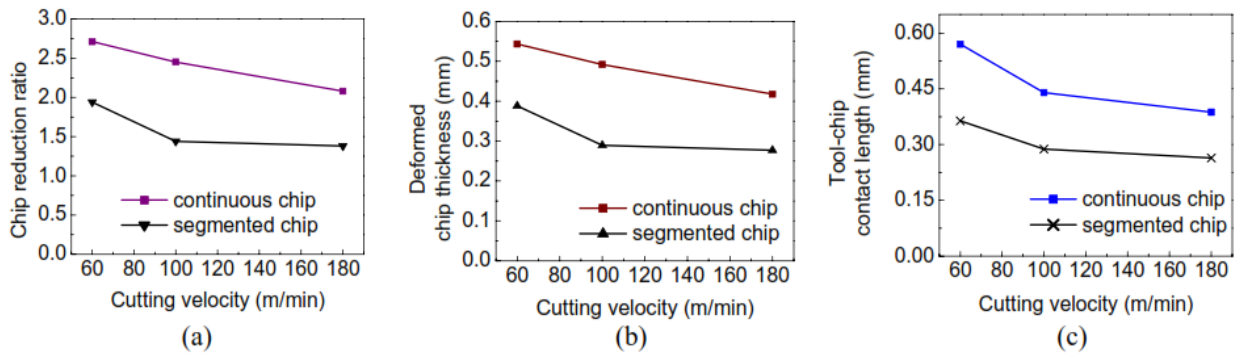
As the cutting velocity increases, temperature of the shear zone increases. This causes softening of the work piece, which means the value of  $\tau_s$  decreases and thereby reduces the value of cutting and thrust force as shown in Figure 8.13. In Figure 8.12, it is observed that cutting force reduced by 11% as the cutting velocity is varied from 60 m/min to 180 m/min. However, not much reduction is observed in the thrust forces.

From Figure 8.13, adiabatic hypothesis considered by neglecting the thermal conductivity of the workpiece. When the thermal conductivity is neglected, it possibly does not take into account the softening of the workpiece material which actually occurs near the tool tip due to increased temperature at high cutting speeds.

As the cutting velocity increases, the shear zone shrinks and results in the increase of shear angle  $\phi$ , which in turn decreases the chip reduction ratio,  $\zeta$  (which is ratio of deformed chip thickness  $t_c$  to undeformed chip thickness  $t$ ). Consequently the deformed chip thickness decreases as shown in Figure 8.14(b).

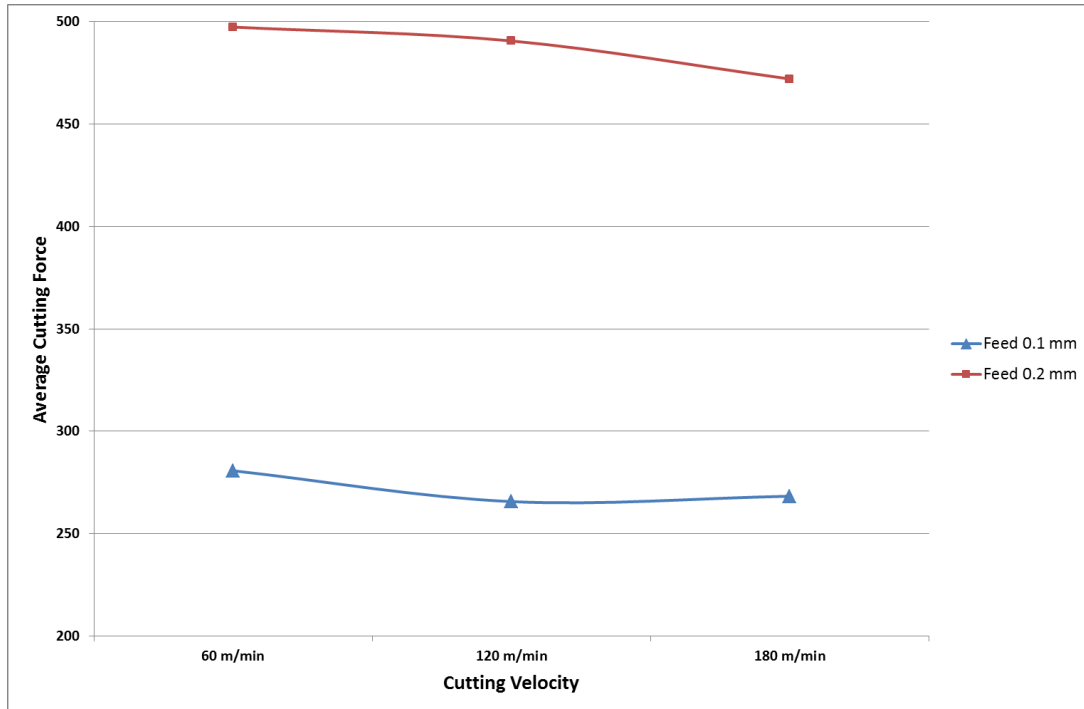
The tool-chip contact length ( $L_n$ ) which in turn affects the cutting force considerably, also changes with variable cutting speed. Figure 8.14(c) shows effect of cutting velocity on tool-chip contact length for both continuous and segmented chip formation.

Chip reduction coefficient, deformed chip thickness and tool-chip contact length showed fairly constant value at higher cutting speeds during the formation of segmented chip formation as observed in the case of forces.



**Figure 8.14: Variation of (a) chip reduction ratio (b) deformed chip thickness and (c) tool-chip contact length with cutting velocity for continuous and segmented chip formation**

Below is Figure 8.15 of variation of cutting force  $F_c$  over different cutting velocity when feed is increased from 0.1 mm to 0.2 mm.



**Figure 8.15: Variation of cutting force over feed and speed**

### 8.2.4 Effects of Coefficient of friction

In Figure 8.16 can be seen that as the value of coefficient of friction increases, the cutting force also increases because of increased resistance due to friction along the tool- chip interface. It can be concluded from the Figure 8.17 that with the increase in the value of coefficient of friction, increase temperature in shear zone is observed .

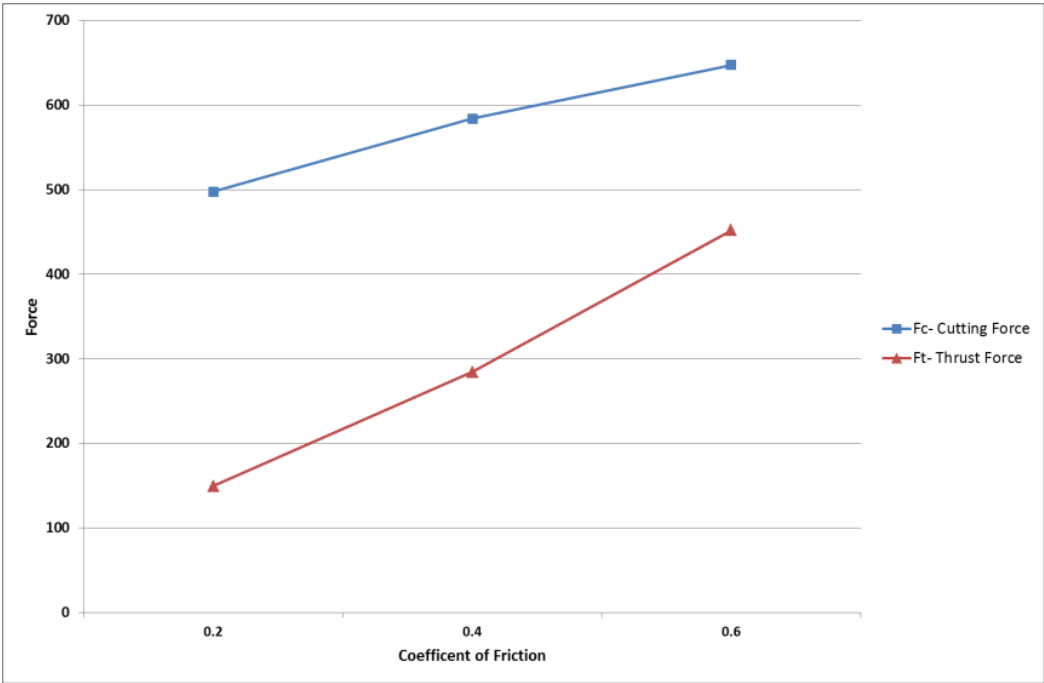


Figure 8.16: Effect of coefficient of friction on Average cutting force

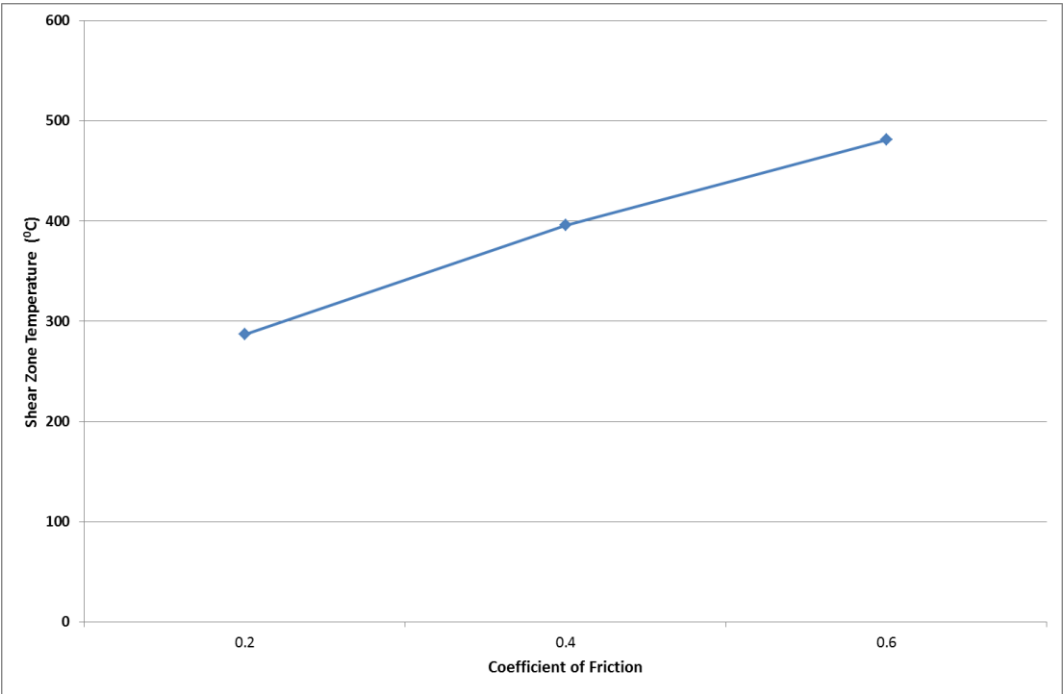


Figure 8.17: Effect of coefficient of friction on shear zone temperature

### 8.3 Comparison of Cutting Force with Experimental Data:

Here cutting force  $F_c$  is compared with the experimental data obtained by Lima et al. (2005) [49] with same cutting conditions.

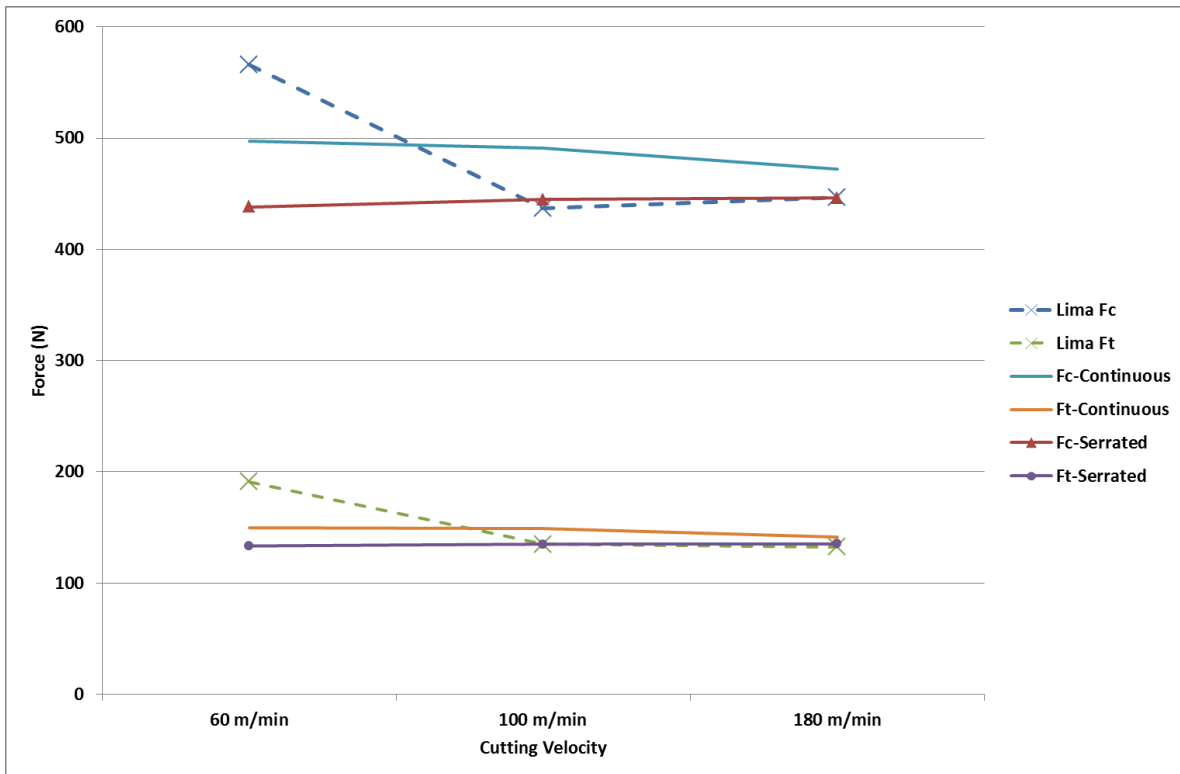
Below Table 8.1 shows the  $F_c$  comparison when cutting speed varies at 60 m/min, 100 m/min, 180 m/min at fixed feed 0.2 mm

**Table 8.1: Cutting force comparison with experimental data at different velocity**

<b>Cutting Velocity m/min.</b>	<b><math>F_c</math> (ABAQUS)</b>	<b><math>F_c</math> (Experiment)</b>	<b> Error  %</b>
60	497.383082	565.66	12.07
100	490.6262727	436.87	12.30
180	472.0714722	446.29	5.77

### 8.4 Verification of simulated results

Verification of FE model is the final and mandatory stage of the FEM authentication in metal cutting. As far as the authenticity of the present model is concerned, predicted results are compared with the experimental results presented by Lima et al. (2005) for machining AISI 4340 using carbide cutting tool ( $\alpha = -6^\circ$ ) under similar cutting conditions. Figure 8.18 shows the deviation between experimental values (Lima et al., 2005) of cutting force and the thrust force with that of the predicted values, as deduced from the simulation of continuous and segmented chip formation. It is found that the simulated results lie well within the acceptable range. In case of continuous chip formation, the cutting force and thrust values closely match with that of the experimental ones, with largest deviation not more than 12-13% observed for low cutting speed (60 m/min). It is interesting to note that predicted results, for both continuous and segmented chip formation, showed maximum deviation at the lowest cutting speed, while in higher cutting speeds the values are closer to the experimental ones.



**Figure 8.18: Comparison of predicted forces during simulation of continuous and segmented chip formation with experimental forces**

## 8.5 Discussion

The present work shows that stress, strain and temperature fields are greatly affected by the chip formation process. Since the goal is to focus on the segmented chip formation, adiabatic analysis module of ABAQUS/Explicit was used at the beginning. Well-defined adiabatic shear bandings are observed in this case as no heat conduction is allowed during the machining process. When feed rate was varied, the cutting force and thrust force increased, as expected. On the other hand, when the cutting speed was varied, the forces remained almost constant. This emphasizes that ignoring the heat conduction completely is impractical, though it produces prominent saw tooth chips based on adiabatic shearing. Hence, coupled temperature displacement analysis was employed to make the study more realistic. In this study, an attempt was made to simulate both continuous and segmented chip formation.

Continuous chips were produced when thermal conductivity of the workpiece was defined in the coupled temperature displacement analysis. During continuous chip formation, stress fields are not as localized in primary shear zone as observed in the case of segmented chip. As a consequence,



highest equivalent strains and temperature levels are not found in this region, but in the secondary shear deformation zone. The chip which is entering into the secondary shear deformation zone already possesses accumulated plastic strain and heat. The instant it begins to flow over the rake surface, further plastic straining and local heating occurs because of severe contact and friction in the contact zone (Shi et al., 2002) [51]. Therefore, the maximum equivalent plastic strain and temperature are found along the tool-chip interface, specifically in the sliding region. Though the desired chip morphology could not be predicted with this module, the cutting forces were found to match closely with the experimental ones. This motivated to combine the adiabatic hypothesis, as considered in adiabatic analysis (predicting desired chip morphology) with the coupled temperature-displacement analysis (predicting forces satisfactorily). Hence, the thermal conductivity of the workpiece was simply neglected in the coupled analysis to cater to the present need of generating segmented chips. In this case, maximum values of temperature are observed in the secondary shear zone due to high straining along the tool-chip interface as well as at the back of the chip in a highly localized region that induces thermal softening causing the desired saw tooth profile.

It is known that type of chip produced depend upon the type of cutting tool and workpiece materials, cutting conditions and so on. Chip morphology is an important index in the study of machining because it affects the stress field generated in the workpiece which determines the residual stresses, the cutting temperatures and the cutting force.

Determination of the cutting forces facilitate estimation of power consumption which is required for the design of machine-fixtured-tool system, evaluation of role of various machining conditions and condition monitoring of the cutting tools. The variation in the cutting force has been shown to be related to the chip morphology. A smoother time signature of the cutting force indicates continuous chip formation with good surface finish whereas wavy time signature of the cutting force indicates segmented chip formation. Obviously, magnitude of the waviness (difference between the peak and lower values) relates to surface finish quality. It is also important to consider the regularity of the waviness which indicates the intervals (time interval correlates to space interval at known cutting conditions) at which residual stresses are released.

Moreover, the knowledge of the cutting temperature gives idea about the tool wear progress, residual stresses and the surface finish of the machined surface. It is, thus, clear that

controlling these variables can lead to higher productivity and accuracy which in case of metal cutting leads to higher tool life and better surface finish. The stresses, strains, temperatures and many other outputs that are obtained from FE simulations greatly help in understanding the basic mechanism of chip formation under different cutting conditions. Note that various aspects of metal cutting like, cutting tool design, optimization of cutting parameters for higher tool life and good surface finish, prediction of tool wear growth, etc. are achievable only when we are able to comprehend the underlying physics of the chip formation process correctly by simulating right kind of chip morphology under different cutting conditions.

## **CHAPTER 9**

### **CONCLUSIONS AND FUTURE WORK**

#### **9.1 Conclusions**

A 2D plane strain FE model has been developed by using simulation software ABAQUS/Explicit with appropriate material and damage models. Numerical results showed that adiabatic hypothesis plays a crucial role in the formation of segmented chips due to adiabatic shearing. Adiabatic analysis module proved useful in explaining formation of adiabatic shear banding that consequently lead to thermal softening and thus the formation of saw-tooth chips during machining of AISI 4340 steel. In coupled temperature displacement analysis, simulation of continuous and segmented chip formation was demonstrated successfully. Thermal conductivity of the workpiece was neglected to satisfy the adiabatic hypothesis for simulating the formation of segmented chip. Highest temperature levels were observed only along the tool-chip interface during continuous chip formation. But during the formation of segmented chip formation, temperatures closer to tool-chip interface temperature were found in highly localized regions at the back of the chip. Such variations in temperatures are attributed to the corresponding variation in the stress and strain fields. Prediction of right kind of chip morphology is important as it affects the stress field generated in the workpiece which determines the residual stresses, the cutting temperatures and the cutting force. It has been shown that there exists a correlation between the type of chip produced and the time signature of the cutting force. Knowledge of the cutting forces are useful in estimation of power consumption which is required for the design of machine-fixtured-tool system, evaluation of role of various machining conditions and condition monitoring of the cutting tools.

It is found that the predicted forces for segmented chips by neglecting the thermal conductivity are underestimated when compared with the experimental values (Lima et al., 2005) [49] and the simulated values for continuous chip formation. This approach can still be considered as a fair compromise because it not only simulates the desired segmented chips and but also, predicts the cutting force and thrust values with maximum deviation not exceeding 20%. Moreover, the difference between the predicted and the experimental values are prominent in low cutting speed. It is observed that as the cutting speed increases the deviation in the predicted values

gradually decrease. This can be attributed to the fact that at higher cutting speeds adiabatic hypothesis satisfies well whereas at lower cutting speeds the assumption shows inadequacy.

## 9.2 Future Works

There are three principal pillars of realistic metal cutting modeling. They are a proper model of the work material behavior (resistance) in cutting (currently known as the chip formation model), a model that governs the contact process at the tool–chip interface, and a model of physical resource of the cutting wedge. In opinion, future modeling of metal cutting should be directed in the development of these models which constitutes the model of metal cutting.

There may be some future investigations-

- All of the simulations were performed assuming a sharp cutting edge of the tool. However in practice no such sharp edge exists, as even a brand new tool has a small tip radius which may increase the cutting and radial forces, alter plastic deformation, and change the chip deformation pattern particularly in small cutting feeds. To include this tool feature in the analysis, other FE modeling techniques may be used to avoid computational instability due to excessive element distortions caused by tool features such as tool tip radius. Mesh controls and adaptive meshing algorithms may overcome these difficulties. Additionally, other finite element techniques such as Arbitrary Lagrangian–Eulerian (ALE) formulation combined with the proposed physical model may be worth investigations.
- Among these computational difficulties is handling the chip separation, element deletion is the most common approach used to simulate crack propagation and material separation. However, in metal cutting other methods may improve the prediction of such cracks taking into consideration the compressive stress nature in the primary deformation zone, possibly causing the creation of unrealistic voids due to the deletion of elements, which can lead to collapse and cause analysis failure.
- A material model with a more correct implementation of the kinematic hardening, containing strain rate effects and temperatures, could be tried in order to see whether there would be any improvements in the result in relation to simulations with the ordinary Johnson-Cook material model.
- There can be investigation on tool life and the tool wear.

- In this work, however uncoated carbide tool is used. But there can be user a coated carbide tool.
- There can be checked the results when rake angle is varied.
- However in this work no user subroutine is used for chip segmentation. But a new ductile failure criterion may be incorporated into the user subroutine (UMAT) to simulate the shear-localized chip formation

## REFERENCES

- [1.] Van Luttervelt, C.A., Childs, T.H.C., Jawahir, I.S., and Klocke, F., "Modeling of machining operations," *Annals CIRP* 47 (1998) 587-626.
- [2.] Zienkiewicz, O.C., "The finite element method in engineering science," McGraw- Hill, London (1971).
- [3.] Childs, T.H.C., Maekawa, K., Obikawa, T., and Yamane, Y., "Metal Machining Theory and Applications" Arnold, London, (2000).
- [4.] Iwata, K., Osakada, K., and Terasaka, Y., "Process modeling of orthogonal cutting by the rigid-plastic finite element method," *Journal of Engineering Materials Technology* 106 (1984) 132-138.
- [5.] Strenkowski, J. and Carroll, J., "A finite element model of orthogonal metal cutting," *Journal of Engineering for Industry* 107 (1985) 347-354.
- [6.] Marusich, T. and Ortiz, M., "Modelling and simulation of high speed machining," *International Journal for Numerical Methods in Engineering* 38 (1995) 3675-94.
- [7.] Ceretti, E., Lucchi, M., and Altan, T., "FEM simulation of orthogonal cutting: serrated chip formation," *Journal of Materials Processing Technology* 95 (1999) 17-26
- [8.] Hahn, R.S.: On the temperature developed at the shear plane in the metal cutting process. In: *Proceedings of First U.S. National Congress Appl. Mech.* ASME 661 (1951)
- [9.] Chao, B.T., Trigger, K.J.: An analytical evaluation of metal cutting temperature. *Trans. ASME* 73, 57–68 (1951)
- [10.] Leone, W.C.: Distribution of shear-zone heat in metal cutting. *Trans. ASME* 76, 121–125 (1954)
- [11.] Loewen, E.G., Shaw, M.C.: On the analysis of cutting tool temperatures. *Transactions of the ASME* 71, 217–231 (1954)
- [12.] Weiner, J.H.: Shear plane temperature distribution in orthogonal machining. *Trans. ASME* 77, 1331–1341 (1955)
- [13.] Rapier, A.C.: A theoretical investigation of the temperature distribution in the metal cutting process. *Br. J. Appl. Phys.* 5, 400–405 (1954)
- [14.] ASM Handbook, Volume 16-Machining, ASM International Handbook Committee, ASM International, Electronic (1989) ISBN: 978-1-61503-145-0

- [15.] Dan Wedberg. *Modelling of High Strain Rate Plasticity and Metal Cutting*. PhD thesis, Luleå University of Technology, 2013.
- [16.] Xue Bin Liu, Xi Bin Wang, Chong Ning Li, and San Peng Deng. Finite Element Simulation of the Orthogonal Cutting Based on Abaqus. *Advanced Materials Research*, 821-822:1410–1413, September 2013.
- [17.] P.J. Arrazola, A. Villar, D. Ugarte, and S. Marya. Serrated chip prediction in Finite Element modeling of the chip formation process. *Machining Science and Technology*, (11):37–41, April 2014.
- [18.] Metal Cut diag by Emesee licensed under CC BY 3.0. [http://en.wikipedia.org/wiki/Image:Metal\\_Cut\\_diag.jpg](http://en.wikipedia.org/wiki/Image:Metal_Cut_diag.jpg).
- [19.] Juneja, B.L., Sekhon, G.S., Seth, N.: Fundamentals of metal cutting and machine tools, 2nd edn. New Age International Publishers, New Delhi (2003)
- [20.] Merchant, M.E.: Mechanics of the metal cutting process. *J. Appl. Phys.* 16, 318–324 (1945)
- [21.] Lee, E.H., Shaffer, B.W.: The theory of plasticity applied to a problem of machining. *Trans. ASME, J. Appl. Mech.* 18, 405–413 (1951)
- [22.] Oxley, P.L.B.: Shear angle solutions in orthogonal machining. *Int. J. Mach. Tool.Des. Res.* 2, 219–229 (1962)
- [23.] Groover, M.P.: Fundamentals of modern manufacturing: materials processes, and systems, 2nd edn. Wiley, India (2002)
- [24.] Lacale, L.N., Guttierrez, A., Llorente, J.I., Sanchez, J.A., Aboniga, J.: Using high pressure coolant in the drilling and turning of low machinability alloys. *Int. J. of Adv. Tech.* 16, 85–91 (2000)
- [25.] Tobias, S.A.: Machine tool Vibration. Blackie and Sons Ltd, Scotland (1965)
- [26.] Mabrouki, T., Deshayes, L., Ivester, R., Regal, J. -F. & Jurrens, K. (2004). Material modeling and experimental study of serrated chip morphology. *Proceedings of 7th CIRP International Workshop on Model. Machin, France April 4-5*
- [27.] M. Vaz, D. R. J. Owen, V. Kalhori, M. Lundblad, and L.-E. Lindgren. Modelling and Simulation of Machining Processes. *Archives of Computational Methods in Engineering*, 14(2):173–204, June 2007.
- [28.] T.L. Anderson. Fracture Mechanics: Fundamentals and Applications, Second Edition. CRC Press- INC, 1995.

- [29.] H. Tada, P.C. Paris, and G.R. Irwin. The stress analysis of cracks handbook: by Hiroshi Tada, with the cooperation of Paul C. Paris and George R. Irwin. Paris Productions & (Del Research Corp.),1985
- [30.] I.N. Sneddon. The distribution of stress in the neighbourhood of a crack in a elastic solid. Proceedings, Royal Society of London, A-187:229–260, 1946
- [31.] F. Beer and E. Johnston, *Mechanics of Materials*. 2nd Ed., New York, NY: McGraw-Hill, 1992
- [32.] G. Sih, “A Review of the Three-dimensional Stress Problem for a Cracked Plate,” *International Journal of Fracture Mechanics*, vol. 7.1, 1971
- [33.] Bakker, “Three Dimensional Constraint Effects on Stress Intensity Distributions in Plate Geometries with Through-thickness Cracks,” *Fatigue & Fracture of Engineering Materials & Structures*, vol. 15.11, pp. 1051-1069, 1992
- [34.] T. Nakamura and D. Parks, “Three-dimensional Crack Front Fields in a Thin Ductile Plate,” *Journal of the Mechanics and Physics of solids*, vol. 38.6, pp. 787, 812, 1990.
- [35.] ABAQUS® ver. 6.14, complete set of online documentation, DS SIMULIA, USA (2016)
- [36.] <http://www-materials.eng.cam.ac.uk>
- [37.] A.A. Griffith. The Phenomena of Rupture and Flow in Solids. Philosophical transactions Royal Society of London. 1920
- [38.] C. F. Shih, B. Moran, and T. Nakamura. Energy release rate along a three-dimensional crack front in a thermally stressed body. *International Journal of Fracture*, 30:79–102, 1986
- [39.] D. M. Barnett and R. J. Asaro. The fracture mechanics of slit-like cracks in anisotropic elastic media. *Journal of the Mechanics and Physics of Solids*, 20:353–366, 1972
- [40.] Z. Suo. Singularities, interfaces and cracks in dissimilar anisotropic media. *Proceedings of the Royal Society, London*, 427:331–358, 1990
- [41.] J.E. Shigley, C.R. Mischke, R.G. Budynas *Mechanical Engineering Design*, 7th Ed. pp 161-166, McGraw Hill, 2004.
- [42.] A.W.A. Konter, *Advanced Finite Element Contact Benchmarks*, Netherlands Institute for Metals Research, July 2005
- [43.] Zhong, Z. H., “Finite Element Procedures for Contact Impact Problems”, Oxford University Press, New York. 1993



- [44.] Joanne Proudian. Simulating Residual Stress in Machining; From Post Process Measurement to Pre-Process Predictions. M.Sc. thesis, Royal Institute of Technology. 2012.
- [45.] Ozel, T. 2006. The Influence of Friction Models On Finite Element Simulations of Machining. *International Journal of Tools and Manufacturing* 46: 518-530
- [46.] Wu, H.-C.: Continuum Mechanics and Plasticity. Chapman and Hall/CRC (2004)
- [47.] [Johnson, G.R., Cook, W.H.: A constitutive model and data for metals subjected to large strains, high strain rates and high temperatures. In: Proceedings of 7th Int Symp Ballistics, the Hague, The Netherlands, pp. 541–547 \(1983\)](#)
- [48.] Mamalis, A.G., Horvath, M., Branis, A.S. and Manolakos, D.E. 2001. Finite Element Simulation of Chip Formation in Orthogonal Metal Cutting. *Journal of Materials and Processing Technology* 110: 19-27.
- [49.] Lima, J. G., Avila, R. F., Abrao, A. M., Faustino, M. & Davim, J. P. (2005). Hard turning: AISI 4340 high strength alloy steel and AISI D2 cold work tool steel. *Journal of Materials Processing Technology*, 169, 388-395
- [50.] Baker, M. (2003). An investigation of the chip segmentation process using finite elements. *Technische Mechanik*, 23, 1-9
- [51.] Shi, G., Deng, X. & Shet, C. (2002). A finite element study of the effect of friction in orthogonal metal cutting. *Finite Elements in Analysis and Design*, 38, 863-883

## APPENDIX

Below are the some important Input File Code, which are generated when job is submitted.

### [1.] For Hertz Contact Analysis:

```
*Heading
** Job name: hertz Model name: Model-1
** Generated by: Abaqus/CAE 6.14-1
*Preprint, echo=NO, model=NO, history=NO, contact=NO
** PARTS
*Part, name=Part-1
*Node
*Nset, nset=_PickedSet2, internal, generate
  1, 1284,  1
*Elset, elset=_PickedSet2, internal, generate
  1, 1199,  1
** Section: Section-2
*Solid Section, elset=_PickedSet2, material=punch
1.,
*End Part
*Part, name=Part-2
*Node
*Element, type=CPE4R
*Nset, nset=_PickedSet3, internal, generate
  1, 11608,  1
*Elset, elset=_PickedSet3, internal, generate
  1, 11400,  1
** Section: Section-1
*Solid Section, elset=_PickedSet3, material=founfd
1.,
*End Part
** ASSEMBLY
*Assembly, name=Assembly
```

```

*Instance, name=Part-1-1, part=Part-1
*End Instance
*Instance, name=Part-2-1, part=Part-2
    0.,    -200.,    0.
*End Instance
*Nset, nset=_PickedSet8, internal, instance=Part-1-1
4,
** MATERIALS
*Material, name=founfd
*Elastic
70000., 0.3
*Material, name=punch
*Elastic
210000., 0.3
** INTERACTION PROPERTIES
*Surface Interaction, name=IntProp-1
1.,
*Friction
0.,
*Surface Behavior, pressure-overclosure=HARD
** BOUNDARY CONDITIONS
** Name: BC-1 Type: Symmetry/Antisymmetry/Encastre
*Boundary
_PickedSet9, ENCASTRE
** Name: BC-2 Type: Displacement/Rotation
*Boundary
_PickedSet10, 1, 1
_PickedSet10, 6, 6
** Name: BC-3 Type: Displacement/Rotation
*Boundary
_PickedSet11, 1, 1
_PickedSet11, 6, 6
** INTERACTIONS

```

```
** Interaction: Int-1
*Contact Pair, interaction=IntProp-1, small sliding, type=SURFACE TO SURFACE
_PickedSurf7, _PickedSurf14
** STEP: Step-1
*Step, name=Step-1, ngeom=NO, inc=1000
*Static
0.01, 1., 1e-05, 0.01
** LOADS
** Name: Load-1  Type: Concentrated force
*Cload
_PickedSet8, 2, -17500.
** OUTPUT REQUESTS
*Restart, write, number interval=1, time marks=NO
** FIELD OUTPUT: F-Output-1
*Output, field, number interval=100, time marks=NO
*Node Output
CF, RF, U
*Element Output, directions=YES
LE, NFORC, PE, PEEQ, PEMAG, S
*Contact Output
CFORCE, CNAREA, CSTRESS
** HISTORY OUTPUT: H-Output-1
*Output, history, variable=PRESELECT
*End Step
```

[2.] **For Orthogonal metal cutting simulation [Feed =0.2, velocity=100 m/min]**

```
*Heading
** Job name: work66_ALE Model name: Model-1
** Generated by: Abaqus/CAE 6.14-1
**Preprint, echo=NO, model=NO, history=NO, contact=NO
**
** PARTS
**
*Part, name=tool_rake_-6
*Node
*Element, type=CPE4RT
*Nset, nset=tool_rake_-6-RefPt_, internal
430,
** Section: Section-1
*Solid Section, elset=_PickedSet4, controls=EC-1, material=tool
1.,
*End Part
*Part, name=workpiece
*Solid Section, elset=_PickedSet36, controls=EC-2, material=workpiece-damage
1.,
** Region: (Section-2:Picked), (Controls:EC-2)
** ASSEMBLY
*Assembly, name=Assembly
*Instance, name=tool_rake_-6-1, part=tool_rake_-6
    0.0105,    0.00152,    0.
*End Instance
*Instance, name=workpiece-1, part=workpiece
    0.0008,    0.,    0.
*End Instance
*Nset, nset=tool_rf, instance=tool_rake_-6-1
```

1, 34, 67, 100, 133, 166, 199, 232, 265, 298, 331, 364, 397, 398, 399, 400  
 401, 402, 403, 404, 405, 406, 407, 408, 409, 410, 411, 412, 413, 414, 415, 416  
 417, 418, 419, 420, 421, 422, 423, 424, 425, 426, 427, 428, 429  
 \*Surface, type=ELEMENT, name=\_PickedSurf10, internal  
 \_\_PickedSurf10\_S1, S1  
 \_\_PickedSurf10\_S2, S2  
 \*End Assembly  
 \*\* ELEMENT CONTROLS  
 \*Section Controls, name=EC-1, hourglass=ENHANCED  
 1., 1., 1.  
 \*Section Controls, name=EC-2, DISTORTION CONTROL=NO, hourglass=RELAX  
 STIFFNESS  
 1., 1., 1.  
 \*Amplitude, name=Amp-1, definition=SMOOTH STEP  
 0., 0., 0.004, 1.  
 \*\* MATERIALS  
 \*Material, name=tool  
 \*Conductivity  
 50.,  
 \*Density  
 11900.,  
 \*Elastic  
 5.34e+11, 0.22  
 \*Specific Heat  
 400.,  
 \*Material, name=workpiece  
 \*Conductivity  
 44.5,  
 \*Density  
 7850.,

\*Elastic  
2.05e+11, 0.3

\*Expansion  
1.37e-05,

\*Inelastic Heat Fraction  
0.9,

\*Plastic, hardening=JOHNSON COOK  
7.92e+08, 5.1e+08, 0.26, 1.03, 1520., 25.

\*Rate Dependent, type=JOHNSON COOK  
0.014,1.

\*Specific Heat  
475.,

\*Material, name=workpiece-damage

\*Conductivity  
44.5,

\*Damage Initiation, criterion=JOHNSON COOK  
0.05, 3.44, -2.12, 0.002, 0.61, 1520., 25., 1.

\*Damage Evolution, type=ENERGY  
11097.6,

\*Density  
7850.,

\*Elastic  
2.05e+11, 0.3

\*Expansion  
1.37e-05,

\*Inelastic Heat Fraction  
0.9,

\*Plastic, hardening=JOHNSON COOK  
7.92e+08, 5.1e+08, 0.26, 1.03, 1520., 25.

\*Rate Dependent, type=JOHNSON COOK

0.014,1.  
 \*Specific Heat  
 475.,  
 \*\* INTERACTION PROPERTIES  
 \*Surface Interaction, name=contact  
 \*Friction  
 0.2,  
 \*Surface Behavior, pressure-overclosure=HARD  
 \*Gap Heat Generation  
 1., 0.5  
 \*\* BOUNDARY CONDITIONS  
 \*\* Name: tool Type: Symmetry/Antisymmetry/Encastre  
 \*Boundary  
 \_PickedSet27, ENCASTRE  
 \*\* Name: wp Type: Displacement/Rotation  
 \*Boundary  
 \_PickedSet13, 2, 2  
 \_PickedSet13, 6, 6  
 \*\* PREDEFINED FIELDS  
 \*\* Name: Predefined Field-1 Type: Temperature  
 \*Initial Conditions, type=TEMPERATURE  
 \_PickedSet18, 25.  
 \*\* STEP: Step-1  
 \*Step, name=Step-1, nlgeom=YES  
 \*Dynamic Temperature-displacement, Explicit  
 , 0.004  
 \*Bulk Viscosity  
 0.06, 1.2  
 \*\* Mass Scaling: Semi-Automatic  
 \*\* Whole Model



\*Fixed Mass Scaling, factor=20.

\*\* BOUNDARY CONDITIONS

\*\* Name: temp Type: Temperature

\*Boundary

\_PickedSet16, 11, 11, 25.

\*\* Name: temp1 Type: Temperature

\*Boundary

\_PickedSet26, 11, 11, 25.

\*\* Name: velo Type: Velocity/Angular velocity

\*Boundary, amplitude=Amp-1, type=VELOCITY

\_PickedSet57, 1, 1, 1.66667

\*Adaptive Mesh Controls, name=Ada-1, geometric enhancement=YES

1., 0., 0.

\*Adaptive Mesh, elset=\_PickedSet61, controls=Ada-1, frequency=5, mesh sweeps=3,

op=NEW

\*\* ADAPTIVE MESH CONSTRAINTS

\*\* Name: Ada-Cons-1 Type: Velocity/Angular velocity

\*Adaptive Mesh Constraint, constraint type=LAGRANGIAN, type=VELOCITY

\_PickedSet60

\*\* INTERACTIONS

\*\* Interaction: surface-node

\*Contact Pair, interaction=contact, mechanical constraint=KINEMATIC,

cpset=surface-node

\_PickedSurf10, \_PickedSet42\_CNS\_

\*\* Interaction: Int-2

\*Sfilm

\_PickedSurf53, F, 25., 500000.

\*\* Interaction: Int-3

\*Sfilm

\_PickedSurf54, F, 25., 0.

\*\* OUTPUT REQUESTS  
\*Restart, write, number interval=1, time marks=NO  
\*\* FIELD OUTPUT: F-Output-1  
\*Output, field, time interval=4e-05  
\*Node Output  
A, NT, RF, RFL, U, V  
\*Element Output, directions=YES  
CFailure, DMICRT, ER, EVF, HFL, LE, PE, PEEQ, PEEQVAVG, PEVAVG, S,  
STATUS, SVAVG, TEMP  
\*Contact Output  
CSTRESS,  
\*\* HISTORY OUTPUT: H-Output-1  
\*Output, history, variable=PRESELECT  
\*End Step